

OCEAN

ENGINEERING

GROUP

Prediction of Flows around Ship-shaped
Hull Sections in Roll
Using an Unsteady Navier–Stokes Solver

Yi–Hsiang Yu

August 2008

Report No. 08–1

ENVIRONMENTAL AND WATER RESOURCES ENGINEERING

DEPARTMENT OF CIVIL, ARCHITECTURAL,

AND ENVIRONMENTAL ENGINEERING

THE UNIVERSITY OF TEXAS AT AUSTIN

Austin, TX 78712

Copyright
by
Yi-Hsiang Yu
2008

**The Dissertation Committee for Yi-Hsiang Yu Certifies that this is the approved
version of the following dissertation:**

**Prediction of Flows around Ship-shaped Hull Sections in Roll Using an
Unsteady Navier-Stokes Solver**

Committee:

Spyros A. Kinnas, Supervisor

Howard M. Liljestr nd

Ben R. Hodges

Ronald L. Panton

David G. Bogard

**Prediction of Flows around Ship-shaped Hull Sections in Roll Using an
Unsteady Navier-Stokes Solver**

by

Yi-Hsiang Yu, B.S.; M.S.

Dissertation

Presented to the Faculty of the Graduate School of

The University of Texas at Austin

in Partial Fulfillment

of the Requirements

for the Degree of

Doctor of Philosophy

The University of Texas at Austin

August 2008

Acknowledgements

First, I would like to thank my supervisor, Professor Spyros A. Kinnas. He patiently guided and supported me through out the years of my study at the University of Texas at Austin. His advice, insights and thoughtfulness always inspired me to further efforts.

I would also like to thank the other committee members: Professor Howard M. Liljestrang and Professor Ben R. Hodges from Civil Engineering, Professor Ronald L. Panton and Professor David G. Bogard from Mechanical Engineering. They reviewed the draft of my dissertation and gave me invaluable comments.

I also want to express my thanks to my colleagues and my friends at the Computational Hydrodynamics Laboratory. It has been a great pleasure working together for these years. Special thanks to Vimal for working on the same problem from a different approach and having great discussions on the research. Without his help the dissertation progress would be very slow. In addition, I would also like to thank all my friends at UT Austin for their friendship and assistance.

I would like to devote my appreciation to my family. I am indebted to my dear wife, I-Huei, for her love and support, and for studying together all these days and nights at the libraries, coffee shops and home. I also want to express my gratitude to my parents, who always encouraged and supported me to study in the U.S. In addition, I also want to thank my aunt Dr. Wu, who spent a lot of time reading and editing my dissertation.

I also want to thank my favor coffee shop, café Medici, which I believe has the best coffee in Austin. In addition, I would like to recognize the support from the staff in the Civil Engineering Department at UT Austin.

Finally, I would like to thank the Offshore Technology Research Center (OTRC) for providing financial support of this research through their Cooperative Agreement with the Minerals Management Service (MMS) and its Industry Consortium.

Prediction of Flows around Ship-shaped Hull Sections in Roll Using an Unsteady Navier-Stokes Solver

Publication No. _____

Yi-Hsiang Yu, Ph.D.

The University of Texas at Austin, 2008

Supervisor: Spyros A. Kinnas

Ship-shaped hulls have often been found to be subject to excessive roll motions, which can inhibit their use as a stable production platform. To solve the problem, bilge keels have been widely adopted as an effective and economic way to mitigate roll motions, and their effectiveness lies in their ability to damp out roll motions over a range of frequencies. In light of this, the present research focuses on roll motions of ship-shaped hulls. A finite volume method based two-dimensional Navier-Stokes solver is developed and further extended into three dimensions. The present numerical scheme is implemented for modeling the flow around ship-shaped hulls in prescribed roll motion and for predicting the corresponding hydrodynamic loads. Studies on the hydrodynamic performance of ship-shaped hull in transient roll decay motions are also conducted. Systematic studies of grid resolution, the effects of free surface, hull geometries and amplitude of roll angle on the results are performed. Predictions from the present method compare well to those of other methods, as well as to measurements from experiments. Non-linear effects, due to the effect of viscosity, were observed in small as well as in

large roll amplitudes, particularly in the cases of hulls with sharp corners. The results of the present method also suggest that it is inadequate to use a linear combination of added-mass and damping coefficients to represent the corresponding hydrodynamic loads. As a result, the calculation of the hull response is performed in the time domain. Finally, the capability of the present numerical scheme to apply in fully three-dimensional ship motion simulations is demonstrated.

Table of Contents

List of Tables	xi
List of Figures	xii
Chapter 1: Introduction.....	1
1.1 Background	1
1.2 Motivation	3
1.3 Objectives.....	5
1.4 Overview	6
Chapter 2: Literature Review.....	8
2.1 Prediction of Ship Motions	8
2.1.1 Experimental Studies.....	8
2.1.2 Numerical Studies	10
2.2 Numerical Methods.....	14
Chapter 3: Methodology	17
3.1 Governing Equations	17
3.2 Numerical formulations	18
3.2.1 Finite Volume Method	18
3.2.2 Moving and Deforming Mesh.....	20
3.2.3 Approximation of Fluxes and Cell Face Values	23
3.2.4 Pressure-Correction Method	27
3.3 Boundary Conditions	30
3.3.1 Velocity Inlet and Wall Boundaries	30
3.3.2 Free Surface boundary.....	32
Chapter 4: Verification and Validation of NS2D.....	36
4.1 Vertical Plate Subject to Alternating Inflow	36
4.1.1 Background	37
4.1.2 Force and Error Calculations	38

4.1.3 Results	39
4.2 Submerged Hull Subject to Oscillating Inflow	45
4.2.1 Background	45
4.2.2 Results	46
4.3 Prescribed Roll Motion of a Submerged Hull	48
4.3.1 Background	48
4.3.2 Mesh Movement.....	50
4.3.3 Results	52
4.4 Piston Type Wave-maker	57
4.5 Summary	59
Chapter 5: Two-Dimensional Ship-Shaped Hull	60
5.1 Prescribed Roll Motion	60
5.1.1 Background	60
5.1.2 Hull Geometries	67
5.1.3 Sensitivity Analyses	68
5.1.4 Correlation with Other Methods	73
5.1.5 The Effect of The Free Surface.....	98
5.1.6 The Effect of Roll Angle Amplitude.....	101
5.1.7 The Effect of Hull Geometry	103
5.2 Decay Motions.....	113
5.2.1 Background	113
5.2.2 Results	116
5.3 Summary	124
Chapter 6: Three-Dimensional Results	125
6.1 Piston Type Wave-maker	125
6.2 Prescribed Roll of A Ship-shaped Hull with A Uniform Hull Cross-section	129
6.3 Prescribed Roll of A Ship-shaped Hull with A Non-uniform Hull Cross-section	133
6.4 Summary	139

Chapter 7: Conclusions and Recommendations	140
7.1 Conclusions	140
7.2 Recommendations.....	143
Appendix A: Approximation of Fluxes and Cell Face Values	146
A.1 Calculations for Cell Face Value	146
A.2 Calculations for Normal Derivative Values	147
A.3 Calculations for Convective Flux	148
Appendix B: Non-Dimensionalization	150
Glossary	152
References.....	158
Vita	164

List of Tables

Table 5.1: The non-dimensional parameters for various roll frequencies used in NS2D.....	63
Table 5.2: Differences between NS2D and FLUENT.....	66

List of Figures

Figure 1.1: A typical FPSO connected to other drilling platforms (source: upload.wikimedia.org/wikipedia/commons/8/80/FPSO_diagram.PNG).	2
Figure 1.2: Kizomba B FPSO (source: http://www.toolpusher.co.uk/jh1%20033.jpg).	2
Figure 1.3: Mid-ship hull section showing bilge keels (source: http://k43.pbase.com/v3/45/387545/1/50702675.DSC_3086z.jpg)...	4
Figure 3.1: A cell in three-dimensions with its neighboring points and faces.	19
Figure 3.2: A typical 2D mesh at two time steps and the volume swept by an arbitrary cell face.....	22
Figure 3.3: Arbitrary east face of a 3-D cell with the computational points.	23
Figure 3.4: Arbitrary east face of a 2D cell with the computational points and their auxiliary points.	25
Figure 3.5: Kinematic Boundary Condition on the Free Surface.	33
Figure 3.6: 2D cells under the free surface, and the free-surface position.	35
Figure 4.1: Grid and domain orientation for the vertical plate problem.	37
Figure 4.2: Convergence studies in space with different grid resolutions in the vertical direction. (a) Non-dimensional force histories, (b) logarithmic plot of ϵ_F for different numbers of cells.	41
Figure 4.3: Convergence studies on non-dimensional forces over one period with different number of cells in the horizontal direction of the domain.	42
Figure 4.4: Convergence studies on non-dimensional forces over one period with different time step sizes.....	42

Figure 4.5: Streamline and vorticity contour plots predicted by NS2D solver with $KC=1$ at (a) start of the period, (b) quarter of the period, (c) half of the period, (d) 3/4 of the period..... 43

Figure 4.6: Comparison between the drag coefficients obtained from the NS2D solver and from measurements by Sarpkaya and O’Keefe (1996) in the case of oscillating flow past a flat plate problem. 44

Figure 4.7: Comparison between the inertia coefficients obtained from the NS2D solver and from measurements by Sarpkaya and O’Keefe (1996) in the case of oscillating flow past a flat plate problem..... 44

Figure 4.8: Fluid domain and corresponding domain boundaries of a *submerged* hull subject to alternating flow. 45

Figure 4.9: Pressure distributions along the fixed submerged hull subject to alternating inflow from NS2D and FLUENT at $t/T_{in}=1.75$ ($Re = 10^5$). 47

Figure 4.10: Pressure distributions along the fixed submerged hull subject to alternating inflow from FLUENT at different Reynolds numbers (Laminar or Turbulent flow) at $t/T_{in} = 2.75$ 47

Figure 4.11: Computational domain and corresponding domain boundaries of the submerged hull under prescribed roll motion..... 48

Figure 4.12: Mesh movement of NS2D in the case of a submerged hull..... 51

Figure 4.13: Mesh movement of FLUENT in the case of a submerged hull..... 51

Figure 4.14: y-plus along the round bilge hull in FLUENT(T) simulations ($\alpha_0=5.75^\circ$). 53

Figure 4.15: Moment histories of submerged round bilge hulls for $Fn=0.4$ and $\alpha_0=5.75^\circ$ from NS2D, FLUENT(L), and FLUENT(T). 54

Figure 4.16: Vorticity magnitude contour of the submerged round bilge hull for $F_n=0.4$ and $\alpha_0=5.75^\circ$ from (top) NS2D, (mid) FLUENT(L), and (bottom) FLUENT(T) at $t/T=4.00$ and $t/T=4.40$	55
Figure 4.17: Pressure distributions on the submerged round bilge hull from NS2D, FLUENT(L) and FLUENT(T) at $t/T=4.00$ and $t/T=4.40$ ($F_n=0.4$ and $\alpha_0=5.75^\circ$).....	56
Figure. 4.18: Computational domain and corresponding domain boundaries of a 2D piston type wave-maker problem.....	57
Figure 4.19: The wave elevation of a piston type wave maker at $t / \sqrt{h/g} = 19.10$	58
Figure 5.1: Computational domain and corresponding domain boundaries of the FPSO hull forced roll motion problem.....	61
Figure 5.2: Mesh movement of NS2D in the case of a ship-shaped hull.....	64
Figure 5.3: Mesh movement of FLUENT in the case of a ship-shaped hull.....	65
Figure 5.4: Four shapes of the hull: (1) Round bilge model; (2) Bilge keel model; (3) Box model; (4) Step model.....	67
Figure 5.5: The definition of the boundary-layer cell height.....	70
Figure 5.6: Logarithmic plot of the absolute errors between the "exact" solution and the results from coarser grid resolutions (round bilge hull, $\alpha_0=5.75^\circ$ and $F_n=0.4, 0.8$ and 1.2).	70
Figure 5.7: Comparison of the moment histories for different boundary layer cell heights and its blowup view (round bilge hull, $\alpha_0=5.75^\circ$ and $F_n=0.8$).71	71
Figure 5.8: Comparison of the moment histories for different time step sizes and its blowup view (round bilge hull, $\alpha_0=5.75^\circ$ and $F_n=0.8$).	72

Figure 5.9: Comparison of pressure and velocity components between NS2D(IN) and NL-BEM (Vinayan et al. 2005) (round bilge hull, $\alpha_0=5.75^\circ$, $Fn=1.0$ and $t/T=2.75$).....	74
Figure 5.10: Comparison of pressure and velocity components between NS2D(IN) and NL-BEM (Vinayan et al. 2005) (round bilge hull, $\alpha_0=5.75^\circ$, $Fn=1.0$ and $t/T=3.00$).	75
Figure 5.11: Comparison of pressure and velocity components between NS2D(IN) and NL-BEM (Vinayan et al. 2005) (round bilge hull, $\alpha_0=11.5^\circ$, $Fn=1.0$ and $t/T=2.75$).	76
Figure 5.12: Comparison of pressure and velocity components between NS2D(IN) and NL-BEM (Vinayan et al. 2005) (round bilge hull, $\alpha_0=11.5^\circ$, $Fn=1.0$ and $t/T=3.00$).	77
Figure 5.13: Comparison of the moment histories between NS2D and NL-BEM (Vinayan et al. 2005) results (round bilge hull, $\alpha_0=5.75^\circ$, $Fn=1.0$ and $t/T=2.45$).....	78
Figure 5.14: Comparison between the moment histories from NS2D(IN) and NS2D(VS). (round bilge hull, $\alpha_0=5.75^\circ$, $Fn=0.6$).....	79
Figure 5.15: Comparison of the pressure distribution along the FPSO hull between results from NS2D(IN) and NS2D(VS) (round bilge hull, $\alpha_0=5.75^\circ$, $Fn=1.0$ and $t/T=3.00$).	80
Figure 5.16: Mesh used in NS2D ($N \approx 10,000$) and the blowup view at the bilge area.	82
Figure 5.17: Mesh used in FLUENT ($N \approx 62,000$, air/water $\approx 22,000/40,000$) and the blowup view at the bilge area.	83

Figure 5.18: Comparison between the wave elevations from NS2D and the volume fraction of water (background contour) from FLUENT(L) at three levels, 0.45, 0.50 and 0.55 (round bilge hull, $\alpha_0=5.75^\circ$, $F_n=0.8$ and $t/T=5.00$).	84
Figure 5.19: Comparison of the moment histories from NS2D, FLUENT(L), FLUENT(T) (round bilge hull, $\alpha_0=5.75^\circ$, $F_n=0.8$ and $t/T=5.00$). ...	84
Figure 5.20: Vorticity magnitude contour From NS2D (round bilge hull, $\alpha_0=5.75^\circ$, $F_n=0.8$ and $t/T=3.00$).	85
Figure 5.21: Vorticity magnitude contour From FLUENT(L) (round bilge hull, $\alpha_0=5.75^\circ$, $F_n=0.8$ and $t/T=3.00$).....	85
Figure 5.22: Vorticity magnitude contour From FLUENT(T) (round bilge hull, $\alpha_0=5.75^\circ$, $F_n=0.8$ and $t/T=3.00$).....	86
Figure 5.23: Moment histories from NS2D and other methods (round bilge hull, $\alpha_0=5.75^\circ$, $F_n=0.8$ and $-\omega^2\sin(\omega t)$ represents the angular acceleration).	88
Figure 5.24: Moment histories from NS2D and other methods (round bilge hull, $\alpha_0=5.75^\circ$, $F_n=1.0$ and $-\omega^2\sin(\omega t)$ represents the angular acceleration).	88
Figure 5.25: Added-mass coefficients from NS2D, FLUENT, and other methods (round bilge hull and $\alpha_0=5.75^\circ$).	89
Figure 5.26: Damping coefficients from NS2D, FLUENT, and other methods (round bilge hull and $\alpha_0=5.75^\circ$).....	89

Figure 5.27: Comparison between the wave elevations from NS2D and the volume fraction of water (background contour) from FLUENT(L) at three levels, 0.45, 0.50 and 0.55 (4% bilge keel hull, $\alpha_0=2.87^\circ$, $Fn=0.8$ and $t/T=6.00$).	90
Figure 5.28: Vorticity magnitude contour From NS2D (4% bilge keel hull, $\alpha_0=2.87^\circ$, $Fn=0.8$ and $t/T=3.00$).	92
Figure 5.29: Vorticity magnitude contour from FLUENT(L) (4% bilge keel hull, $\alpha_0=2.87^\circ$, $Fn=0.8$ and $t/T=3.00$).	92
Figure 5.30: Vorticity magnitude contour from FLUENT(T) (4% bilge keel hull, $\alpha_0=2.87^\circ$, $Fn=0.8$ and $t/T=3.00$).	93
Figure 5.31: Moment histories for $Fn=0.6$ from NS2D, FLUENT(L), and FLUENT(T) (4% bilge keel hull, $Fn=0.8$ and $\alpha_0=2.87^\circ$).	93
Figure 5.32: Moment histories for $Fn=0.8$ from NS2D, FLUENT(L) and FLUENT(T) (4% bilge keel hull and $\alpha_0=2.87^\circ$).	94
Figure 5.33: Histories of total moment from NS2D and other methods ($Fn=0.8$ and $\alpha_0=2.87^\circ$).	95
Figure 5.34: Added-mass coefficients from NS2D, FLUENT, and other methods (4% bilge keel hull and $\alpha_0=2.87^\circ$).	96
Figure 5.35: Damping coefficients from NS2D, FLUENT, and other methods (4% bilge keel hull and $\alpha_0=2.87^\circ$).	96
Figure 5.36: Damping coefficients for the box model with $\alpha_0=5.0^\circ$	97
Figure 5.37: Damping coefficients for the step model $\alpha_0=5.0^\circ$	98
Figure 5.38: Free-surface elevations in the case of $Fn=0.4$ and $Fn=1.2$ ($\alpha_0=5.75^\circ$).	99
Figure 5.39: Comparison between the moment histories for a ship-shaped hull and a submerged hull (round bilge hull, $Fn=0.4$ and $\alpha_0=5.75^\circ$).	100

Figure 5.40: Comparison between the moment histories for a ship-shaped hull and a submerged hull (round bilge hull, $Fn=1.2$ and $\alpha_0=5.75^\circ$).....	100
Figure 5.41 Total moment histories of round bilge model for different roll angles (scaled by $\alpha_0=5^\circ$).....	101
Figure 5.42: Roll added-mass coefficients for the round bilge model ($\alpha_0=5^\circ, 10^\circ, 15^\circ, 20^\circ$).....	102
Figure 5.43: Roll damping coefficients for the round bilge model ($\alpha_0=5^\circ, 10^\circ, 15^\circ, 20^\circ$).....	102
Figure 5.44: Total moment histories for different hull geometries ($Fn=1.0$ and $\alpha_0=5.75^\circ$).....	104
Figure 5.45: Roll added-mass coefficients for different hull geometries.....	105
Figure 5.46: Roll damping coefficients for different hull geometries.....	105
Figure 5.47: Vorticity contours ($t/T=5.75, Fn=1.0$ and $\alpha_0=5.75^\circ$), (a) round bilge model, (b) box model, (c) step model, (d) 4% bilge keel model. ...	107
Figure 5.48: Pressure distributions on the hull (round bilge model, $Fn=0.8$ and $\alpha_0=5.75^\circ$).....	108
Figure 5.49: Pressure distributions on the hull (box model, $Fn=0.8$ and $\alpha_0=5.75^\circ$).....	108
Figure 5.50: Pressure distributions on the hull (step model, $Fn=0.8$ and $\alpha_0=5.75^\circ$).....	109
Figure 5.51: Pressure distributions on the hull (4% bilge keel model, $Fn=0.8$ and $\alpha_0=5.75^\circ$).....	109
Figure 5.52: Roll added-mass coefficients for different bilge keel lengths ($\alpha_0=2.87^\circ$).....	110
Figure 5.53: Roll damping coefficients for different bilge keel lengths ($\alpha_0=2.87^\circ$).....	110
Figure 5.54: The geometries for different types of bilge keels.....	112

Figure 5.55: Roll added-mass and damping coefficients for horizontal and vertical bilge keels ($\alpha_0=2.87^\circ$).....	112
Figure 5.56: Center of gravity in roll decay.....	114
Figure 5.57: The heave or decay motion of a hull and its mean position.....	115
Figure 5.58: Heave motions responses from NS2D and other methods (round bilge hull and $y_0=0.125B$).....	118
Figure 5.59: Logarithmic decay of the heave motions from NS2D and other methods (round bilge hull and $y_0=0.125B$).....	118
Figure 5.60: Roll response for different hull geometries ($\alpha_0=14.32^\circ$).	119
Figure 5.61: Roll response for different initial roll displacements (round bilge hull).	119
Figure 5.62: Vorticity contours and the corresponding hull positions for round bilge model at $t^* = t / \sqrt{B/g} = 0$ and $t^* = t / \sqrt{B/g} = 12$ ($\alpha_0=14.32^\circ$).120	
Figure 5.63: Vorticity contours and the corresponding hull positions for box model at $t^* = t / \sqrt{B/g} = 0$ and $t^* = t / \sqrt{B/g} = 13$ ($\alpha_0=14.32^\circ$).....	121
Figure 5.64: Vorticity contours and the corresponding hull positions for step model at $t^* = t / \sqrt{B/g} = 0$ and $t^* = t / \sqrt{B/g} = 14$ ($\alpha_0=14.32^\circ$).	122
Figure 5.65: Vorticity contours and the corresponding hull positions for 4% bilge keel model at $t^* = t / \sqrt{B/g} = 0$ and $t^* = t / \sqrt{B/g} = 15$ ($\alpha_0=14.32^\circ$).123	
Figure 6.1: Computational domain and corresponding domain boundaries of a 3D piston type wave-maker problem.....	126
Figure 6.2: Three slices of the pressure contours for x - y plane at $t / \sqrt{h_d/g} = 20$.127	
Figure 6.3: 3D free-surface elevation at (a) $t / \sqrt{h_d/g} = 5.0$, (b) $t / \sqrt{h_d/g} = 10.0$, (c) $t / \sqrt{h_d/g} = 15.0$ and (d) $t / \sqrt{h_d/g} = 20.0$	127

Figure 6.4: Free-surface elevation from NS3D, NS2D and Lin (1984) at $t / \sqrt{h_d / g} = 19.1$	128
Figure 6.5: Computational domain and corresponding domain boundaries of a 3D prescribed roll motion problem in a uniform channel with a uniform hull cross-section.	130
Figure 6.6: Mesh of the 3D prescribed roll motion problem in a uniform channel with a uniform hull cross-section.	130
Figure 6.7: The vorticity contour and the vorticity iso-surface of the 3D prescribed roll motion problem in a uniform channel with a uniform hull cross- section.....	131
Figure 6.8: Slices of pressure contours for x - y plane in the case of the 3D prescribed roll motion problem in a uniform channel with a uniform hull cross- section.....	131
Figure 6.9: Comparison between the pressure distribution from NS2D and NS3D.	132
Figure 6.10: Computational domain and corresponding domain boundaries of a 3D prescribed roll motion problem in a uniform channel with a non-uniform hull cross-section, and a blowup view of the hull.....	135
Figure 6.11: The vorticity contour and the vorticity iso-surface of the 3D prescribed roll motion problem in a uniform channel with a non-uniform hull cross- section.....	136
Figure 6.12: Slices of pressure contours for x - y plane in the case of the 3D prescribed roll motion problem in a uniform channel with a non-uniform hull cross- section.....	136
Figure 6.13: Pressure contours for the 3D prescribed roll motion problem in a uniform channel with a non-uniform hull cross-section ($Fn=0.8$).	137

Figure 6.14: Pressure contours for the 3D prescribed roll motion problem in a uniform channel with a non-uniform hull cross-section ($F_n=1.2$).137

Figure 6.15: Moment histories for non-uniform cross-section cylindrical hull (round bilge model, $F_n=0.8$ and $\alpha_0=5.75^\circ$).138

Figure 6.16: Moment histories for non-uniform cross-section cylindrical hull (round bilge model, $F_n=1.2$ and $\alpha_0=5.75^\circ$).138

Chapter 1: Introduction

1.1 BACKGROUND

Oil has been drilled from offshore locations since the 1950s when all oil platforms originally sat on the seabed. The rising demand of oil has pushed the exploration of oil to move to deeper waters and longer distances offshore. However, due to the water depth and the prevailing harsh weather conditions, it is an expensive and challenging task to setup the drilling and production system in deep seas.

Since the usage of a fixed platform is limited in shallow water, the offshore oil and gas industry has been using floating production systems since the mid-1970s. Floating, Production, Storage and Offloading (FPSO) drilling vessels, often converted from tankers, are a typical type of floating production system, used for the extraction of oil in deep seas. FPSOs can be taken offsite when in the projected path of a hurricane. From the environmental as well as the economic standpoints, FPSOs are also very cost effective due to the fact that they can be re-used elsewhere when the oil field's productive life ends. This is a fact especially attractive for marginal oil fields, where the production facilities are mostly needed for only a few years. Figure 1.1 presents a floating oil drilling system, which involves an FPSO and other drilling platforms, and Fig. 1.2 shows an operating FPSO hull situated off the coast of northern Angola (Kizomba B FPSO has a storage capacity of 2.2 million barrels, and is 285m long, 63m wide, and 32m high).

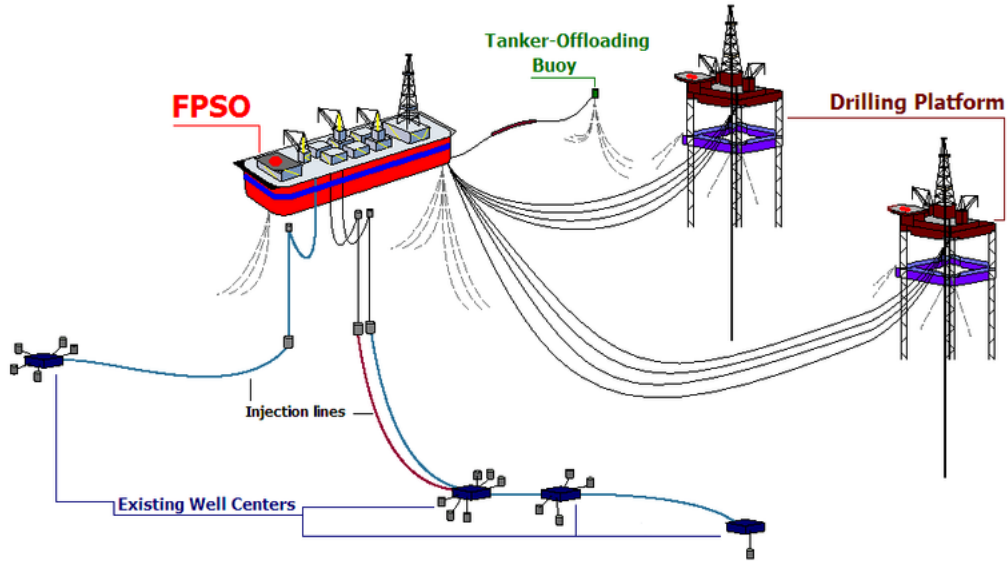


Figure 1.1: A typical FPSO connected to other drilling platforms (source: upload.wikimedia.org/wikipedia/commons/8/80/FPSO_diagram.PNG).



Figure 1.2: Kizomba B FPSO (source: <http://www.toolpusher.co.uk/jh1%20033.jpg>).

1.2 MOTIVATION

FPSO hulls have often been found to be subject to excessive roll motions that inhibit their use as a stable production platform. Most commonly considered systems and methods of roll reduction can be divided into the following two groups:

- Active stability system: Active stabilizer fins.
- Passive systems, such as anti-roll tanks and bilge keels.

According to Kasten (2002), active stabilizer fins can provide up to a 90% roll reduction, depending on the ship speed. They are most effective at maximum ship speed, and marginally effective with zero ship speed. As a result, the active stabilizer fins are not considered as an option for stationary vessel such as FPSOs. They are also relatively expensive and complex to install. For passive roll reduction systems, ship speed is not a limiting factor. Using passive anti-roll tanks, the roll reduction can be on the order of 50% to 60%. The main disadvantage, however, is the added displacement required to carry the extra deadweight of the tank contents. Passive anti-roll tanks are also relatively complex to design correctly. Using bilge keels, another passive roll-reduction approach, can provide roll attenuations on the order of 35% to 55%. Compared to anti-roll tanks, bilge keels may cause some added frictional resistance due to increased wetted surface area. However, they are relatively inexpensive and simple to install. As shown in Fig.1.3¹, a bilge keel is a long fin of metal, often in a "V" shape, and attached along the length of the vessel, which runs over the mid-ship portion of the hull to the turn of the bilge. Bilge keels increase the hydrodynamic resistance when a hull rolls, and thus reduce the tendency of a hull to roll when it is subject to waves. Bilge keels have been widely

¹ Note that Fig. 1.3 shows a mid-ship hull section of a ferry, which is much smaller than an FPSO hull. The mid-ship portion of an FPSO hull and the corresponding bilge keel length in the hull longitudinal direction will be longer than what is shown in Fig. 1.3.

used as an effective and economic way to mitigate roll motions, and their effectiveness lies in their capability to damp out roll motions over a range of frequencies. It is essential to simulate the separated flow around the bilge keels under a large angle of roll motions and to predict the corresponding hydrodynamic loads correctly.



Figure 1.3: Mid-ship hull section showing bilge keels (source: http://k43.pbase.com/v3/45/387545/1/50702675.DSC_3086z.jpg)

Empirical and semi-empirical formulae, based on experimental data, have been used in the past for estimating the roll damping moment. The decay and prescribed roll tests are two types of experiments which are often performed on hull models. Therefore, most existing studies focus on these areas. In the past, the three-dimensional problems of a hull subject to roll motions are often approximated by two-dimensional approaches using strip theory. These approaches are basically two-dimensional solutions at each cross-

section integrated along the ship's length. Strip theory has been used widely because it reduces computational effort. Strip-theory predictions, however, are poor at high wave frequencies (or high Froude numbers, equivalently), and/or for hulls with large beam to length ratio. A fully three-dimensional solver is, therefore, needed to accurately predict the wave-hull interaction.

The numerical modeling until now has been limited because of insufficient computational resources. Most of the past numerical schemes were based on potential (inviscid) methods. More recently, the use of viscous solvers, e.g. Reynolds Averaged Navier-Stokes (RANS) solver, for the prediction of hull motions has become more common, despite the fact that these methods often require very large number of nodes (or cells), especially in the case of three dimensions. With rapidly increasing computer capacity², full-scale application of numerical tools on hull motion problems is now more feasible.

1.3 OBJECTIVES

The objective of the research is to develop a robust and reliable computational tool to predict hull motions and the resulting hydrodynamic loads, with emphasis on roll. More precisely, the research aims to perform systematic studies on grid dependence of the results of the developed methods, and to investigate the effects of hull geometries and the presence of the bilge keels on the reduction of hull motions.

A two-dimensional numerical scheme for solving the unsteady Euler equations in the context of propulsor flows was developed by the Ocean Engineering Group in the University of Texas at Austin (Choi 2000; Choi and Kinnas 2001; 2003). Later, the

² The rapidly increasing computer capacity is primarily achieved by higher CPU speed and by using parallel computation, which allows larger number of cells and reduces running time.

numerical scheme has been modified to include the effect of viscosity and was named NS2D. It was applied to simulate hull motions and to predict corresponding hydrodynamic loads in Kakar (2002) and Kacham (2004) with simplified hull geometries and assumptions. In this study, the two-dimensional numerical scheme is further improved, and applied to problems with more complex hull geometries. Some preliminary studies were presented in Kinnas et al. (2003) ;Yu et al. (2005); Kinnas et al. (2006; 2007); and Yu and Kinnas (2008). The solver is later extended into three dimensions, which will be mentioned as NS3D hereafter.

1.4 OVERVIEW

This dissertation is organized into seven chapters:

Chapter 1 includes the background, motivation, and the objectives of the research.

Chapter 2 presents the literature review of related studies on the prediction of hull motions and a review of the numerical methods related to the present numerical scheme.

Chapter 3 describes the methodology used in the study, which includes the governing equations, the numerical formulations, the boundary conditions, and the hull geometries.

Chapter 4 presents two types of simplified two-dimensional simulations for the verification and validation purposes of the present numerical scheme. In the first type of simulation, the study is performed in the case of a submerged body, and the other type of simulation is conducted on a wave-maker problem.

Chapter 5 presents the simulations of two-dimensional ship-shaped hulls subject to prescribed roll motion (section 5.1) or in free-decay motions (section 5.2). Section 5.1 presents the grid sensitivity analyses in space and in time, and the comparisons of the

results from NS2D and those from other methods. Also presented are the studies of the effects of free surface, hull geometries, and roll angle amplitudes. Section 5.2 addresses the effects of hull geometries and initial roll displacements on mitigating roll motions.

Chapter 6 shows the simulations of three test cases for the verification and validation purposes of the three-dimensional Navier-stokes solver (NS3D): a piston type wave-maker problem and the prescribed roll motion problems for a uniform or a non-uniform cross-section hull.

Chapter 7 summarizes the conclusions and the contributions of the study, and provides recommendations for future research.

Chapter 2: Literature Review

This chapter reviews the existing literature related to ship-shaped hull roll motion problems. The first section focuses on the prediction of hull motions, particularly in roll. The second section discusses numerical methods related to the present numerical scheme.

2.1 PREDICTION OF SHIP MOTIONS

An accurate assessment of wave-body interaction is of crucial importance to ocean engineering and ship design industry. The corresponding experimental and numerical methods have been developed and investigated over past years. The first subsection will review the existing experimental studies, and the second subsection will review the existing numerical methods.

2.1.1 Experimental Studies

For two-dimensional wave-body interactions, Vugts (1968) made a great contribution in investigating independent roll, heave and sway motions for various hull geometries. He was the first to calculate the hydrodynamic coefficients for sharply edged sections in roll motions and to observe the importance of the viscous effect. The results have been used as a guideline for ship design.

Sarpkaya and Okeefe (1996) presented the experimental measurements of two- and three-dimensional vertical plates subject to an oscillating inflow. The vertical plate was a simplified geometry, which can be viewed as a slender bilge keel placed on a flat wall without the presence of the free surface. They concluded that bilge keels did provide a high degree of damping, which was affected by the vortex shedding from the edge of

the plate. Therefore, the use of the damping coefficients obtained from free-plate tests is not necessarily applicable to wall-bounded cases.

Yeung et al. (1998) conducted an experimental study on the prescribed roll motion for a rectangular ship-like section, and compared the hydrodynamic coefficients obtained from their experiments to those from FSRVM, where the acronym FSRVM stands for the Free-Surface Random Vortex Method, developed by Yeung et al. (1993). Note that the round bilge hull geometry that they used has a different bilge radius (2% of the beam), as compared to the one (3.125% of the beam) used in Vugts (1968). This difference results in a deviation on the prediction of the corresponding hydrodynamic coefficients. The results of Yeung et al. (1998) also showed that the added-mass coefficient is not affected for roll amplitudes less than 5.75 degrees.

Following their research in 1998, Yeung et al. (2000) performed a study in which each side of the hull was attached with a bilge keel and the assumption of uniform cross hull section was made. They compared the results from the experimental measurements to those from FSRVM and BFFDM, where the acronym BFFDM stands for the Boundary-Fitted Finite-Difference Method based numerical solver (Alessandrini and Delhommeau 1994). A study on the effect of the bilge keel length was performed. The results showed that an increase in the keel size enlarges both the added-mass and damping coefficients.

Na et al. (2002) presented some experimental data for an FPSO hull with vertical and horizontal bilge keels subject to roll motions. Another study presented by Seah and Yeung (2003) investigated the same problem by using FSRVM. Both of their studies concluded that the horizontal bilge keels generate vortices closer to the free surface, and thus carry more energy away from the body, and result in a higher damping coefficient.

Yuck et al. (2003) performed a series experimental studies and partial numerical calculations for analyzing the roll motion of non-conventional mid-ship sections. The damping coefficients for various hull models, a round bilge model, a box (square) model and a step model, were estimated. The researchers divided the roll damping into the wave-making component and the viscous component. The viscous component was predicted by simulating a submerged hull problem, where the free surface was absent. The wave component was determined experimentally by a far-field momentum method. Their results were compared to the numerical results obtained from the potential theory and the experimental results from Vugts (1968), which have shown great agreement. Unfortunately, the authors did not provide any experimental data on the roll added-mass calculation.

Irvine et al. (2006) presented a series of studies on the free roll decay motion of an advancing surface combatant in calm water. The results of three model tests from three different international facilities were compared, and their comparisons show significant differences in roll decay and period among the facilities. Their study also shows a difficulty in simulating the ship roll motion problems. Irvine et al. (2008) also presented another study on the towing-tank experiments of coupled pitch and heave motions for a surface combatant in regular head waves. An equation was derived to predict the Froude number for maximum response as a function of ship geometrical coefficients.

2.1.2 Numerical Studies

Traditionally, naval architecture sub-disciplines are separated for resistance and propulsion, maneuvering, and seakeeping. Of the three sub-discipline areas, the

application of viscous methods to resistance and propulsion problems has been studied for more than two decades. At the recent Gothenburg 2000 Workshop on CFD in Ship Hydrodynamics³, the results have shown that the existing methods are able to predict ship resistance with reasonable accuracy. Tahara et al. (2000) applied the RANS method to optimize hull forms for a variety of objective functions for ships with steady forward speed in calm sea.

On the contrary, the application of viscous methods for maneuvering and seakeeping is more complicated due to the interactions among unsteady flows, ship motions and complex environments (e.g., incident waves and wave breaking), and such simulation also requires large computational power. For steady ship maneuvering, Tahara et al. (1992) applied an interactive approach for calculating ship boundary layers and wakes for nonzero Froude number. In Tahara and Stern's (1996) study, a large-domain approach was developed for the same problem. In their approach, the RANS and continuity equations were solved with the Baldwin-Lomax turbulence model with exact nonlinear kinematic and approximate dynamic free-surface boundary conditions, and a body/free-surface conforming grid. More studies with the application of viscous methods can be found in Alessandrini and Delhommeau (1998); Tahara et al. (1998); Di Mascio and Campana (1999); Hochbaum and Vogt (2002); Simonsen and Stern (2003) and Simonsen and Stern (2005). In Simonsen and Stern's (2005) study, a simplified potential theory-based infinite-bladed propeller model was coupled with the RANs solver to give a model that interactively determines propeller-hull-rudder interaction without requiring detailed modeling of the propeller geometry. For unsteady ship maneuvering, however,

³ A workshop on Numerical Ship Hydrodynamics, Chalmers University of Technology, Gothenburg, Sweden; September 2000.

most studies are conducted based on motion simulation programs with empirically derived coefficients.

For seakeeping, early studies were based on the assumptions of small amplitude motions and potential theory. Later, Sen (2002) presented the time domain computation of large amplitude ship motion using a potential flow based solver. In the study, both linear and non-linear (large amplitude) computations were included, and the nonlinearities had a considerable influence on the results. The potential flow solvers, however, have been proven adequate for sway, pitch and heave motions, in which the viscous effect is insignificant. In the case of roll, however, these solvers fail due to the assumption of irrotational flow and the absence of viscous effects. Himeno (1981); Taz UI Mulk and Falzarano (1994) included the viscous effects in the potential flow based models by incorporating empirically derived roll damping data. However, the simulations are limited to the ship geometry, the frequency of ship motion, and operating parameters from the empirical data. Therefore, the development of viscous methods and the prediction of large amplitude of motions are critical needed for ship design.

For the application of viscous methods to seakeeping problems, most studies focuses on 2D oscillating bodies, and the effects of viscosity are clearly observed (Korpus and Falzarano 1997; Sarkar and Vassalos 2001; Seah and Yeung 2003; Yeung et al. 1998; Yeung et al. 2000). In Korpus and Falzarano's (1997) study, a fully submerged hull without bilge keels was investigated using a RANS method. They performed a series of parametric studies in order to identify the individual contributions of viscosity, vorticity, and pressure. They have found that both the magnitude and phase of roll moment were strongly affected by rotational flow contributions to pressure (i.e., shed vortices near the bilge). They also concluded that in the case where the bilge keels are present, one must account for the nonlinear effects at the third and fifth harmonic of the

forcing frequency, which implies that it is not sufficient to use only the added-mass and damping coefficients to represent the moment and forces on the hull. Sarkar and Vassalos (2001) used a Reynolds Averaged Navier-Stokes (RANS) solver, "COMET", to simulate the flow in the case of a rectangular cylinder rolling at the free surface, where the Volume Of Fluid (VOF) method was applied to predict the free surface. In their study, a series of investigations on the square and round bilge hulls for varying roll frequency have been performed with different roll angle amplitudes. However, the bilge radius that they used for a round bilge hull was 0.625% of the beam, rather than 2% (Yeung et al. 1998) or 3% (Vugts 1968) of the beam. According to Sarkar and Vassalos (2001), the results are sensitive to the hull geometries as well as to the bilge radius. Their results show that the characteristics of the physical flow can be simulated qualitatively, but the resulting hydrodynamic coefficients are inconsistent with those from Vugts (1968) and Yeung et al. (1998).

For 3D investigations, Miller et al. (2002) performed a study on the prediction of forces and moment on a 3D submerged cylinder fitted with bilge keels subject to prescribed roll motions. Moreover, Prediction of pitch and heave motions for ships with regular head waves was conducted for a container ship in Hochbaum and Vogt (2002), where the level-set algorithm was applied to predict the free surface. For Wigley hull and Series 60 cargo ships, prediction of pitch and heave motions for ships was performed in Sato et al. (2000) using density function free surface modeling. In addition, Wilson et al. (1998) performed simulations for Wigley hull, Series 60 cargo ships and DTMB model 5512 for medium speed/long wave and high speed/short wave conditions, and validated their RANS solver. Following the same research, Weymouth et al. (2005) presented a study on pitch and heave motions for the Wigley hull in incident waves, and the RANS results were compared to those from strip theory. Later, Wilson et al. (2006) extended

their previous work to unsteady RANS simulations of general 6DOF ship motions and maneuvering, and analyzed the prescribed roll motion for a ship-shaped hull. A spring–mass-damper system was used to compare their non-linear predictions to the traditional linear strip theory results. The natural rolling frequency and the roll decay rate at multiple ship speeds both with and without bilge keels were predicted. Their study highlighted the viability and the importance of the numerical simulation for fully three-dimensional ship motion problems.

2.2 NUMERICAL METHODS

The early investigations of three-dimensional wave-body interaction were based on the two-dimensional theory. A number of two-dimensional strip-theory based methods for the slender body have been subsequently developed by various researchers. The pioneering work was proposed by Korvin-Kroukovsky (1955).

Based on the potential theory, the Laplace equation has been widely used for modeling wave propagation. For the prediction of large amplitude wave motion, various approaches have been pursued and categorized as fully non-linear methods. The fully non-linear free surface calculation following the Mixed Euler-Lagrangian approach was proposed by Longuet-Higgins and Cokelet (1976) in a two-dimensional flow. It is based on the Boundary Element Method (BEM), and the approach has been widely used by many researchers. Vinayan et al. (2005) also implemented the Mixed Euler-Lagrange approach based BEM solver to model the ship motion problem in potential flow, and studied the non-linear free-surface effect on the corresponding hydrodynamic coefficients.

The potential theory based solvers are easy to implement. However, it is not appropriate for flows that involve shear, vortex and turbulence generation. In order to simulate wave propagation in real fluid with rotation and dissipation, a numerical model for solving the Navier-Stokes equation is needed. An explicit projection method was used in Li and Fleming (2001); Lin and Li (2002); Choi and Wu (2006) for predicting the water wave motion. In these studies, the MacCormack explicit scheme was used, and the equations were transformed from an irregular calculation domain to a regular one. Hendrickson (2005) performed a systematic study of a range of breaking waves by using Direct Numerical Simulation (DNS) of the Navier-Stokes equations coupled with an Eulerian interface capturing method.

The absorption of the incident wave at the outflow boundary is always a critical issue in the numerical simulation. Two numerical absorbing methods have been developed. One is the so-called numerical beach (adding dissipation terms), and the other implements an active paddle on the downstream boundary. Clement (1996) coupled these two methods and his approach leads to a very good absorption for all wave frequencies. Gentaz et al. (2000) presented the simulations of a two-dimensional wave tank in viscous flow. Exact nonlinear free-surface boundary conditions and the moving grid technique were used to simulate the wave propagation in a tank. A numerical damping method was used for wave absorption at the outlet boundary, where the down stream boundary is extended using a damping beach with stretched mesh.

The numerical simulation of unsteady and incompressible flows requires coupling the velocities and pressure. The well-known SIMPLE algorithm, presented by Patankar and Spalding (1972), is widely applied to solve the corresponding system equations, resulting from the finite volume or finite element discretization. An improved SIMPLE method was proposed by Van Doormaal and Raithby (1984), which provided a better

approximation on the calculation of the corresponding coefficients, and is known as SIMPLEC algorithm. Patankar (1980) and Issa (1986) later proposed two improvements on the SIMPLE algorithm, which are known as SIMPLER and PISO, respectively.

The application of the finite volume method always requires the interpolation of cell side values from cell center values. The simple and commonly used Central Differencing Scheme (CDS) leads to a significant loss in accuracy when the numerical grid is non-orthogonal (irregular) as the case when modeling complex geometries. Peric (1985) presented a detailed discussion on various differencing scheme that are employed for the evaluation of convection and diffusion fluxes. Peric (1990) proved that the efficiency of the SIMPLE coupling algorithm is not affected by the grid non-orthogonality. However, ignoring the grid-orthogonality while calculating the cell side values often results in a deteriorated convergence behavior of the overall pressure-correction scheme. Lehnhauser and Schafer (2002) suggested an alternative technique, based on a multi-dimensional Taylor series expansion that preserves the CDS-like sparsity pattern of the discrete system and provides a converged solution. The algorithm was later extended into three dimensions in Lehnhauser and Schafer (2003).

In many application areas, the solution domain changes with time due to the movement of the boundaries, i.e. free surface and moving hull. Many researchers highlighted the importance of taking the Geometric Conservation Law (GCL) into account with moving boundaries (Demirdzic and Peric 1988; Thomas and Lombard 1979). GCL states that the rate of change of the cell volume is equal to the volume swept by the cell boundaries. An excellent review on these studies can be found in Ferziger and Peric (2002). Related studies were also presented by Lesoinne and Farhat (1996); Farhat et al. (2001).

Chapter 3: Methodology

This chapter describes the governing equations, numerical methods and boundary conditions that are applied in the present numerical scheme. It is assumed that the flow is incompressible, and that the surface tension is neglected on the free surface. The flow field is predicted by solving the continuity equation and the Navier-Stokes equations. A cell-center-based Finite Volume Method (FVM) and a free-surface tracking algorithm, described in the following sections, are applied in the NS2D and NS3D solvers, which implement the methods developed in this work.

3.1 GOVERNING EQUATIONS

For unsteady incompressible flow, the integral representation of the three-dimensional continuity equation and Navier-Stokes equations are as follows:

$$\begin{aligned} \int_{CV} \nabla \cdot \vec{U} d\forall &= 0, \\ \int_{CV} \frac{\partial \vec{U}}{\partial t} d\forall + \int_{CV} \vec{U} \cdot \nabla \vec{U} d\forall &= -\frac{1}{\rho} \int_{CV} (\nabla p + \vec{F}_B) d\forall + \int_{CV} \nu \nabla^2 \vec{U} d\forall, \end{aligned} \quad (3.1)$$

where $\vec{U} = (u, v, w)$ is the total flow velocity vector with respect to the inertial coordinate system with (u, v, w) being the three velocity components respectively, \forall represents the volume of the control volume (CV), p stands for pressure, \vec{F}_B indicates the body force vector, (x, y, z) represent the three directions in the Cartesian coordinate system, ρ stands for density, which is assumed to be constant; ν represents the kinematic viscosity and t indicates time. Note that the gravity force is combined in the pressure gradient term. Also note that the present pressure indicates the hydrodynamic pressure

(gage pressure – hydrostatic pressure). Since gravity is absorbed into the pressure gradient term, the body force is set zero, $\vec{F} = 0$, in the present problem.

3.2 NUMERICAL FORMULATIONS

According to the primitive variable method, the momentum equations and the continuity equation are coupled and solved iteratively. FVM is applied on the collocated grids and it is combined with a pressure-correction scheme. Moving and deforming grids are used to follow the hull motion and to track the non-linear free surface. A second-order implicit scheme is used for time marching, and a second-order upwind scheme is applied for the convective terms in the momentum equations to provide better stability. For moving and deforming mesh, the cell-face motion terms are included and calculated by following the Geometric Conservation Law (GCL).

3.2.1 Finite Volume Method

A cell center based finite volume method is applied in the current numerical scheme, which provides a better accuracy for non-orthogonal grids and simplifies the treatment at the boundary. Moreover, it avoids the complexity of specifying the boundary condition at the common node of the hull and the free surface. The orientation of a three-dimensional cell is plotted in Figure 3.1. For a hexahedral cell with all its faces quadrilateral, a cell containing point P has six neighboring points, identified as west, east, south, north, bottom, and top points ($W, E, S, N, B,$ and T). The notations of $w, e, s, n, b,$ and t refer to the west, east, south, north, bottom, and top cell faces respectively.

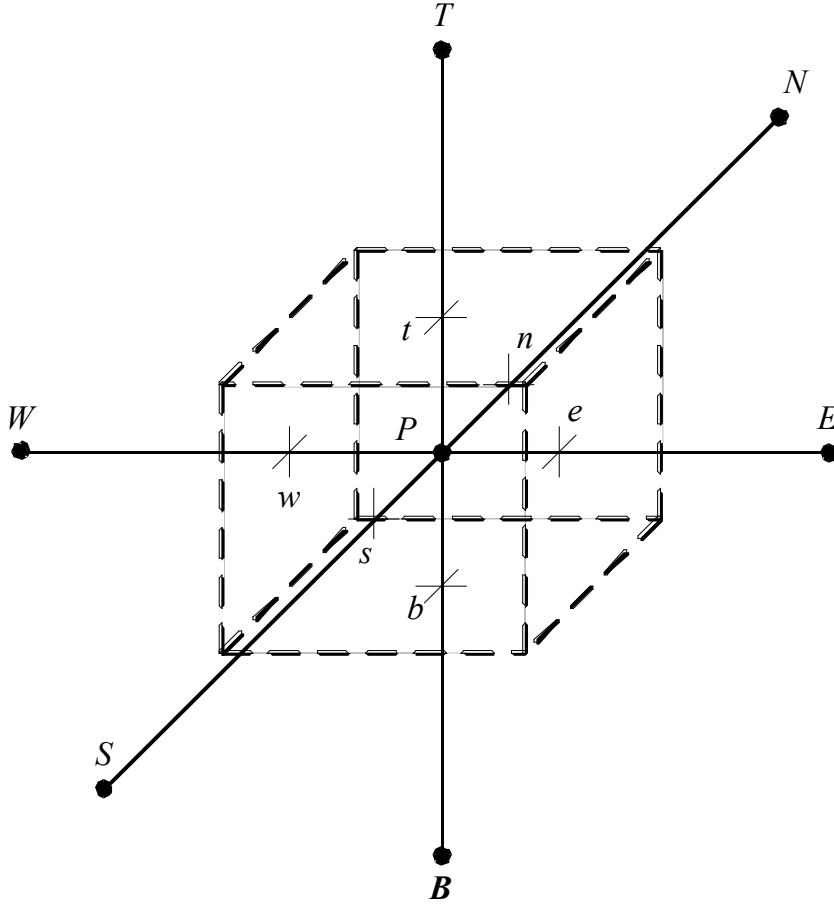


Figure 3.1: A cell in three-dimensions with its neighboring points and faces.

Based on the Gauss divergence theorem and considering a cell as a CV, the discrete representation of the continuity equation and the conservative form of the Navier-Stokes equations can be written as:

$$\begin{aligned}
 \sum_{\partial\forall} \dot{m} &= \sum_{\partial\forall} \rho(\vec{U}_f \cdot \vec{n}) A_f = 0 \\
 \frac{\partial \vec{U}_P}{\partial t} \forall + \sum_{\partial\forall} \left[v_n \vec{U}_f - v \left(\frac{\partial \vec{U}}{\partial n} \right)_f \right] A_f &= -\frac{1}{\rho} \sum_{\partial\forall} p_f \vec{n} A_f,
 \end{aligned} \tag{3.2}$$

where \dot{m} is the mass flux of each cell side, $\partial\forall$ represents the boundary of the CV, v_n is the normal velocity on the cell face, n means the direction normal to the cell face, \bar{n} is the unit normal vector to the cell face, subscripts " P " and " f " represent the values located at the cell center point P and at the center of the CV face and A_f is the area of the cell side. In two dimensions, the calculation of the CV volume is simple, but it becomes more complicated in three dimensions. The present scheme uses the approach described in Ferziger and Peric (2002) to calculate the 3D CV volume.

3.2.2 Moving and Deforming Mesh

Following Leibnitz and Gauss divergence theorems, the total change of any variable Φ , with both increments in time and the corresponding change in moving and deforming of the CV, is given as⁴:

$$\frac{\delta}{\delta t} \int \Phi d\forall = \int \frac{\partial \Phi}{\partial t} d\forall + \int_{\partial\forall} v_{gn} \Phi dA_f, \quad (3.3)$$

where v_{gn} is the normal component of the velocity of the CV boundary. Based on FVM, the discrete representation of Eq. (3.3) can be written as:

$$\begin{aligned} \frac{\delta(\Phi_P \forall)}{\delta t} &= \frac{\partial \Phi_P}{\partial t} \forall + \sum_{\partial\forall} v_{gn} \Phi_f A_f, \\ \Rightarrow \frac{\partial \Phi_P}{\partial t} \forall &= \frac{\delta \Phi_P}{\delta t} \forall + \Phi_P \frac{\delta \forall}{\delta t} - \sum_{\partial\forall} v_{gn} \Phi_f A_f, \end{aligned} \quad (3.4)$$

⁴ The symbol $\delta/\delta t$ is used to differentiate from that used in the case of the substantive derivative since the grid movement is also considered in this work.

where the first two terms on the right hand side of the equation are calculated by using a time marching scheme. As a special case, if $\Phi = \text{constant}$, the above equation becomes

$$\frac{\delta \forall}{\delta t} - \sum_{\partial \forall} v_{gn} A_f = 0. \quad (3.5)$$

It is the so-called Geometric Conservation Law (GCL), which states that the rate of change of the cell volume is equal to the volume swept by the cell boundaries. It is used to calculate the normal grid velocity, as contained in the last term of Eq. (3.4).

For calculating the rate of change of any variable, an implicit three-level second order time marching scheme is applied, where the time derivative at t^{m+1} can be approximated as a backward difference (same approach is applied for the rate of change of a CV volume):

$$\frac{\delta \Phi}{\delta t} = \frac{3\Phi^{m+1} - 4\Phi^m + \Phi^{m-1}}{2\Delta t}, \quad (3.6)$$

where Δt represents the time step size, the superscript " $m+1$ " represents the current time step, at which the unknown variables are evaluated, superscripts " m " and " $m-1$ " represent the previous time steps. Eq. (3.5) can be rewritten as:

$$\frac{3\forall^{m+1} - 4\forall^m + \forall^{m-1}}{2\Delta t} = \sum_{\partial \forall} v_{gn} A_f. \quad (3.7)$$

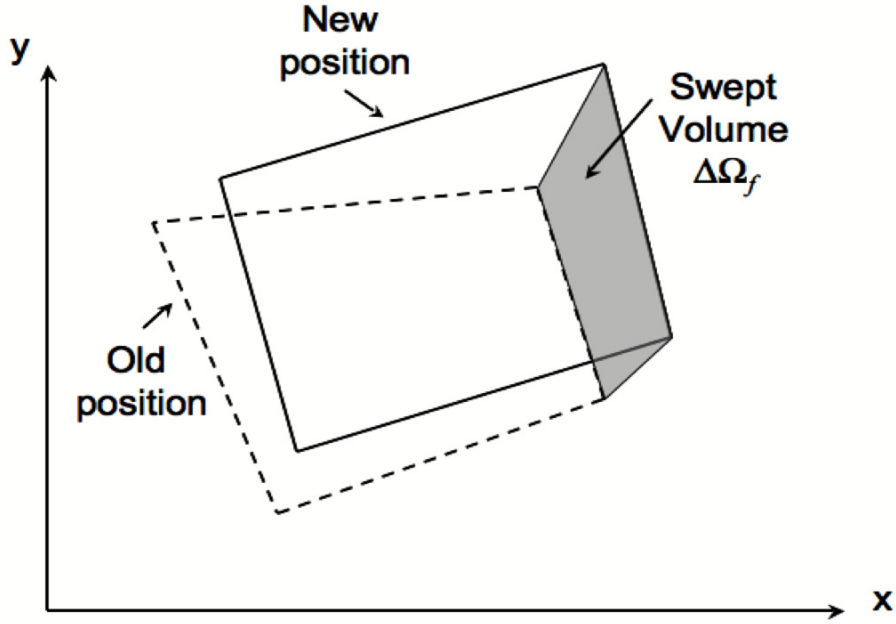


Figure 3.2: A typical 2D mesh at two time steps and the volume swept by an arbitrary cell face.

As shown in Fig. 3.2, the difference between the "new" and "old" cell volume at two time steps can be expressed as the sum of $\Delta\Omega_f$, swept by the CV faces. The rate of change of the cell volume can be further given as:

$$\frac{3\forall^{m+1} - 4\forall^m + \forall^{m-1}}{2\Delta t} = \frac{3(\forall^{m+1} - \forall^m) - (\forall^m - \forall^{m-1})}{2\Delta t} = \frac{\sum_{\partial\forall} (3\Delta\Omega_f^{m+1} - \Delta\Omega_f^m)}{2\Delta t}, \quad (3.8)$$

where $\sum_{\partial\forall} \Delta\Omega_f^{m+1} = \forall^{m+1} - \forall^m$; and $\sum_{\partial\forall} \Delta\Omega_f^m = \forall^m - \forall^{m-1}$. From Eq. (3.7) and Eq. (3.8), the normal grid velocity on each cell face is obtained:

$$v_{gn} = \frac{3\Delta\Omega_f^{m+1} - \Delta\Omega_f^m}{2A_f\Delta t}. \quad (3.9)$$

When Eq. (3.4) is substituted into Eq. (3.2), the discrete momentum equation can be re-written as:

$$\frac{\delta \bar{U}_P}{\delta t} \nabla + \bar{U} \frac{\delta \nabla}{\delta t} + \sum_{\partial \forall} \left[(v_n - v_{gn}) \bar{U}_f - v \left(\frac{\partial \bar{U}}{\partial n} \right)_f \right] A_f = -\frac{1}{\rho} \sum_{\partial \forall} p_f \bar{n} A_f, \quad (3.10)$$

3.2.3 Approximation of Fluxes and Cell Face Values

This section presents the procedure and formulations for calculating the cell face value, the normal derivative of any variable, and the convective flux. More details of the derivations of these equations are described in Appendix A.

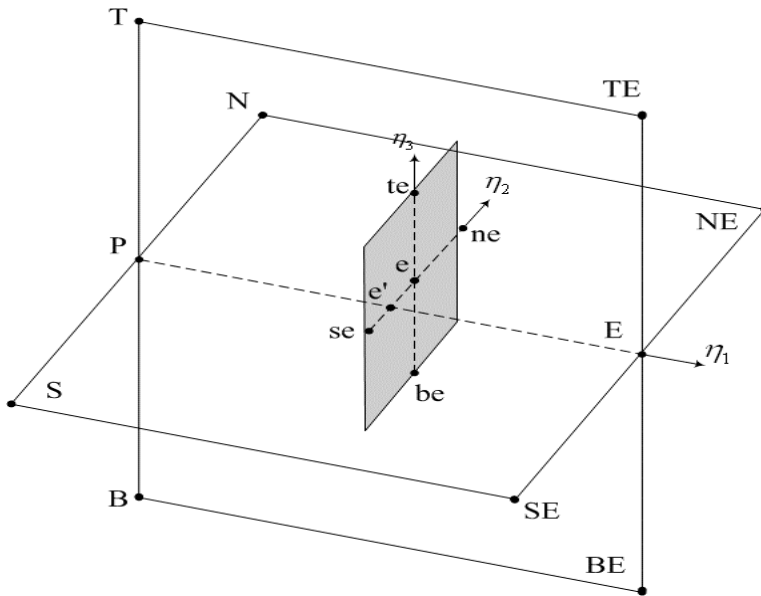


Figure 3.3: Arbitrary east face of a 3-D cell with the computational points.

The cases that involve interpolation of values at the center of a cell face are: (i) the calculation of the mass flux for each cell face required by the continuity equation; (ii) the calculation of the pressure and velocity gradients required by the momentum equations; (iii) the averaged pressure derivative with respect to the normal direction used in the pressure-correction method. Figure 3.3 shows an arbitrary east side of a 3-D cell with corresponding neighboring computational points. The simplest way to calculate the cell face value is by using the linear interpolation between the cell-containing point P and the neighboring point ($NB=W, E, S, N, T, B$) on either side of the cell face. However, when the grid is irregular, the line that connects P and NB for each cell face may not pass through the cell face center. As a result, the approximation to the surface integral is no longer accurate to second order. For any variable Φ , one can preserve the accuracy by using Taylor series expansion:

$$\Phi_f = \Phi_{f'} + \Delta\vec{X}_{f-f'} \cdot \nabla\Phi_{f'} + H \approx \Phi_{f'} + \Delta\vec{X}_{f-f'} \cdot \nabla\Phi_{f'}, \quad (3.11)$$

where H stands for higher-order terms, which are neglected, f' represents a point on the line between P and NB with:

$$\frac{|\Delta\vec{X}_{NB-f'}|}{|\Delta\vec{X}_{P-f'}|} = \frac{|\Delta\vec{X}_{NB-f}|}{|\Delta\vec{X}_{P-f}|}, \quad (3.12)$$

and $\Delta\vec{X}$ represents the distance vector between the two points. The values at point f' are calculated using linear interpolation between points P and NB on either side of the face:

$$\begin{aligned}\Phi_{f'} &\approx (C_P)_f \Phi_P + C_{NB} \Phi_{NB}, \\ \nabla \Phi_{f'} &\approx (C_P)_f \nabla \Phi_P + C_{NB} \nabla \Phi_{NB},\end{aligned}\tag{3.13}$$

where $(C_P)_f$ and C_{NB} are the corresponding coefficients. Based on the Gauss divergence theorem, the variable gradient can be written as: (the same approach applies for neighboring point NB)

$$\nabla \Phi_P \approx \frac{1}{\nabla} \sum_{\partial \nabla} \Phi_f \bar{n} A_f.\tag{3.14}$$

Note that the cell face value obtained from Eq. (3.13) will be mentioned hereafter as an interpolated value.

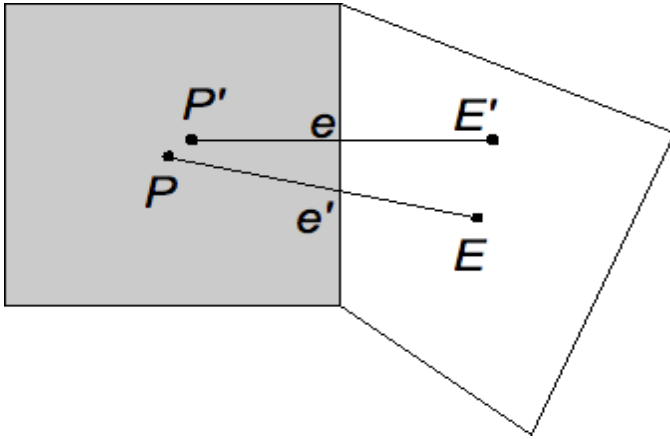


Figure 3.4: Arbitrary east face of a 2D cell with the computational points and their auxiliary points.

Both the diffusive flux term in the momentum equation and the velocity-correction term in the pressure-correction method require the calculation of the normal derivative of a variable at a cell-face center. Figure 3.4 shows an arbitrary east side of a 2D cell with the computational points and their auxiliary points, where " ' " indicates the

auxiliary points. For a cell with arbitrary shape, the normal derivative of any variable Φ on the cell face can be approximated as a central difference:

$$\left(\frac{\partial\Phi}{\partial n}\right)_f \approx \frac{\Phi_{NB'} - \Phi_{P'}}{(\vec{X}_{NB'} - \vec{X}_{P'}) \cdot \vec{n}}, \quad (3.15)$$

where \vec{X} represents the position vector. The auxiliary points P' and NB' are defined as:

$$\begin{aligned} (\vec{X}_{P'})_f &= \vec{X}_f - [(\vec{X}_f - \vec{X}_{P'}) \cdot \vec{n}] \vec{n}, \\ \vec{X}_{NB'} &= \vec{X}_f - [(\vec{X}_f - \vec{X}_{NB'}) \cdot \vec{n}] \vec{n}. \end{aligned} \quad (3.16)$$

The calculation of the convective flux for each cell face is required in the momentum equations. In order to identify the flow direction and to stabilize the numerical scheme, a second order upwind scheme is applied. The cell-face flow velocity vector for the convective term is also calculated through Taylor series expansion, but with an additional direction coefficient C_{up} , where

$$\begin{aligned} \vec{U}_f &\approx C_{up}(\vec{U}_P + \Delta\vec{X}_{f-P} \cdot \nabla\vec{U}_P) + (1 - C_{up})(\vec{U}_{NB} + \Delta\vec{X}_{f-NB} \cdot \nabla\vec{U}_{NB}), \\ C_{up} &= 0.5(v_n + |v_n|) / v_n, \end{aligned} \quad (3.17)$$

Using FVM, the implementations of Eq. (3.6), Eq. (3.15), and Eq. (3.17) in Eq. (3.10) yield a system algebraic equation of the momentum equation:

$$\begin{aligned} a_P \vec{U}_P + \sum_l a_l \vec{U}_l &= -\frac{1}{\rho} \sum_{\partial\forall} p_f \vec{n} A_f + \hat{a}_P \nabla \vec{U}_P + \sum_l \hat{a}_l \nabla \vec{U}_l, \\ l &= \text{surrounding cells}, \end{aligned} \quad (3.18)$$

where a_p , a_l , \hat{a}_p and \hat{a}_l are the corresponding coefficients and the subscript " l " represents the surrounding cells, which includes all the NB points and the neighboring points around each NB point. When the grid is regular (f and f' on each cell face are located at the same point), the coefficients with " $\hat{\cdot}$ " are equal to zero, and the above equation can be solved by itself. Otherwise, an iterative procedure is required, and Eq. (3.18) has to be solved iteratively with Eq. (3.14) until it reaches the convergence criterion.

3.2.4 Pressure-Correction Method

A pressure-correction method (SIMPLEC algorithm) is used to correct the velocities on each cell face and to calculate the pressure at the cell center point P . The acronym SIMPLE stands for Semi-Implicit Method for Pressure-Linked Equations, and the algorithm was developed by Patankar and Spalding (1972). The acronym C indicates the modification of the scheme on the approximation of the coefficients (Van Doormaal and Raithby 1984). The pressure-correction term is obtained by forcing the corrected normal velocity on the cell face to satisfy the continuity equation with a guess-and-correct procedure. The correction equations are given as:

$$\begin{aligned}
 p &= \tilde{p} + p', \\
 v_n &= \tilde{v}_n + v'_n, \\
 v'_n &= -d_f \left(\frac{\partial p'}{\partial n} \right)_f
 \end{aligned} \tag{3.19}$$

where the superscript " $'$ " indicates the correction term, " $\tilde{\cdot}$ " represents the provisional value and d_f is the corresponding coefficient. The scheme is known as SIMPLEC

algorithm if $d_f = a_p + \sum_l a_l$ (Van Doormaal and Raithby 1984). According to FVM, the sum of the mass flux through each cell face is given as:

$$\sum_{\partial\forall} \dot{m}_f \sum_{\partial\forall} v_n A_f = \sum_{\partial\forall} (\tilde{v}_n + v'_n) A_f = 0. \quad (3.20)$$

The equation is formed into a Poisson's equation of pressure-correction terms, which will be mentioned hereafter as the pressure-correction equation. Using Eq. (3.15) with $\Phi = p'$, the discrete algebraic equation becomes:

$$h_p p'_p + \sum_l h_l p'_l = \sum_{\partial\forall} \tilde{v}_n A_f + \hat{h}_p \nabla p'_p + \sum_l \hat{h}_l \nabla p'_l, \quad (3.21)$$

$l = \text{surrounding cells},$

where h_p , h_l , \hat{h}_p and \hat{h}_l denote the corresponding coefficients. The numerical scheme is based on a non-staggered grid, where all the unknown variables are located at the cell center. Note that when \hat{h}_p and \hat{h}_l are equal to zero, the above equation can be solved directly. Otherwise, the same iterative approach, as applied in Eq. (3.18), is used for Eq. (3.21). In order to avoid the checkerboard pressure problem, the normal component of the interpolated cell-face velocity is thus modified by the difference between the normal component of the interpolated pressure gradient and the normal pressure derivative calculated at the cell face:

$$\tilde{v}_n = \bar{U}_f \cdot \bar{n} + d_f \left[\overline{(\nabla p)}_f \cdot \bar{n} - \left(\frac{\partial p}{\partial n} \right)_f \right], \quad (3.22)$$

where the overbar indicates the interpolated value at the cell face. The procedure of the pressure-correction algorithm can be summarized as follows:

1. Start the calculation of the field at new time step $m+1$ using the latest solution \bar{U}^m and p^m as starting estimates (the provisional value) for \bar{U}^{m+1} and p^{m+1}
2. Assemble and solve the linearized system of the algebraic equations (momentum equations) for new \bar{U}^{m+1} .
3. Assemble and solve the pressure-correction equation (continuity equation/ Poisson's equation) for p' .
4. Correct the normal velocity at the cell face center and the pressure value at the cell center point P .
5. Repeat step 2~4, by using the latest solution as updated estimates (the provisional value) for \bar{U}^{m+1} and p^{m+1} , until all the corrections are smaller than a predefined threshold.
6. Move on to the next time step.

The linear sparse systems of the equations resulting from the Poisson equation and the momentum equations are then solved using Generalized Minimal Residual (GMRES) algorithm. Note that all variables in NS2D/NS3D are made non-dimensional by using reference scales. More details are described in Appendix B.

3.3 BOUNDARY CONDITIONS

This section describes three types of boundary conditions that are used in study: the velocity inlet, the wall boundary (stationary/moving), and the free surface. In the present numerical scheme, all the values on the domain boundaries are calculated at the center of the cell face.

3.3.1 Velocity Inlet and Wall Boundaries

For the velocity inlet, each velocity component is specified. For a stationary or a moving wall, a kinematic boundary condition is applied so that the flow does not penetrate the hull geometry:

$$v_n = v_{gn}, \text{ on the domain boundary,} \quad (3.23)$$

In the case of viscous flow, a no-slip boundary condition is applied, where the fluid particle velocities on the wall are consistent with the hull velocities. In the case of inviscid flow, the tangential velocity is calculated using Taylor series expansion. Based on FVM, the discrete formulation is given as:

$$\begin{aligned} v_s &= \vec{U}_{DB} \cdot \vec{s}, \\ v_s &\approx (\vec{U}_P + \Delta\vec{X}_{DB-P} \cdot \nabla\vec{U}_P) \cdot \vec{s}, \\ \Rightarrow \left(1 - \frac{\Delta\vec{X}_{DB-P} \cdot \vec{n}A_f}{\nabla} \right) v_s &\approx \vec{U}_P \cdot \vec{s} + \Delta\vec{X}_{DB-P} \cdot \frac{1}{\nabla} \sum_{\partial\forall \neq DB} (\vec{U}_f \cdot \vec{s}) \vec{n}A_f, \end{aligned} \quad (3.24)$$

where the subscript "DB" represents the value on the domain-boundary cell face, $\partial\forall \neq DB$ represents all the cell sides except the one on the domain boundary, v_s is the

tangential component of the flow velocity at the cell face center on the domain boundary and \vec{s} denotes the unit tangential vector to the cell face on the domain boundary. Note that the tangential vector in 2D can be determined easily using the distance vector between two node points on the domain-boundary cell face. In the case of 3D, however, more than one tangential vector exists on the domain-boundary cell face. Each unit tangential vector is obtained using the distance vector between the center point and any node point on the domain-boundary cell face:

$$\vec{s} = \frac{\Delta\vec{X}_{f-tn}}{|\Delta\vec{X}_{f-tn}|}, \quad (3.25)$$

where the subscript "tn" denotes any node point on the domain-boundary cell face. The normal component and any two tangential components of the flow velocity are used to solve the corresponding \vec{U}_{DB} . Note that using this approach, all the node points on each domain-boundary cell face except for the free surface boundary are assumed to be on the same plane. Pressure on all domain boundaries except on the free surface is obtained from linear extrapolation of the values at the internal cells, which is given as:

$$\begin{aligned} p_{DB} &\approx p_P + \Delta\vec{X}_{DB-P} \cdot \nabla p_P, \\ \Rightarrow \left(1 - \frac{\Delta\vec{X}_{DB-P} \cdot \vec{n}A_f}{\nabla} \right) p_{DB} &= p_P + \Delta\vec{X}_{DB-P} \cdot \frac{1}{\nabla} \sum_{\partial\forall \neq DB} p_f \vec{n}A_f. \end{aligned} \quad (3.26)$$

3.3.2 Free Surface boundary

The non-linear boundary conditions are applied on the free surface, where the Kinematic Free Surface Boundary Condition (KFSBC) and the Dynamic Free Surface Boundary Condition (DFSBC) are given as:

$$\begin{aligned} \text{KFSBC: } v_{FSn} - v_n &= 0, \\ \text{DFSBC: } p_{ap} &= p - \rho g \eta = 0, \end{aligned} \quad (3.27)$$

where η represents the wave height; v_{FSn} is the normal component of the free surface velocity. KFSBC indicates that v_{FSn} is equal to the normal component of the flow velocity at the free surface. DFSBC states that when the surface tension is neglected, the total pressure on the free surface is equal to atmospheric pressure p_{ap} . For consistency, the gravity force is defined in the y-direction in both NS2D and NS3D. On the free surface, the pressure-correction term becomes zero when pressure is specified using DFSBC. Thus, the pressure-correction value at cell center point P in each free-surface cell is interpolated using Taylor series expansion, which leads to:

$$\begin{aligned} p'_{FS} = 0 &\approx p'_P + \Delta \bar{X}_{FS-P} \cdot \nabla p'_P, \\ \Rightarrow p'_P - \Delta \bar{X}_{FS-P} \cdot \frac{1}{\nabla} \sum_{\partial \nabla \neq FS} \bar{n} p'_f A_f, \end{aligned} \quad (3.28)$$

where the subscript "FS" indicates the value on the free-surface cell face and $\partial \nabla \neq FS$ represents all the cell sides except the one on the free surface. To calculate the pressure-correction term, Eq. (3.28) is applied instead of the pressure-correction equation, and the mass conservation for each free-surface cell is used for calculating the mass flux through the free surface:

$$\dot{m}_{FS} \approx \rho(v_n A_f)_{FS} = - \sum_{\partial V \neq FS} \rho(v_n A_f). \quad (3.29)$$

In this way, mass is still conserved both globally and in each cell, and the normal component of the flow velocity on the free surface is obtained.

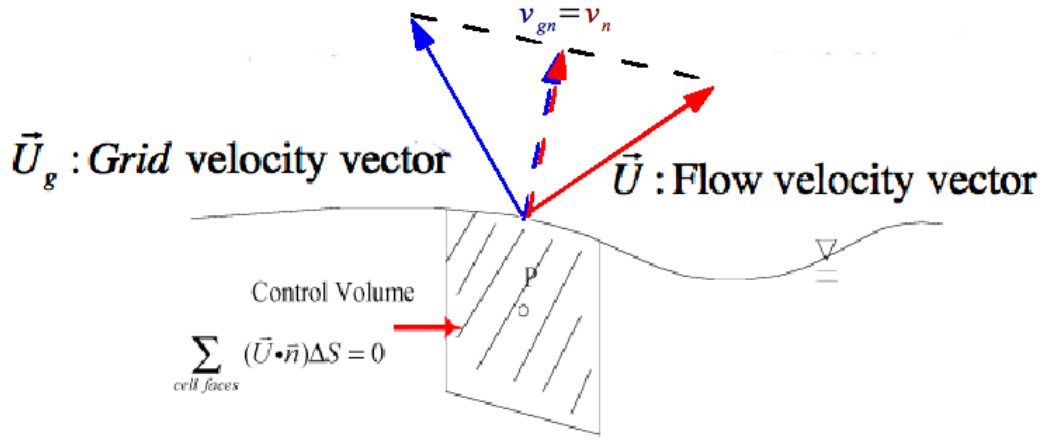


Figure 3.5: Kinematic Boundary Condition on the Free Surface.

As shown in Fig. 3.5, NS2D/NS3D applies a free-surface tracking algorithm, where the normal grid velocity on the free surface is assumed to be equal to the normal free-surface velocity as well as the normal flow velocity on the free surface. KFSBC then becomes the following wave equation, which describes the rate of change of the wave elevation:

$$\begin{aligned} v_{FSn} = v_{gn} = v_n &= \frac{\dot{m}_{FS}}{\rho(A_f)_{FS}}, \\ \Rightarrow v_g n_y &= \frac{\dot{m}_{FS}}{\rho(A_f)_{FS}} - u_g n_x - w_g n_z, \\ \Rightarrow \frac{\delta \eta}{\delta t} = v_g &= \frac{\dot{m}_{FS}}{\rho(A_f)_{FS} n_y} - u_g \frac{n_x}{n_y} - w_g \frac{n_z}{n_y}, \end{aligned} \quad (3.30)$$

where (n_x, n_y, n_z) are the Cartesian components of \vec{n} and (u_g, v_g, w_g) indicate the Cartesian components of the grid velocity. The wave elevation at t^{m+1} is obtained from the equation above by following the second-order three-time-level implicit scheme. Within the pressure-correction algorithm, the procedure used in NS2D/NS3D for calculating the fully non-linear free surface follows (modifications of the pressure-correction algorithm are made only on those **cells along the free surface**):

1. While solving the momentum equations, pressure on the free surface is specified by following DFSBC. Since the surface tension is neglected, the viscous terms are excluded from the momentum equations.
2. Instead of solving the pressure-correction equation, Eq. (3.26) is applied for calculating p' .
3. Enforce the local mass conservation in each cell on the free surface to calculate the normal flow velocity v_n .
4. Correct the position of the free surface to enforce KFSBC, and re-mesh.
5. Move on to the next pressure-correction iteration if necessary.

A similar approach was described in Ferziger and Peric (2002). As they mentioned, the critical issue of this procedure is the algorithm for the movement of the free surface. The problem is that there is only one discrete equation per free-surface cell but more than one node on the free-surface cell face needs to be moved. In the present scheme, the wave height for each cell is not calculated at those vertices but at the cell-face center. 2D structured grids are used as an example, which is illustrated in Fig. 3.6, where L_0 and L_1 are the vertices on the free surface and one level below the free surface respectively. After solving Eq. (3.30), the new node position on each free-surface cell face is located at

the intersection of $y=\eta$ and the line passes through each L_0 and L_1 vertices. However, for the same vertex, a different location is predicted from different cells, which results in an elevation jump among the free-surface cells. The averaged vertex location on the free surface is then defined by interpolating wave elevation for each associated cell with weighted cell-face area (length in 2D). The new free-surface position is shown in Fig. 3.6 as the dashed line, and those cells below the free surface are smoothed using an exponential distribution. Therefore, structured quadrilateral cells are required in x - y and y - z planes for those cells close to the free surface. The advantage of using this scheme is that it is straightforward and easy for coding. However, the cell-face center on the free surface and the wave elevation for each free-surface cell face are not necessarily located at the same point. The difference between the two positions is negligible when the free-surface movement is small within one time step, which puts a constraint on the time step size in NS2D/NS3D.

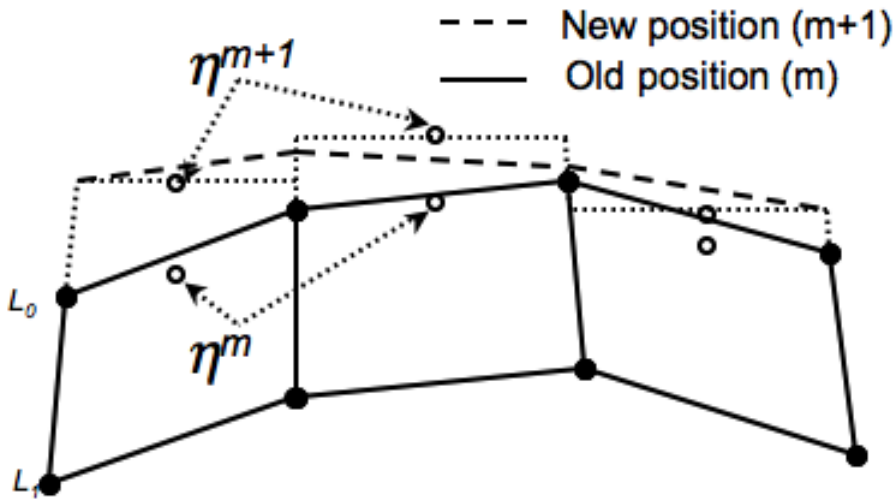


Figure 3.6: 2D cells under the free surface, and the free-surface position.

Chapter 4: Verification and Validation of NS2D

For verification and validation purposes, the modeling of 2D flow around a ship-shaped hull is simplified into two types of simulations. In the first type of simulation, the study is performed in the case of a submerged body, where the free surface effect is excluded. Three validation cases are performed for the submerged body simulations: vertical plate subject to alternating inflow, submerged hull subject to oscillating inflow, and submerged hull subject to prescribed roll. The other type of simulation is conducted on a wave-maker problem. The purpose of this type of simulation is to validate the free-surface tracking algorithm used in NS2D. The results from NS2D are then compared against those from the commercial CFD tool FLUENT and other existing experimental data.

4.1 VERTICAL PLATE SUBJECT TO ALTERNATING INFLOW

In the oscillating flow problem, the objective is to understand the physics of the separated flow about the bilge keels of a hull in a simplified geometry where the vertical plate can be viewed as a slender bilge keel placed on a flat wall without the presence of the free surface. This section describes the background and the NS2D simulation of the vertical plate problem. The results from the NS2D simulation are compared to the experimental measurements provided by Sarpkaya and Okeefe (1996) for different Keulegan-Carpenter numbers.

4.1.1 Background

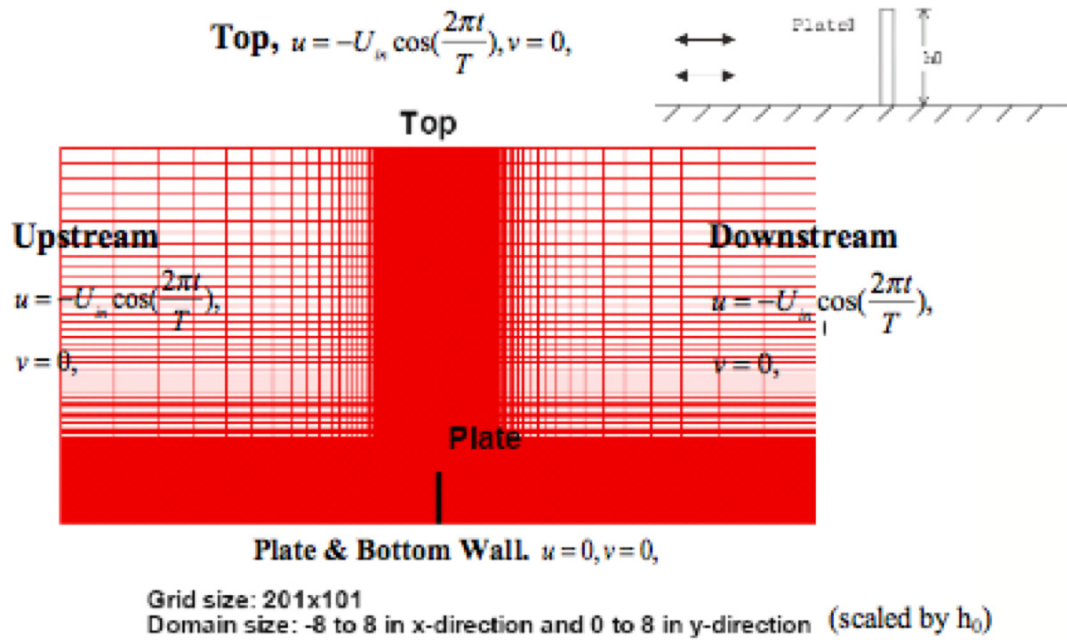


Figure 4.1: Grid and domain orientation for the vertical plate problem.

Sarpkaya and Okeefe (1996) performed an experimental study by putting a thick aluminum plate inside a U-shaped water tunnel consisting of a 0.91m wide, 1.42m high and 0.67m long horizontal section, and two vertical legs of 0.91m by 1.83m by 7.62m. The test body is 6mm thick, 0.91m wide and 102 mm high, and is subject to a horizontal sinusoidal inflow. Figure 4.1 presents the fluid domain and the corresponding boundary conditions used in the NS2D solver. The domain is $16h_0$ long and $8h_0$ tall, and is meshed with 201×101 structured cells. The domain is chosen this way so that the vortices created by the separated flow around the plate would not reach the upstream, downstream and top boundaries. All the variables in the NS2D simulation are made non-dimensional with respect to the plate height h_0 and the sinusoidal inflow amplitude U_{in} . The corresponding Reynolds number in the NS2D solver is therefore defined as

$Re = U_{in} h_o / \nu$. According to Sarpkaya and Okeefe (1996), the Keulegan-Carpenter number for the plate problem is defined as $KC = U_{in} T_{in} / h_o$, where T_{in} is the period of the sinusoidal inflow, and the frequency ratio β is given as $Re/KC=1845$. In the following studies, KC ranges from 0.5 to 10, and the corresponding Reynolds number ranges from 992.5 to 18450, respectively.

4.1.2 Force and Error Calculations

The force caused by the sinusoidal inflow exerted on the plate can be expressed by Morison's equation. Following Sarpkaya and Okeefe (1996), the non-dimensional formulation is given as:

$$\frac{2F_p}{\rho h_o U_{in}^2} = -C_d |\cos \theta| \cos \theta + C_m \frac{2\pi^2}{KC} \sin \theta, \quad (4.1)$$

where $\theta = 2\pi t / T_{in}$, F_p represents the horizontal force acting on the plate, C_d and C_m are the drag and inertia coefficients, respectively. The drag and inertia coefficients are extracted from the force history by using Fourier analysis:

$$\begin{aligned} C_d &= -\frac{3}{4} \int_0^{2\pi} \frac{F_p \cos \theta}{\rho h_o U_{in}^2} d\theta, \text{ Drag coefficient,} \\ C_m &= \frac{2KC}{\pi^3} \int_0^{2\pi} \frac{F_p \sin \theta}{\rho h_o U_{in}^2} d\theta, \text{ Inertia coefficient,} \end{aligned} \quad (4.2)$$

where the force is calculated by integrating the pressure along the plate surface $\partial\Gamma$:

$$F_p = \int_{\partial\Gamma} p n_x d\Gamma, \quad (4.3)$$

where Γ is the plate surface length.

As to the convergence analysis, the force history with the highest grid resolution is used as the "exact" solution. The error difference ε_F between the "exact" solution and the force history from another grid resolution is defined as:

$$\varepsilon_F = \frac{1}{N_T} \sqrt{\sum_{i=1}^{N_T} (F_c - F_e)_i^2}, \quad (4.4)$$

where N_T is the number of the time steps per period, F_e indicates the "exact" force value, F_c represents the force value from a coarser grid and the subscript "i" represents the time index at each time step.

4.1.3 Results

As shown in Fig. 4.2, the sensitivity analyses in space and in time are performed in order to validate the numerical scheme. The top figure shows the force histories with different cell sizes in the vertical direction, where the number of the grids on the plate surface is proportional to the cell numbers in the vertical direction. The bottom figure presents the semi logarithmic plot of the error difference for different total numbers of cells by following Eq. (4.4), where the result of 200×150 grid is used as the "exact" solution. The slope of the convergence rate is about 2, which is consistent with the second-order accurate scheme in space, as used in the NS2D solver. As a result, the resolution of 100 cells in the vertical direction (20 cells on the plate surface) is sufficient

for this particular plate problem. The comparison of the force histories with different grid resolutions in the horizontal direction is shown in Fig. 4.3, and the sensitivity analysis in time step size is presented in Fig. 4.4. As shown in these convergence studies, a grid size of 200×100 and a time step size of $0.001T$ are adequate, and thus will be implemented in the subsequent vertical plate problems.

The predicted flow fields for $KC=1$ from NS2D are shown in Fig. 4.5. A pair of counter-rotating vortices is formed at the edge of the plate, which then sheds away in the diagonal direction, either to the left or the right side of the plate. These vortex structures resemble qualitatively to those drawn in Sarpkaya and Okeefe (1996). The drag and the inertia coefficients obtained from NS2D for a range of KC numbers are presented in Fig. 4.6 and Fig. 4.7. These coefficients are calculated from the force history using Eq. (4.2). The result shows that the coefficients predicted from NS2D are close to those from the experiments of Sarpkaya and Okeefe (1996). The NS2D results are considered validated in the vertical plate problem. In the next section, and the solver will be applied to a case with a more complex geometry, fixed submerged hull problem.

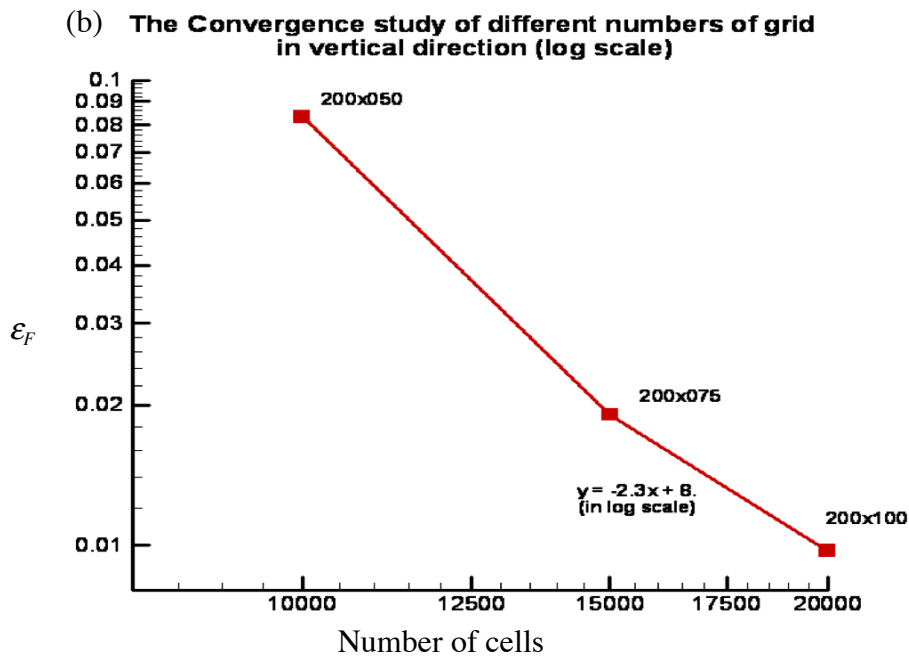
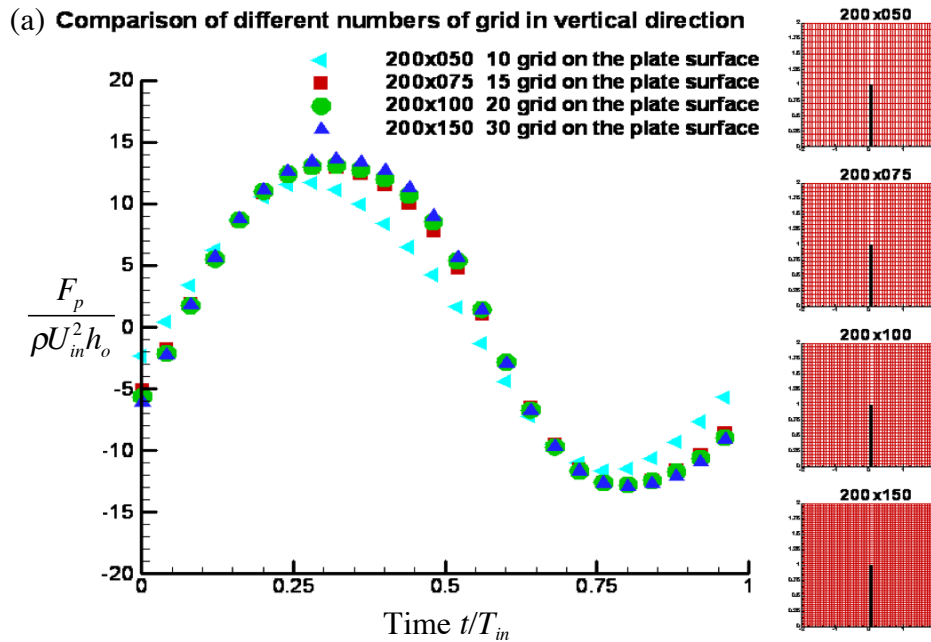


Figure 4.2: Convergence studies in space with different grid resolutions in the vertical direction. (a) Non-dimensional force histories, (b) logarithmic plot of ϵ_F for different numbers of cells.

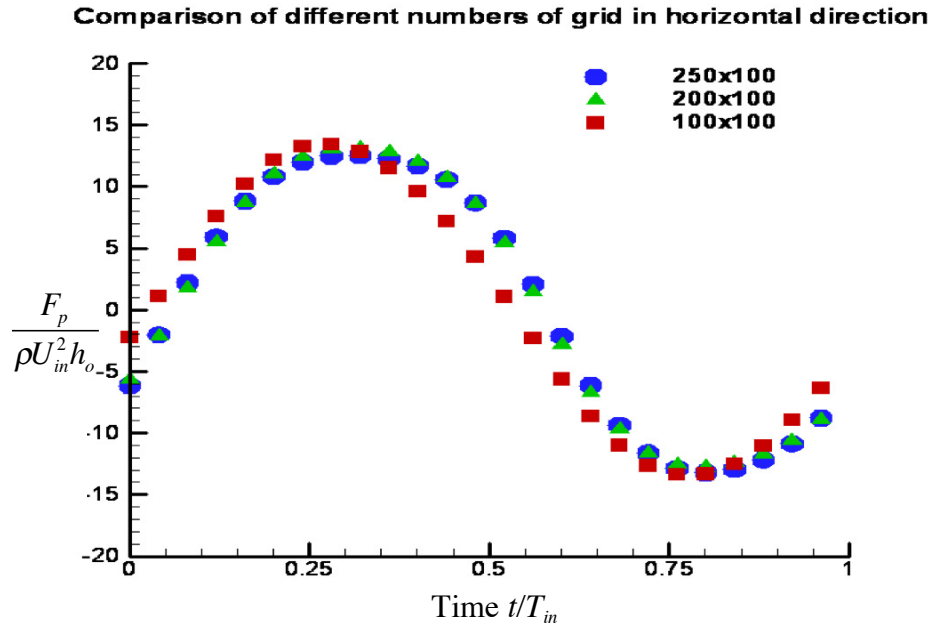


Figure 4.3: Convergence studies on non-dimensional forces over one period with different number of cells in the horizontal direction of the domain.

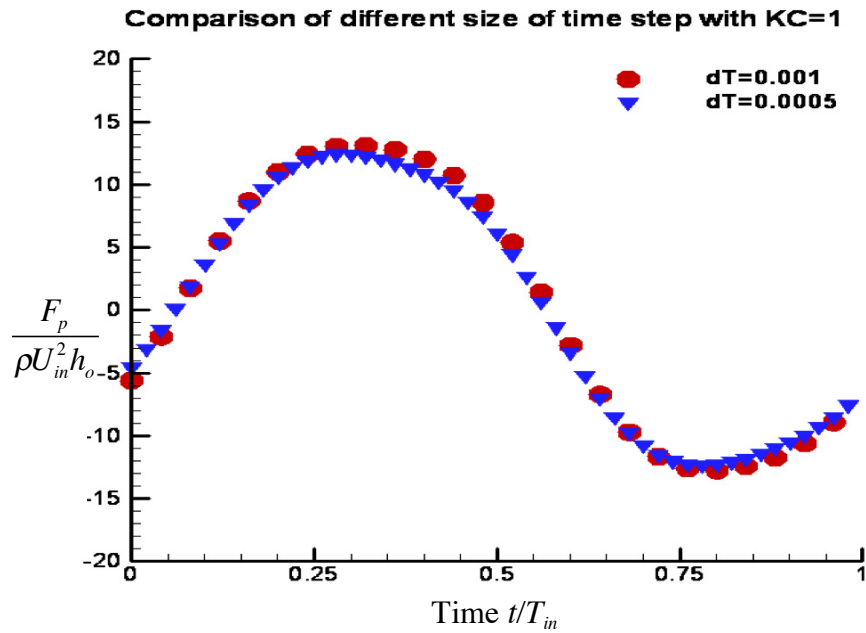


Figure 4.4: Convergence studies on non-dimensional forces over one period with different time step sizes.

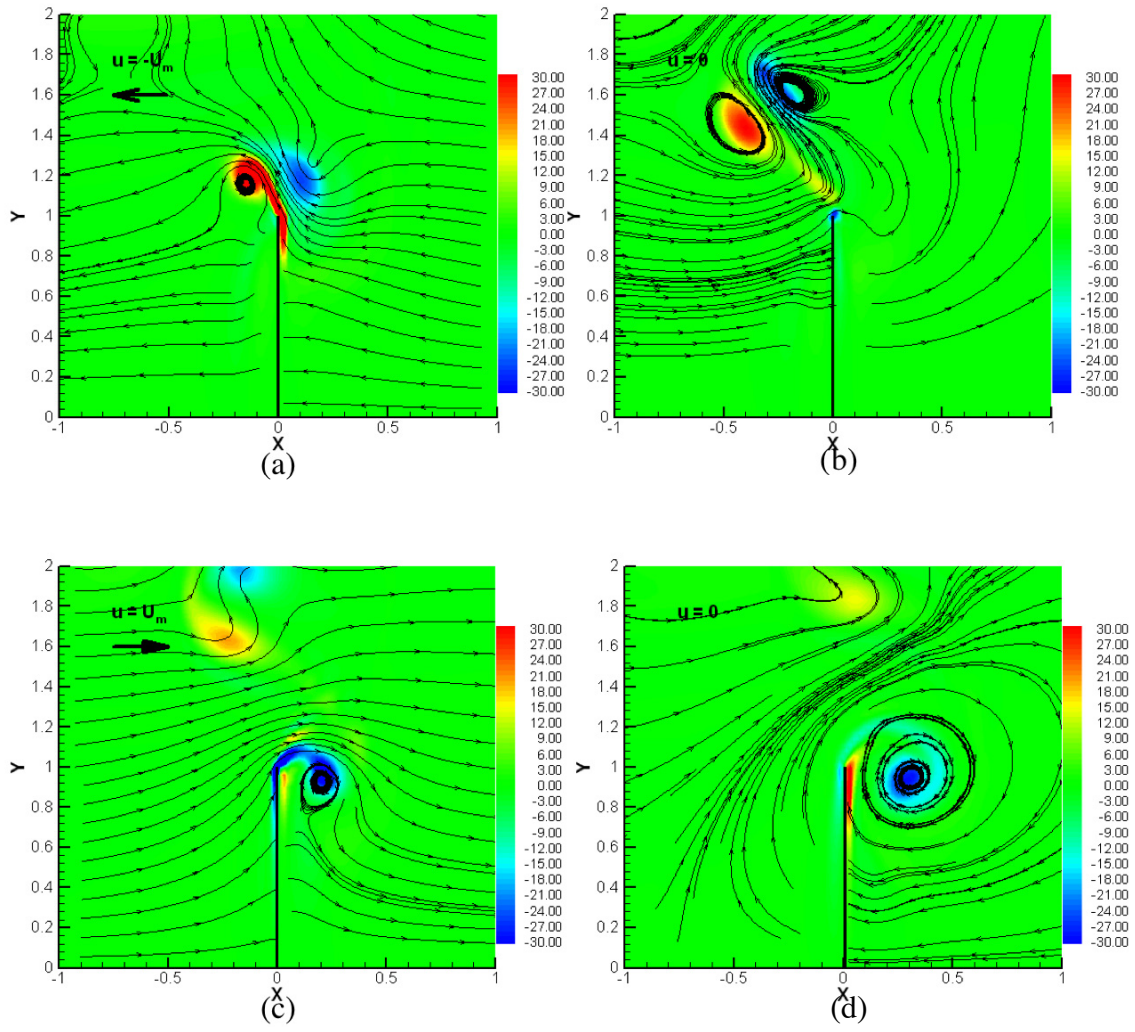


Figure 4.5: Streamline and vorticity contour plots predicted by NS2D solver with $KC=1$ at (a) start of the period, (b) quarter of the period, (c) half of the period, (d) 3/4 of the period.

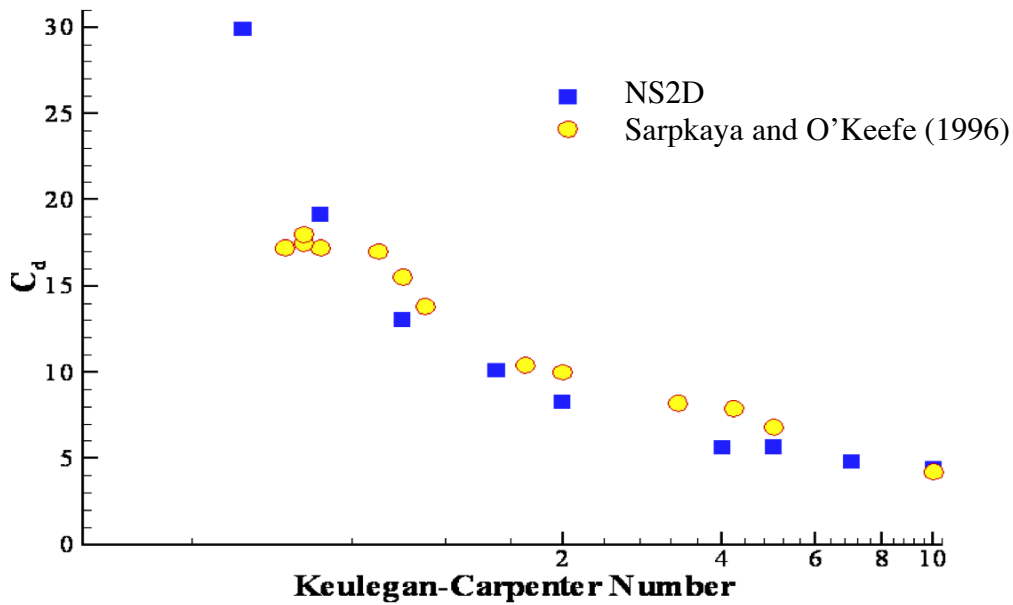


Figure 4.6: Comparison between the drag coefficients obtained from the NS2D solver and from measurements by Sarpkaya and O'Keefe (1996) in the case of oscillating flow past a flat plate problem.

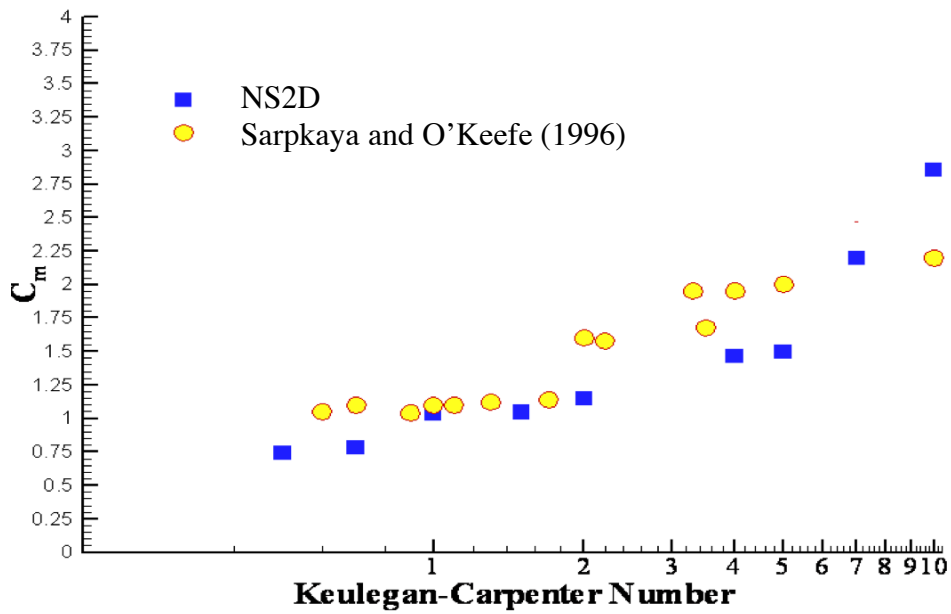


Figure 4.7: Comparison between the inertia coefficients obtained from the NS2D solver and from measurements by Sarpkaya and O'Keefe (1996) in the case of oscillating flow past a flat plate problem.

4.2 SUBMERGED HULL SUBJECT TO OSCILLATING INFLOW

The second validation test for NS2D in the submerged problem group can be viewed as a simplified case or a pre-test case for the FPSO hull roll motion problem. In this section, the results from the NS2D simulation are compared to those from the commercial software FLUENT in laminar and turbulent flow conditions.

4.2.1 Background

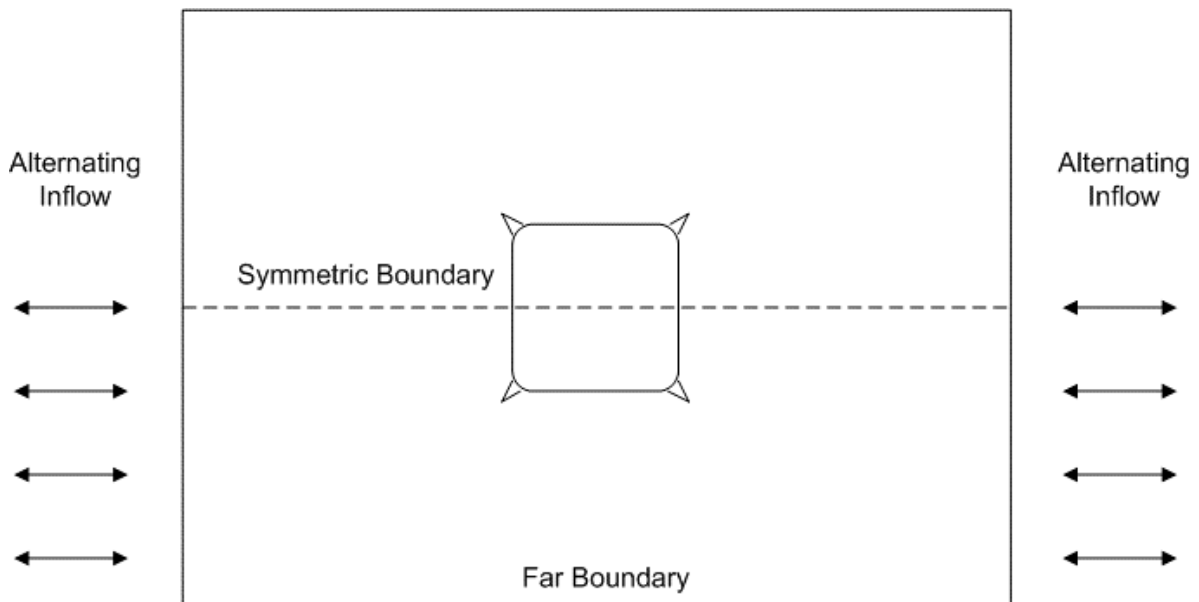


Figure 4.8: Fluid domain and corresponding domain boundaries of a *submerged* hull subject to alternating flow.

The 4% bilge keel model, will be described in subsection 5.1.2, is implemented in the problem of a submerged hull subject to oscillating inflow. The hull geometry and the mesh are similar to those used in the FPSO hull roll motion problem, except that the domain size is smaller in this case. The flow domain and its corresponding boundaries are

shown in Fig. 4.8. The free surface is excluded and replaced by a symmetric boundary in this case. All the variables in this case are made non-dimensional regarding to hull beam B and the period T_{in} of the sinusoidal inflow, where the amplitude of the sinusoidal inflow is given as $U_{in} = 0.1B / T_{in}$. The domain size is $8B$ long and $4B$ wide. The corresponding Reynolds number is defined as $Re = B^2 / (\nu T_{in})$, and it ranges from 10^3 to 10^6 .

4.2.2 Results

The pressure distributions along the fixed submerged hull predicted from NS2D and FLUENT at $t/T=1.75$ are presented in Fig. 4.9. The Reynolds number in both simulations is equal to 10^5 , and identical mesh is used for both runs. The results from NS2D compare well with those from FLUENT. As shown in Fig. 4.10, more studies are conducted only using FLUENT, in which the Reynolds stress model with standard wall function is applied to study the turbulent flow effect. The corresponding y-plus for the grid used in this case is around 40. The result shows significant deviation from others when the Reynolds number drops to 10^3 and the flow is laminar, and the turbulent flow effect has been found to be insignificant. For cases with such a low Reynolds number, it is beyond the scope of this study and will not be discussed further. In the following section, more studies on the submerged hull problem will be investigated, where the hull is subject to prescribed roll motions, and more studies on the effect of turbulent flow will be also addressed.



Figure 4.9: Pressure distributions along the fixed submerged hull subject to alternating inflow from NS2D and FLUENT at $t/T_{in}=1.75$ ($Re = 10^5$).

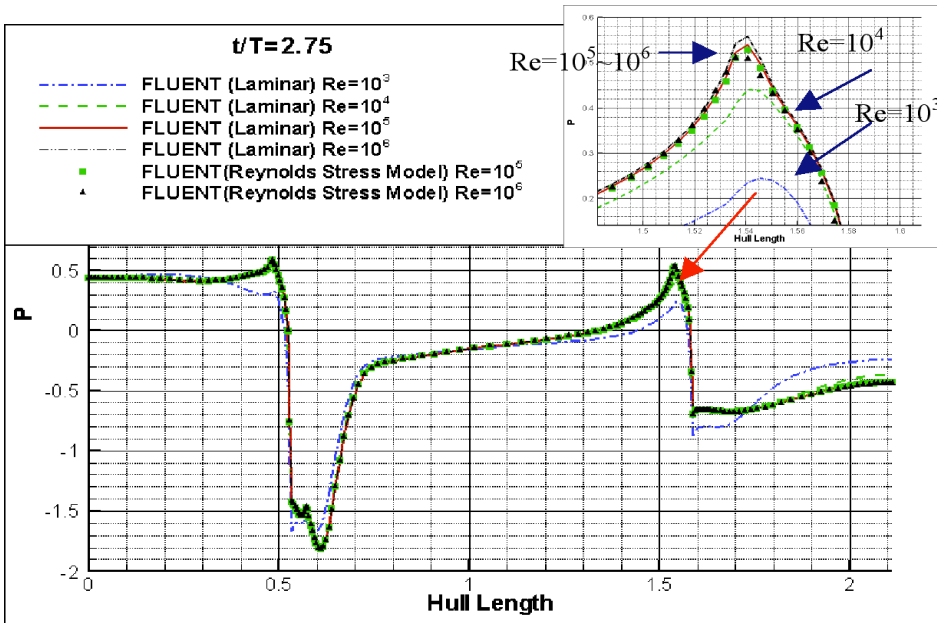


Figure 4.10: Pressure distributions along the fixed submerged hull subject to alternating inflow from FLUENT at different Reynolds numbers (Laminar or Turbulent flow) at $t/T_{in} = 2.75$.

4.3 PRESCRIBED ROLL MOTION OF A SUBMERGED HULL

The third validation case for NS2D in the submerged problem group is performed in this section, where the submerged round bilge hull (hull bilge geometry will be explained in subsection 5.1.2) is subject to prescribed roll motions. The correlation between the results from NS2D and FLUENT is presented, and the turbulent flow effect is studied using FLUENT.

4.3.1 Background

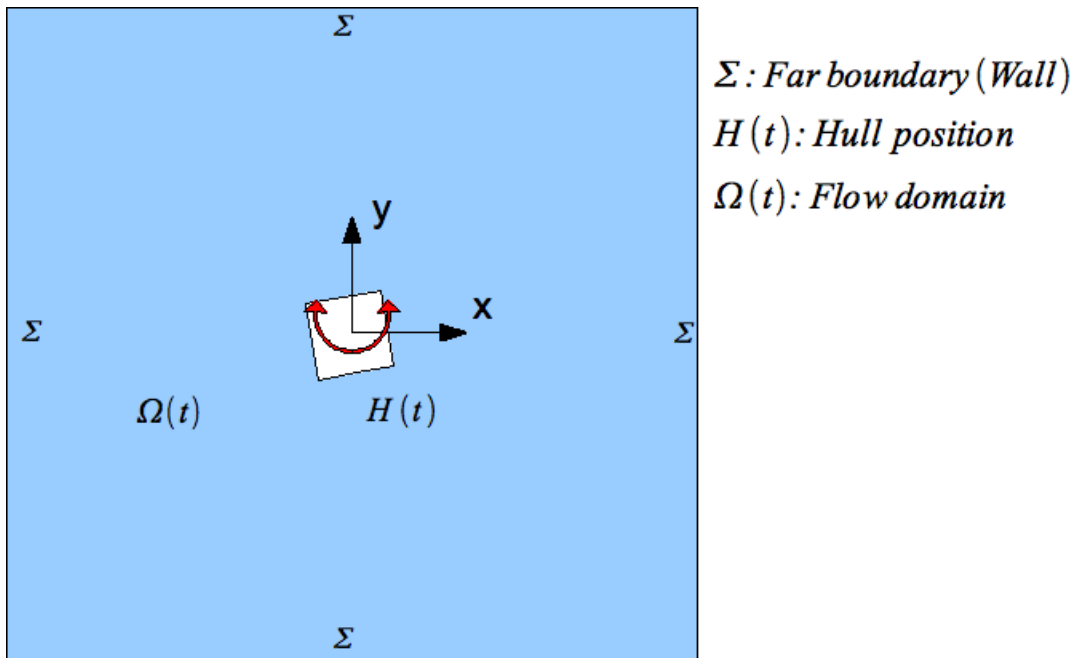


Figure 4.11: Computational domain and corresponding domain boundaries of the submerged hull under prescribed roll motion.

Figure 4.11 shows the computational domain and the corresponding domain boundaries, where the domain is $8B$ long and $8B$ wide. The hull is only allowed to roll about a coordinate system with its origin O , which is the center of the hull in this case.

The forced roll motion starts smoothly with a ramp function R_f (found necessary in order to avoid strong transient flows at the earlier steps of the calculation). The corresponding roll angle α is defined as:

$$\alpha = R_f \alpha_0 \sin(\omega t), \quad (4.5)$$

where ω represents the roll frequency, α stands for the roll angle and α_0 is the amplitude of the roll angle in radians. The ramp function is given as

$$R_f = \begin{cases} \tanh(\omega t) & t / T < 1 \\ 1 & t / T \geq 1 \end{cases} \quad (4.6)$$

The hydrodynamic moment M_ω on the hull is evaluated by integrating the pressure along the body surface:

$$M_\omega = - \int_{H(t)} p \vec{n} \times \vec{r} d\Gamma, \quad (4.7)$$

where \vec{r} represents the distance vector from the center of rotation; and Γ is the hull length.

In order to be consistent with the ship-shaped hull roll motion problem, which is going to be studied in the next chapter, all the variables are made non-dimensional with respect to the hull beam and the prescribed roll period T . Based on Vugts (1968), the angular frequency is made non-dimensional in terms of the hull beam and gravity. The corresponding parameters are defined as:

$$\begin{aligned} \text{Fn} &= \omega \sqrt{\frac{B}{2g}}, \text{ Froude number,} \\ \text{Re} &= \frac{B^2}{\nu T}, \text{ Reynolds number.} \end{aligned} \tag{4.8}$$

The non-dimensional frequency, Froude number Fn , is kept in the range between 0.4 and 1.2. According to Yeung et al (2000) and Yuck (2003), the corresponding Reynolds number used in the NS2D solver ranges from 4.6×10^4 to 1.39×10^5 . Note that in this submerged roll problem, Fn does not directly appear in the governing equations or in the boundary conditions, but it is proportional to Re . As result, the study of different roll frequencies becomes the study of the effects of viscosity.

4.3.2 Mesh Movement

The meshes used in both NS2D and FLUENT are generated using GAMBIT, a grid generator provided by FLUENT Company. One of the issues for simulating the roll motion of the hull is the movement of the cells. One can either re-mesh and smooth those cells close to the hull or define a grid zone interface to separate the moving zone and the stationary zone.

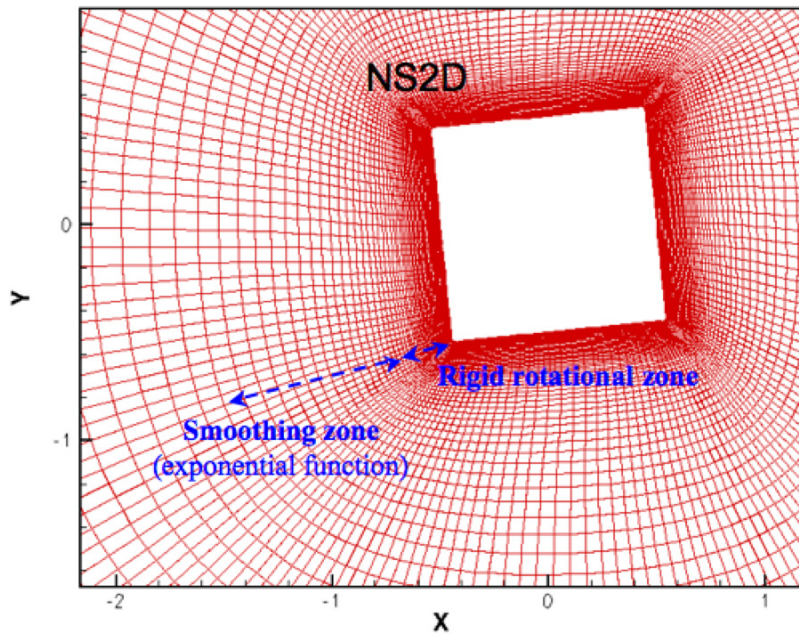


Figure 4.12: Mesh movement of NS2D in the case of a submerged hull.

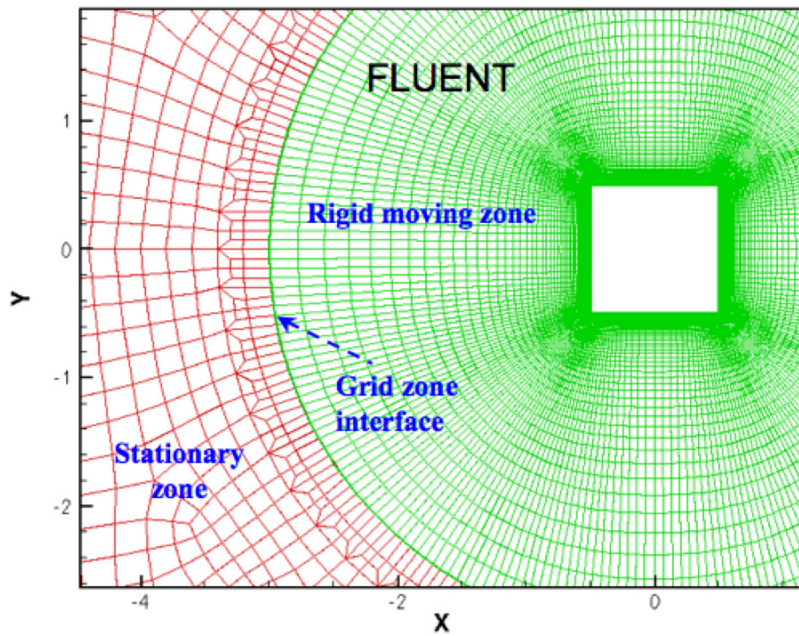


Figure 4.13: Mesh movement of FLUENT in the case of a submerged hull.

In NS2D, the re-mesh and smooth approach is applied as shown in Fig. 4.12, where certain layers of cells from the hull are defined as the rigid rotational zone. From the edge of the rigid rotational zone, certain layers of cells are called the smoothing zone, where an exponential function is given to smooth out the grid rotation. When the dynamic mesh is applied in NS2D, structured and quadrilateral cells are required in the rigid-rotational zone and the smoothing zone. On the other hand, the grid zone interface approach is used in FLUENT, as shown in Fig. 4.13, where the fluid domain is separated into a rigid moving zone and stationary zone by a grid zone interface. The values on the interface are interpolated from the internal cell values on either side of the interface.

4.3.3 Results

The study of a submerged round bilge hull subject to prescribed roll motions is performed in this subsection, where the roll angle amplitude is equal to 5.75 degrees. The simulations are performed using NS2D and FLUENT. In the FLUENT runs, the simulations are conducted with or without the implementation of the turbulent model. Note that the effect of turbulence is only studied by using FLUENT, where FLUENT(L) represents the laminar flow FLUENT solver, and FLUENT(T) indicates the turbulent flow FLUENT solver. The $k-\omega$ turbulent model is implemented in FLUENT(T) with the enhanced wall treatments, and as shown in Fig. 4.14, the corresponding y-plus along the hull surface for the grid applied in FLUENT(T) is smaller than 7.5.

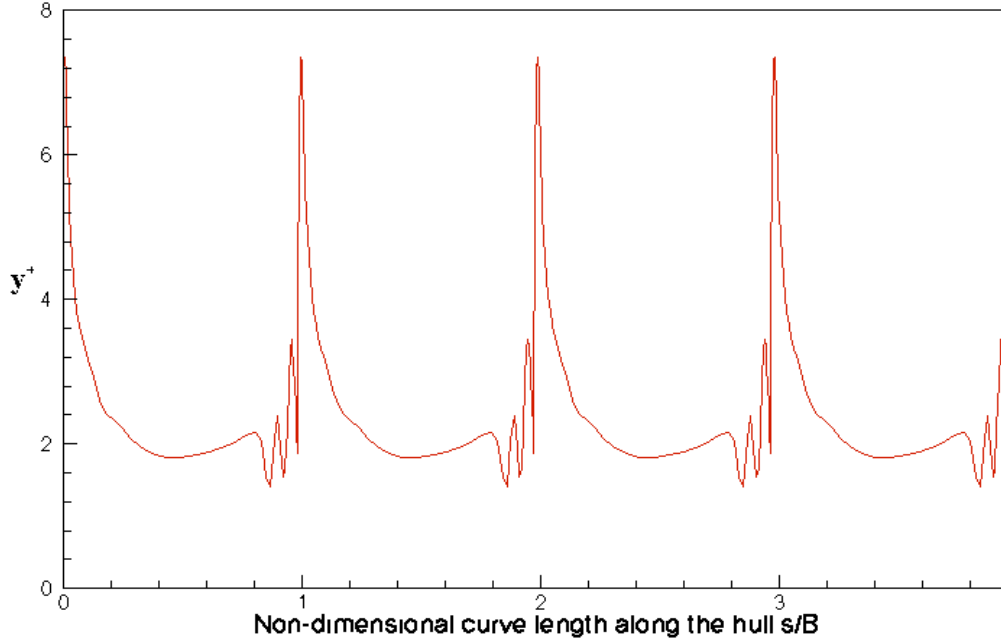


Figure 4.14: y-plus along the round bilge hull in FLUENT(T) simulations ($\alpha_0=5.75^\circ$).

Figure 4.15 shows the moment histories for $F_n=0.4$ predicted from NS2D, FLUENT(L) and FLUENT(T). The vorticity contours at $t/T=4.00$ and $t/T=4.40$ are plotted in Fig. 4.16, where the results from NS2D, FLUENT(L), and FLUENT(T) are shown in the top, mid and bottom figures, respectively. Note that the hull motion is at the maximum angular velocity when $t/T=4.00$, and the roll moment is close to its peak at $t/T=4.40$. Despite the fact that the flow dissipation is slightly higher in the turbulent flow simulation due to the presence of turbulent viscosity, the simulations from NS2D, FLUENT(L) and FLUENT(T) show a very similar flow pattern. The corresponding pressure distributions on the hull surface from NS2D, FLUENT(L) and FLUENT(T) are presented in Fig. 4.17, and the prediction of the pressure distributions from these three solvers also shows a fairly good agreement. As a result, all the moment histories predicted by using NS2D, FLUENT(L) and FLUENT(T) are almost identical to each

other, and the turbulent flow effect is found to be very small in this case. More studies on the effect of turbulence with the presence of the free surface and with different hull geometries will be presented in the next chapter.

Note that NS2D and FLUENT simulations are performed using a 16 nodes workstation with dual AMD Opteron 1.6 Hz processors, and 2GB memory per node. The computational time for a NS2D run is about 1.5 hr / per period by using a single CPU. On the other hand, the FLUENT run requires 1.25 hr to simulate a period of roll motion by using parallel computing with 4 CPUs. The difference on the numerical settings between the two solvers and more studies on the prescribed roll motion of ship-shaped hulls are presented in the next chapter.

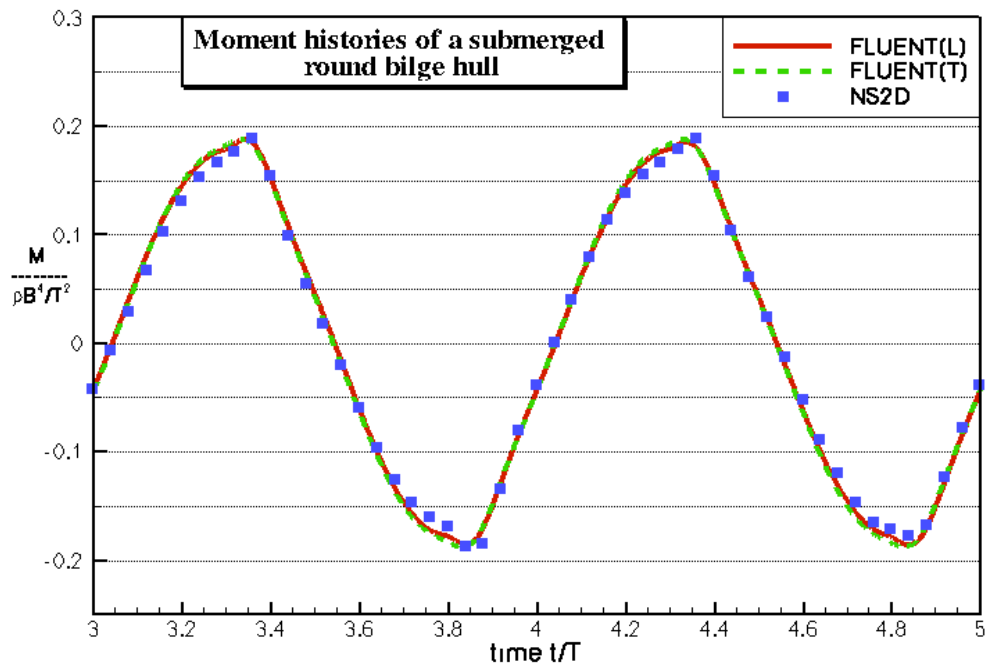


Figure 4.15: Moment histories of submerged round bilge hulls for $F_n=0.4$ and $\alpha_0=5.75^\circ$ from NS2D, FLUENT(L), and FLUENT(T).

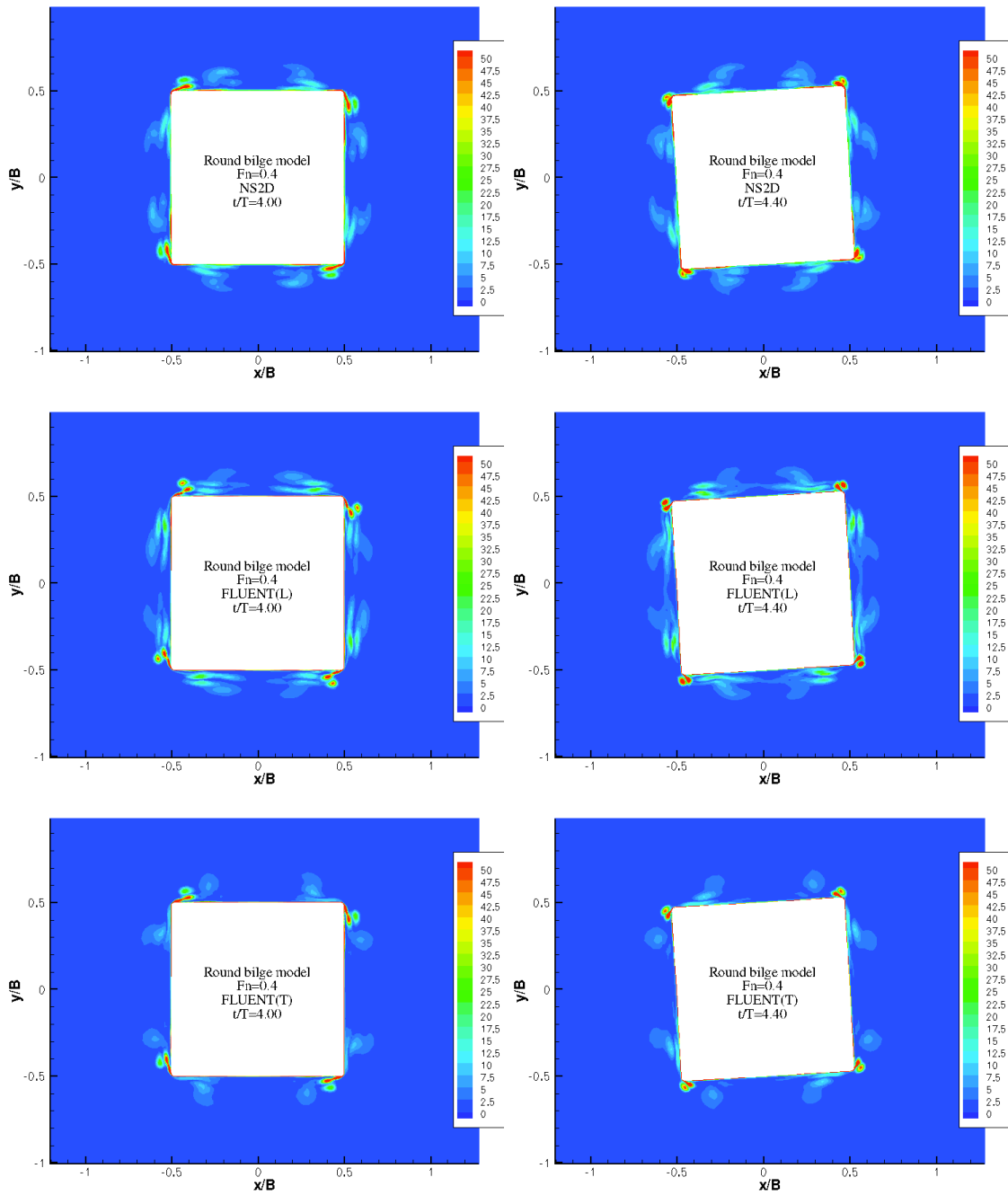


Figure 4.16: Vorticity magnitude contour of the submerged round bilge hull for $Fn=0.4$ and $\alpha_0=5.75^\circ$ from (top) NS2D, (mid) FLUENT(L), and (bottom) FLUENT(T) at $t/T=4.00$ and $t/T=4.40$.

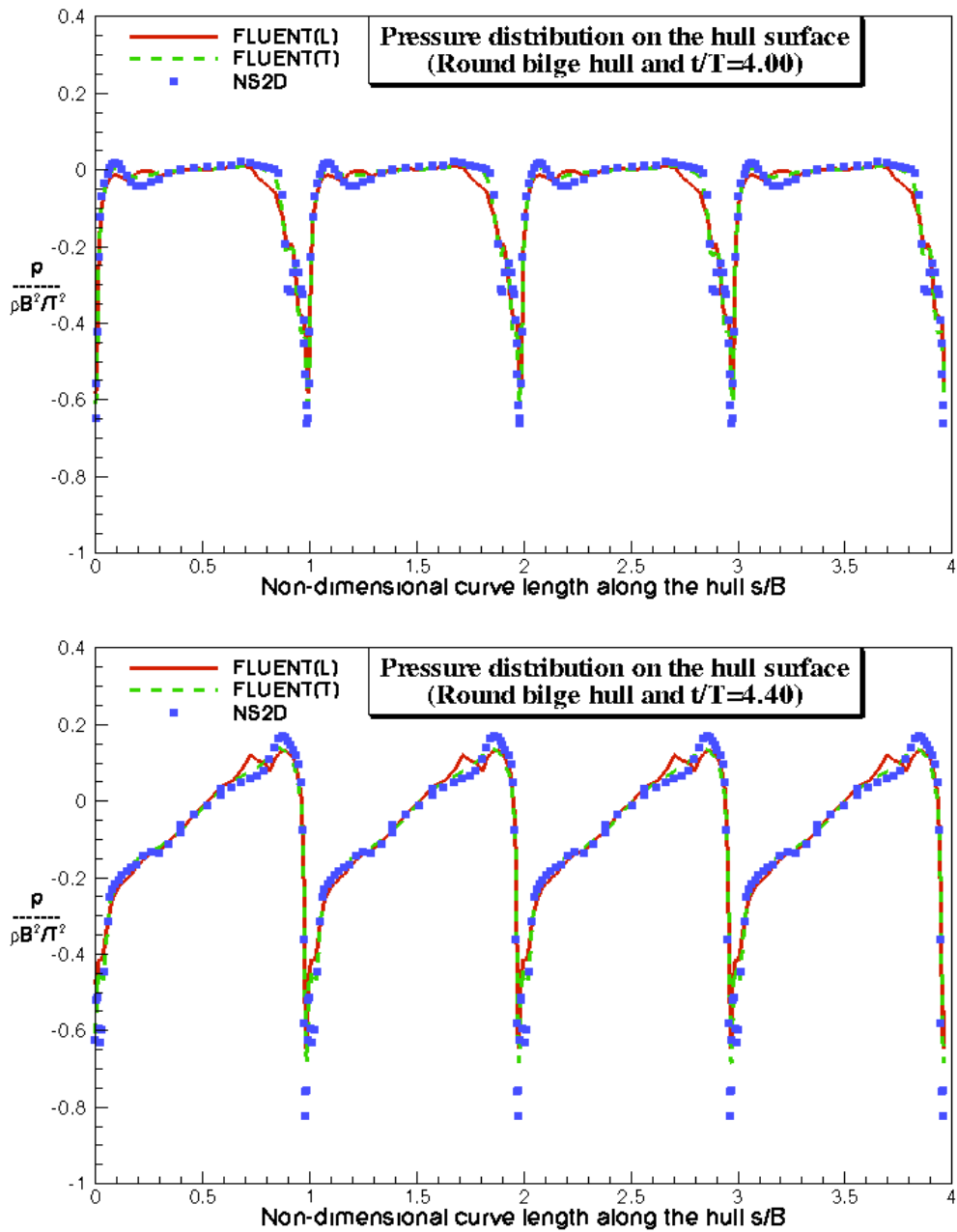


Figure 4.17: Pressure distributions on the submerged round bilge hull from NS2D, FLUENT(L) and FLUENT(T) at $t/T=4.00$ and $t/T=4.40$ ($Fn=0.4$ and $\alpha_0=5.75^\circ$).

4.4 PISTON TYPE WAVE-MAKER

In order to investigate and validate the non-linear boundary conditions on the free surface, the inviscid version of the Navier-Stokes solver, NS2D (IN), is applied to a piston type wave-maker problem. The free-surface wave profile from the NS2D simulation is compared to another numerical result predicted by Lin (1984), who used a potential flow solver, and no linearization assumption was made on the free-surface boundary conditions.

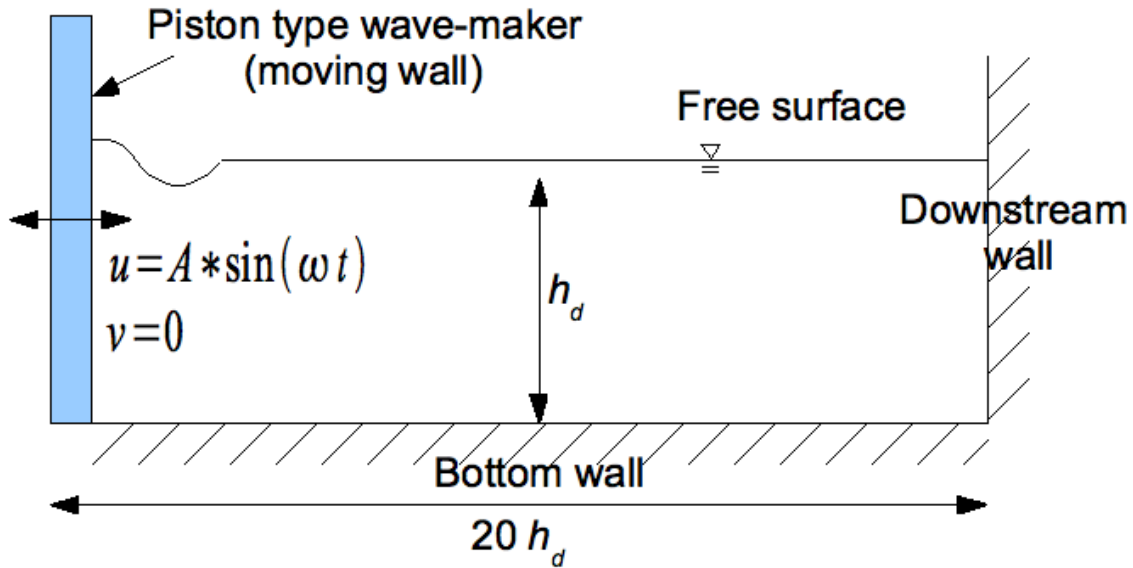


Figure. 4.18: Computational domain and corresponding domain boundaries of a 2D piston type wave-maker problem.

In this validation case, the viscous terms in the momentum equations are excluded in NS2D(IN), and all the variables are made non-dimensional in terms of water depth h_d and characteristic velocity $\sqrt{gh_d}$. The piston wave-maker moves periodically with a frequency of $(\pi/2)\sqrt{g/h_d}$, an amplitude of $A=0.05h_d$, and a time step size of $\Delta t / \sqrt{h_d/g} = 0.1$. The computational domain and corresponding domain boundaries are

presented in Fig. 4.18, where the computational domain is about 20 water-depths long, approximately equal to 8 wavelengths. As shown in Fig. 4.19, the wave elevation predicted from NS2D(IN) shows decent agreement with the numerical solution from Lin (1984). The prediction of the non-linear free-surface elevation is also well validated in this case.

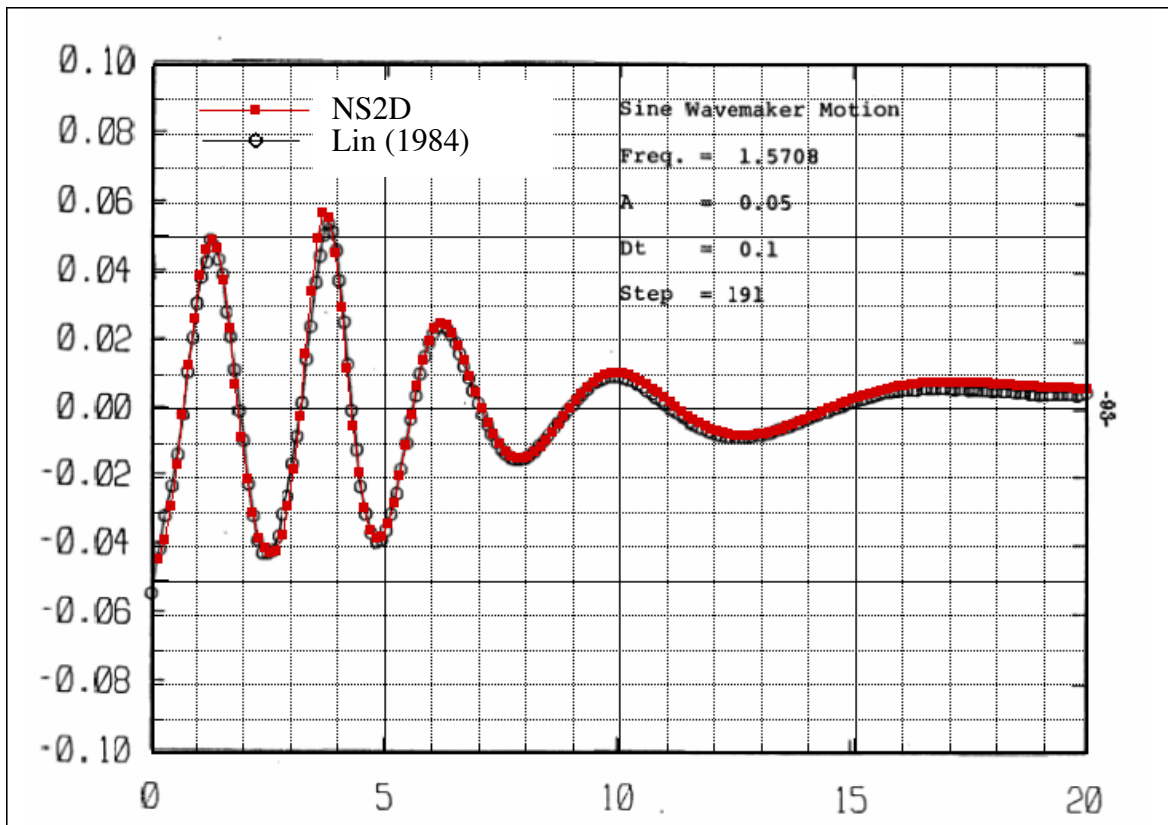


Figure 4.19: The wave elevation of a piston type wave maker at $t/\sqrt{h/g} = 19.10$.

4.5 SUMMARY

A two-dimensional unsteady Navier-Stokes solver has been verified and validated in several different test cases, a vertical plate subject to an alternating inflow, a fixed submerged hull subject to oscillating inflow, prescribed roll of a submerged hull and the wave-maker problem. The results predicted from NS2D show a fairly good agreement with those from other numerical methods in all cases. In the next chapter, NS2D will be applied to the ship-shaped hull motion problem, where the effect of free surface is included.

Chapter 5: Two-Dimensional Ship-Shaped Hull

In this Chapter, the NS2D solver is applied to a ship-shaped hull motion problem, where the free surface is present. Two types of simulations are presented in this chapter. In the first type of simulation, ship-shaped hulls are subject to prescribed roll motions. The second type of simulation studies the free-decay motions for hulls with a given initial heave or roll displacement.

5.1 PRESCRIBED ROLL MOTION

The background of the prescribed ship-shaped hull roll motion simulations is described in this section. Also presented are the studies on the sensitivity analyses in space and in time, the correlation between the present numerical scheme and other methods, the investigation of the free-surface effect, and the studies of different hull geometries and roll angles.

5.1.1 Background

Certain assumptions are made to simplify the complex nature of the forced roll motion. The hull is assumed to roll about a coordinate system with its origin O at the intersection of the mean free surface and the longitudinal axis of the hull. The beam over draft ratio B/D is equal to 2, and the center of gravity is situated at O . The orientations of the boundaries and the computational domain are shown in Fig. 5.1, where $S_F(t)$ and $S_H(t)$ represent the instantaneous positions of the free-surface and the hull surface respectively.

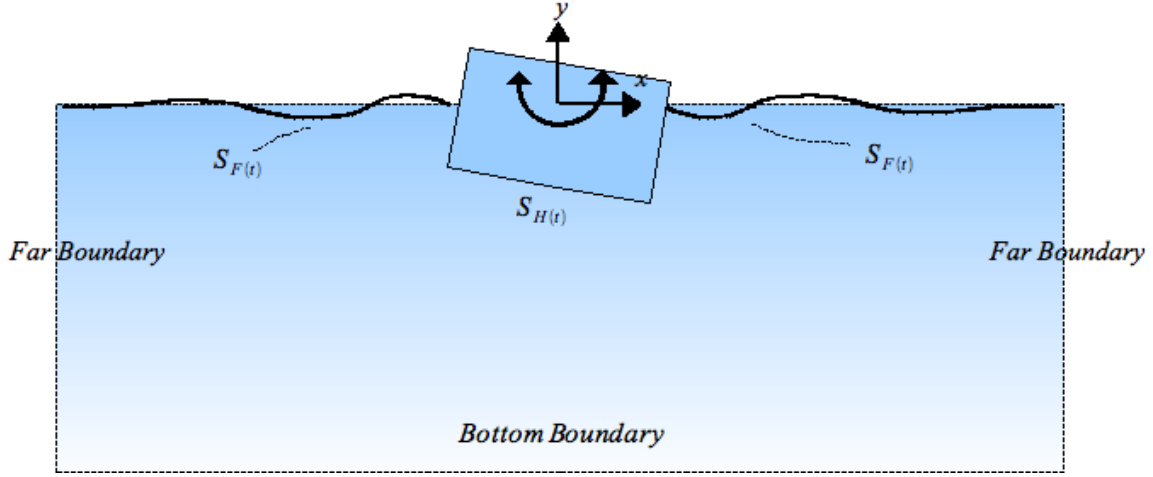


Figure 5.1: Computational domain and corresponding domain boundaries of the FPSO hull forced roll motion problem.

The ship-shaped hull is forced to rotate periodically following exactly the same roll motion as used in the submerged hull roll motion problem. The corresponding total force vector \vec{F}_o and total moment M_o on the hull are evaluated by integrating the pressure on the wetted portion of the body surface.

$$\vec{F}_o = - \int_{H(t)} (p - \rho gy) \vec{n} d\Gamma, \quad M_o = - \int_{H(t)} (p - \rho gy) \vec{n} \times \vec{r} d\Gamma, \quad (5.1)$$

where \vec{r} represents the distance vector from the center of rotation and Γ stands for the hull length. Note that in order to be consistent with the results from the experiments by Vugts (1968), Yeung et al. (1998) and Yeung et al. (2000), and the FLUENT calculations, the hydrostatic pressure term is included in Eq. (5.1).

Following Yeung et al. (2000) and Wilson (2006), the hydrodynamic moment M_ω is obtained from the total moment by subtracting the hydrostatic restoring term M_r , which is given as:

$$\begin{aligned} M_\omega &= M_o - M_r, \\ M_r &= \rho g \nabla B \sin(\alpha) / 12, \end{aligned} \quad (5.2)$$

where $\nabla = B^2/2$ denotes the 2D hull displacement. Based on the linear theory, the hydrodynamic moment can be written as a combination of the added-mass a_{66} and damping b_{66} terms:

$$M_\omega = -a_{66} \ddot{\alpha} - b_{66} \dot{\alpha}, \quad (5.3)$$

where $\ddot{\alpha}$ stands for the angular acceleration. The added-mass and damping coefficients can be extracted from the roll moment history using Fourier analysis (averaged from last three periods), which are given as:

$$\begin{aligned} a_{66} &= \frac{1}{\pi \alpha_o \omega} \int_0^T M_\omega \sin(\omega t) dt, \\ b_{66} &= \frac{-1}{\pi \alpha_o} \int_0^T M_\omega \cos(\omega t) dt. \end{aligned} \quad (5.4)$$

For consistency and comparison purposes, the hydrodynamic coefficients are normalized following Vugts (1968) and Yeung et al. (2000),

$$a_{66}^* = \frac{a_{66}}{\rho \nabla B^2}, \quad b_{66}^* = \frac{b_{66}}{\rho \nabla B^2} \sqrt{\frac{B}{2g}}. \quad (5.5)$$

In NS2D, the non-dimensionalization parameters applied in the prescribed roll motion problem are exactly the same as those used in the submerged hull case. According to Yeung et al (2000) and Yuck (2003), the hull beam used in the experiment is equal to $0.3048m$, and the non-dimensional frequency F_n varies from 0.4 to 1.2. The corresponding Reynolds number and the non-dimensional gravity used in the NS2D solver are illustrated in Table 5.1.

$F_n = \omega \sqrt{B / 2g}$	$T(sec)$	$g^* = g / (B / T^2)$	$Re = B^2 / \nu T$
0.4	1.942	123.370	46,335
0.6	1.295	54.831	69,503
0.8	0.971	30.843	92,670
1.0	0.777	19.739	115,838
1.2	0.647	13.708	139,006

Table 5.1: The non-dimensional parameters for various roll frequencies used in NS2D.

As shown in Fig. 5.2, for both NS2D and FLUENT runs, the mesh movement approaches applied in the ship-shaped hull roll motion problem are similar to those used in the submerged hull cases. In NS2D, when the free surface is present, the grids close to the free surface also need to be re-meshed and smoothed. On the other hand, as shown in Fig. 5.3, FLUENT still uses the grid interface approach, as described in the submerged

roll case, even though it requires higher grid resolution in the area close to the free surface.

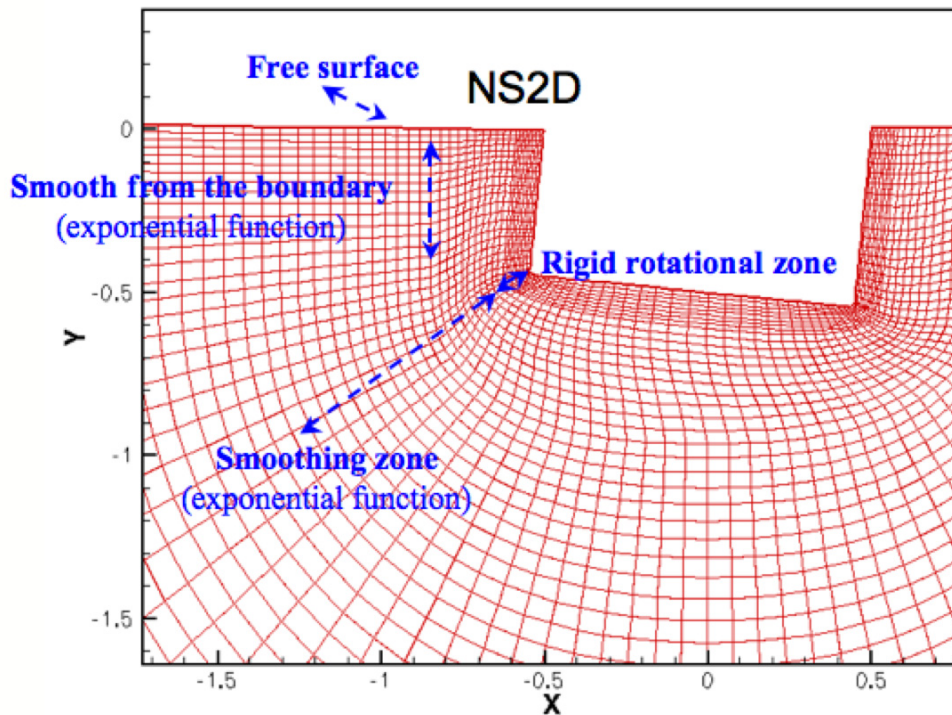


Figure 5.2: Mesh movement of NS2D in the case of a ship-shaped hull.

Using the re-mesh and smooth algorithm is simple to apply in coding, but one has to make sure that the cell volume does not become negative (cell is not over-twisted) while simulating the roll motion of hulls, particularly in the case when the free surface is present. On the other hand, using the grid zone interface approach has the advantage of keeping the cell volume the same for the entire time domain, which avoids cell-deforming issue. However, with the presence of the free surface (two-fluid interface), the numerical simulation is very sensitive to the grid resolution close to the free surface, particularly at the intersection of the grid zone interface and the free surface. Fig. 5.3

shows a good example. When the rigid moving zone is subject to a large roll angle, the grid resolution at the intersection of the grid zone interface and the free surface is not sufficient. As a result, an artificial wave reflection may occur at the grid zone interface.

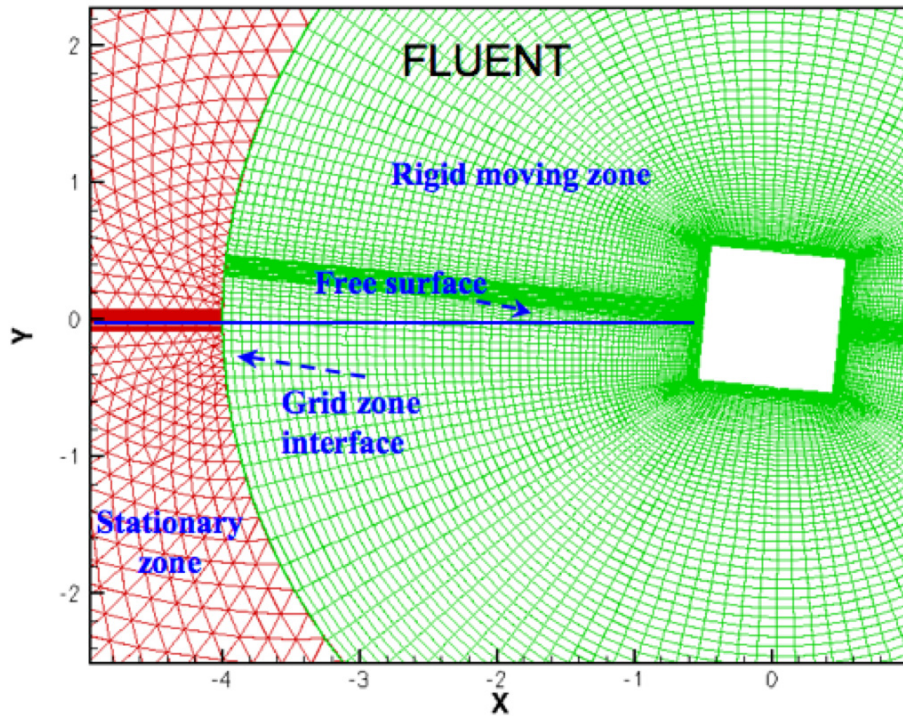


Figure 5.3: Mesh movement of FLUENT in the case of a ship-shaped hull.

Both NS2D and the commercial solver, FLUENT, are based on FVM, but these two solvers apply different algorithms for the boundary conditions and have different numerical settings. In addition to the difference on the grid movement, NS2D uses the free-surface tracking algorithm, but FLUENT applies the Volume Of Fluid (VOF) method to predict the free surface. These differences are listed in Table 5.2. Note that the FLUENT version used in this study is 6.3.26 (version up-to-date), and the settings can be

different from another FLUENT version. In this version, the time marching scheme becomes 1st-order accurate in time when the dynamic mesh is implemented. Therefore, instead of using 200 time steps per period of roll in NS2D, FLUENT is set to run with 1000 time steps per period. Moreover, the $\partial p / \partial n = 0$ boundary condition on the wall in FLUENT will require a higher grid resolution to preserve the accuracy for predicting the corresponding forces and the moment. It becomes essential when the hull moves and/or when the free surface is present, where the hydrostatic pressure is proportional to the water depth. It also makes FLUENT jobs require much more computational power. Even with the ability to parallelize the job with several CPUs, it will be very difficult for FLUENT to run a fully 3D case with a sufficient grid resolution. More details of the 3D simulation using present numerical scheme will be discussed in Chapter 6.

	NS2D	FLUENT
Free surface prediction	Free-surface tracking algorithm	VOF
Time accuracy	2 nd -order ($\Delta t/T=0.005$)	1 st -order ($\Delta t/T=0.001$)
Pressure boundary condition on the wall	Linear extrapolation	$\partial p / \partial n = 0$ (FLUENT user manual)
Computational time	For N \approx 10,000 2hrs/period; single CPU	For N \approx 62,000 (22,000 in air; 40,000 in water) 6hrs/period; 8 CPUs

Table 5.2: Differences between NS2D and FLUENT⁵.

⁵ The NS2D and FLUENT simulations are performed using a 16 nodes workstation with dual AMD Opteron 1.6 Hz CPUs, and 2GB memory per node.

5.1.2 Hull Geometries

The four different hull geometries used in the following studies are shown in Fig. 5.4. B represents the hull beam, and the beam/draft ratio is equal to 2. The box model is considered as a reference shape. The round bilge model has the same bilge radius, $0.02B$, as the one used in Yeung et al. (1998). The bilge keel model is defined following (Yeung et al. 2000). The one with a keel length of $0.04B$ is used in the following studies, and it will be named 4% bilge keel model hereafter, unless mentioned otherwise. The last model is the "step model", whose geometry is the same as defined in Yuck et al. (2003).

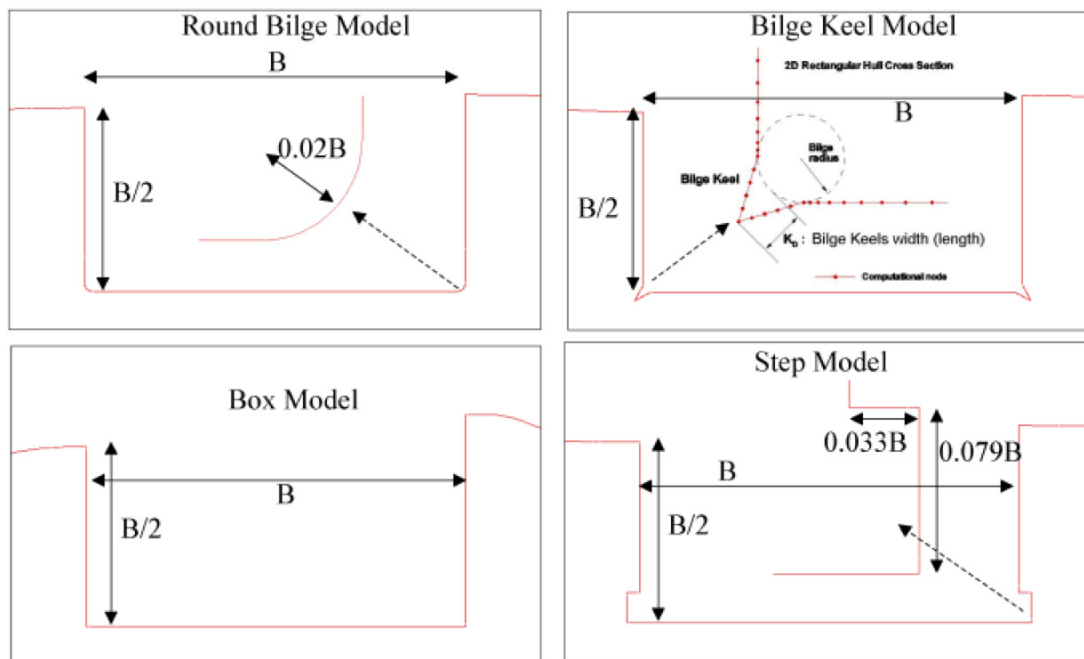


Figure 5.4: Four shapes of the hull: (1) Round bilge model; (2) Bilge keel model; (3) Box model; (4) Step model.

5.1.3 Sensitivity Analyses

To validate the numerical results obtained from a ship-shaped hull undergoing a forced harmonic roll motion, the sensitivities of the grid resolution and the time step size are studied. The studies are performed using the round-bilge hull with a fixed roll angle amplitude of $\alpha_0=5.75^\circ$.

For the grid resolution analysis, the moment history from the highest resolution is used as the "exact" solution. The absolute error difference ε_m between the "exact" solution and the moment history from another grid resolution is obtained using the least square method:

$$\varepsilon_m = \frac{1}{N_T} \sqrt{\sum_{i=1}^{N_T} (M_c - M_e)_i^2}, \quad (5.6)$$

where N_T is the number of time steps for the last two periods, M_e indicates the "exact" moment history, M_c is the moment history from a coarser grid and the subscript "i" represents the data index at each time step.

The definition of the boundary layer cell height δ is explained in Fig. 5.5. Four different heights, $\delta=0.002B$, $0.005B$, $0.01B$, and $0.02B$, are used for the grid sensitivity analysis. The convergence rate for three different roll frequencies, $\text{Fn}=0.4$, 0.8 and 1.2 , are presented in Fig. 5.6. Note that due to the stability constraint on the time step size for the free surface calculation, the time step size in the case of $\text{Fn}=0.4$ is equal to $\Delta t/T=0.002$, and $\Delta t/T=0.005$ is used in the cases of $\text{Fn}=0.8$ and $\text{Fn}=1.2$. The convergence rate is obtained using Eq. (5.6), and the result of $\delta=0.002B$ is used as the "exact" solution. The moment histories for different boundary-layer-cell heights are shown in Fig. 5.7, where the roll frequency fixed at $\text{Fn}=0.8$ and a roll angle amplitude is given as $\alpha_0=5.75^\circ$.

The differences between the "exact" solution and the results from the coarser grids at every quarter period are relatively small as compared to the difference in the moment amplitude. The results suggest that the grid resolution may not have a significant impact on the hydrodynamic coefficients. However, the roll moment amplitude can be underestimated using a low-resolution mesh. According to the studies, a grid size of $\delta=0.005B$ is adequate and, therefore, will be used in subsequent studies. The same boundary layer cell height is also applied in the studies with different hull models. Only the number of the cells along the hull corner will be different due to the various hull corner geometries.

The sensitivity of the resolution in time is analyzed with three different time step sizes, $\Delta t/T=0.001$, 0.002 , and 0.005 . The corresponding moment histories and the blowup view are plotted in Fig. 5.8. Note that due to the stability issue for calculating the free-surface elevation, no time step size larger than $0.005T$ can be implemented. The results have shown that the differences among all three cases are found to be extremely small. Therefore, $\Delta t/T=0.005$ is proved to be adequate and will be used in the following studies, except for $Fn=0.4$ and $Fn=0.6$ cases, where $\Delta t/T=0.002$ will be used due to the same free-surface stability constraints.

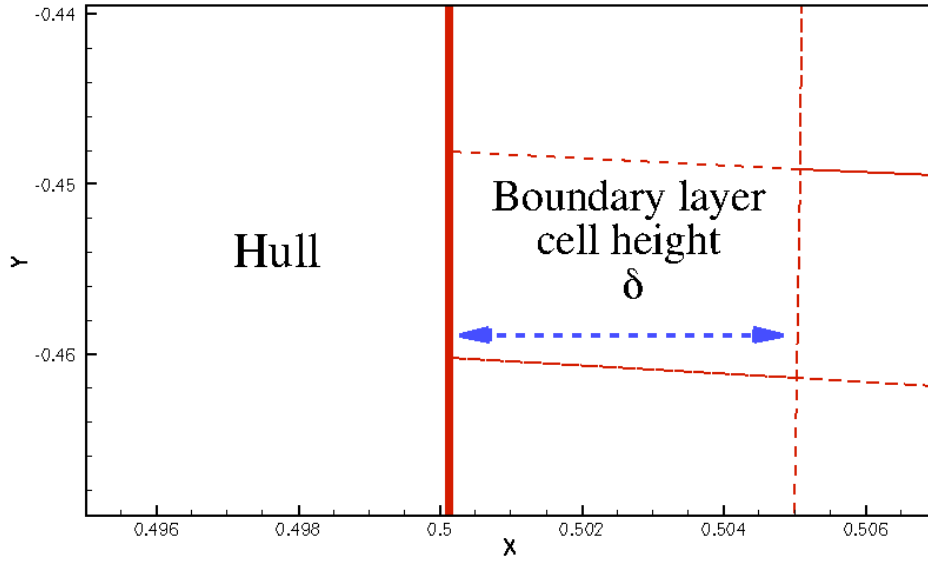


Figure 5.5: The definition of the boundary-layer cell height.

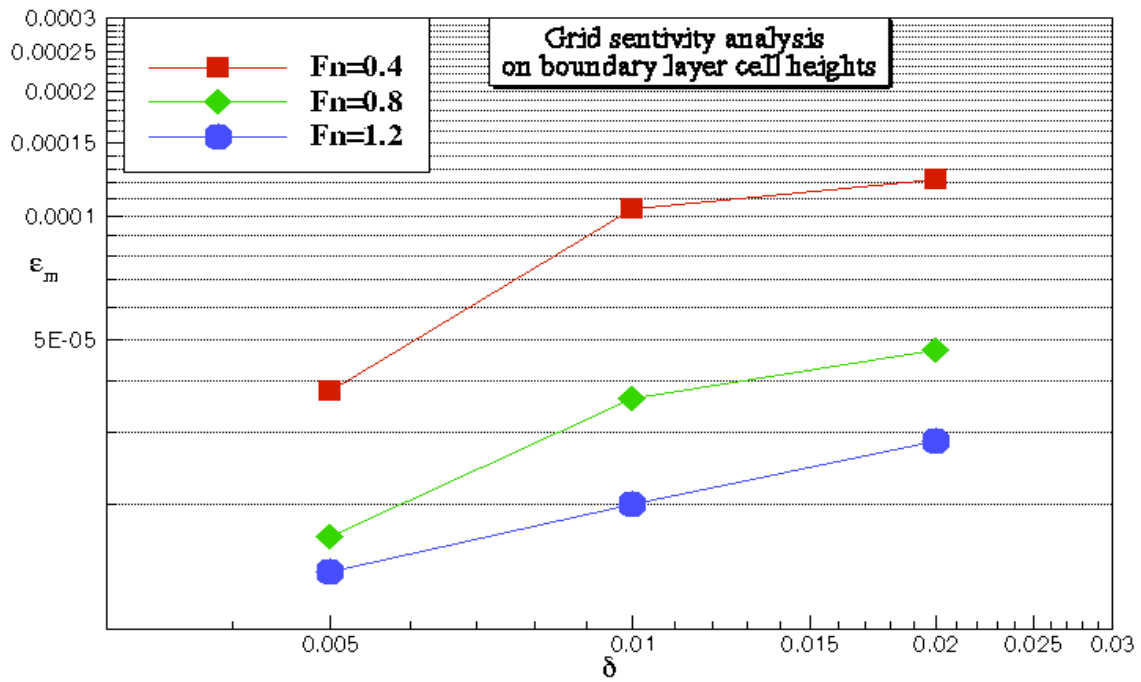


Figure 5.6: Logarithmic plot of the absolute errors between the "exact" solution and the results from coarser grid resolutions (round bilge hull, $\alpha_0=5.75^\circ$ and $Fn=0.4, 0.8$ and 1.2).

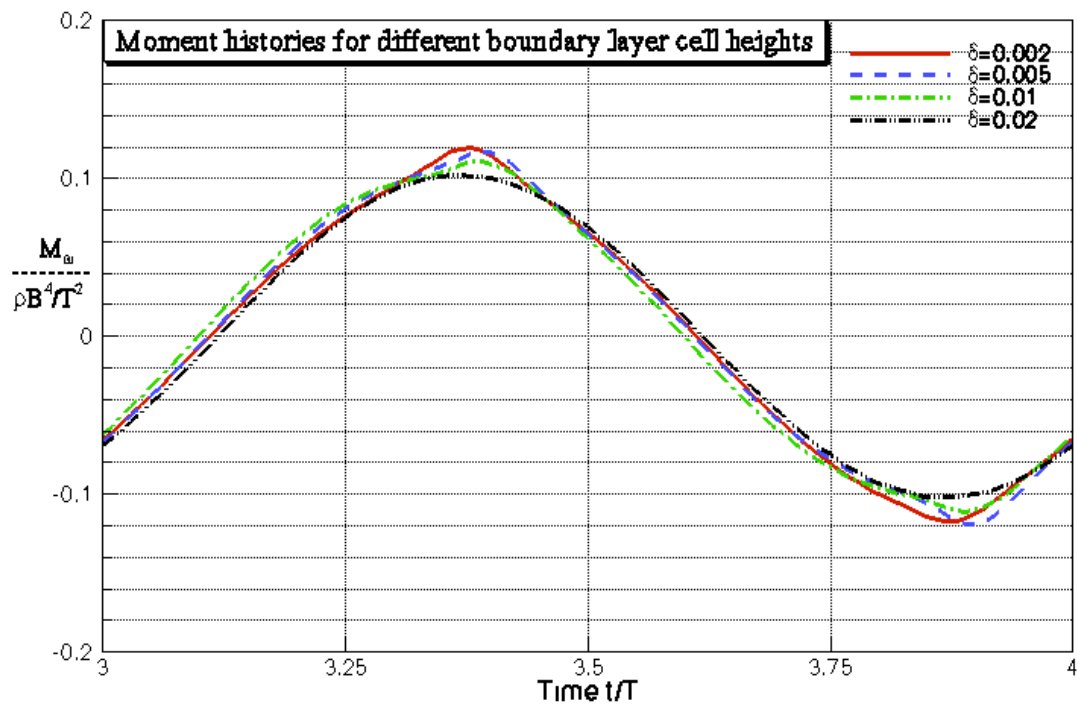


Figure 5.7: Comparison of the moment histories for different boundary layer cell heights and its blowup view (round bilge hull, $\alpha_0=5.75^\circ$ and $Fn=0.8$).

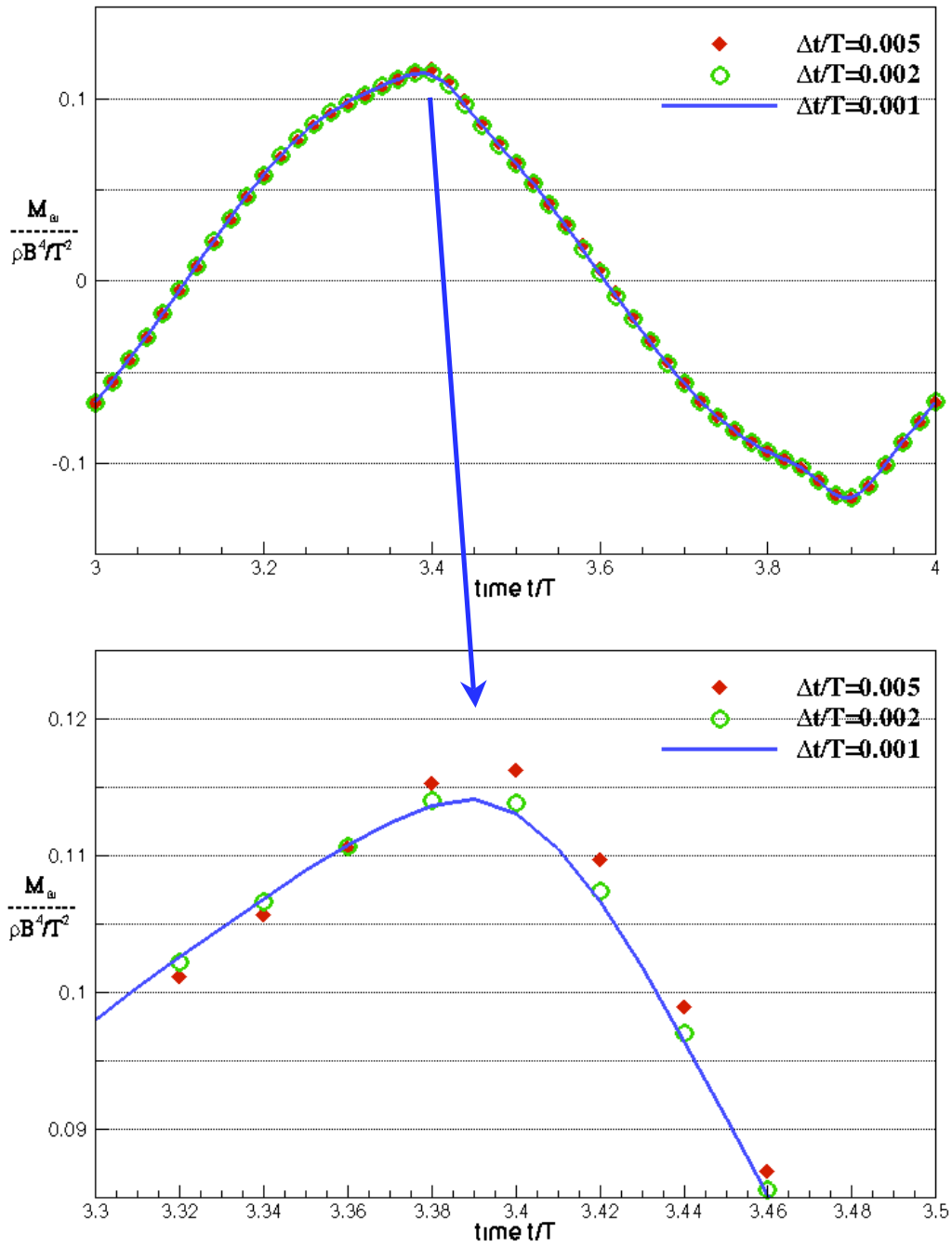


Figure 5.8: Comparison of the moment histories for different time step sizes and its blowup view (round bilge hull, $\alpha_0=5.75^\circ$ and $Fn=0.8$).

5.1.4 Correlation with Other Methods

This subsection presents the comparison of the results from the NS2D solver and other methods for different hull geometries. As mentioned in subsection 5.1.2, four hull geometries are implemented in the studies, which include round bilge model, 4% bilge keel model, box model and step model.

Round Bilge model

In the case of the round bilge model, the results from the NS2D simulation are compared to those solved by using FLUENT or a BEM based potential flow solver (Vinayan et al. 2005) and to other experimental data.

The potential flow solver is primarily used for validation purposes. The reason for comparing inviscid NS2D results to those from the potential flow solver is to validate the prediction of the non-linear free surface in the NS2D simulation. The BEM scheme is categorized into two types based on the applied boundary conditions on the free surface. MBLF represents Moving Body Linear Free-surface, and NL-BEM indicates that a fully non-linear free surface is applied along with the moving hull in the BEM solver. The results are produced at a fixed Froude number, $F_n=1.0$. Two roll amplitudes, $\alpha_0 = 5.75^\circ$ and $\alpha_0 = 11.5^\circ$, are used. Pressure and the velocity components on the hull from NS2D(IN) are compared to those from NL-BEM in Fig. 5.9 to Fig. 5.12. The comparisons of the results from these two solvers show great agreements. To further verify the application of the non-linear free-surface boundary conditions, the wave elevations from NS2D are compared to those from NL-BEM on both starboard and port sides of the hull. As shown in Fig. 5.13, the free-surface elevations from both solvers also agree well, which also proves that the numerical approach used for calculating the non-linear free surface works successfully.

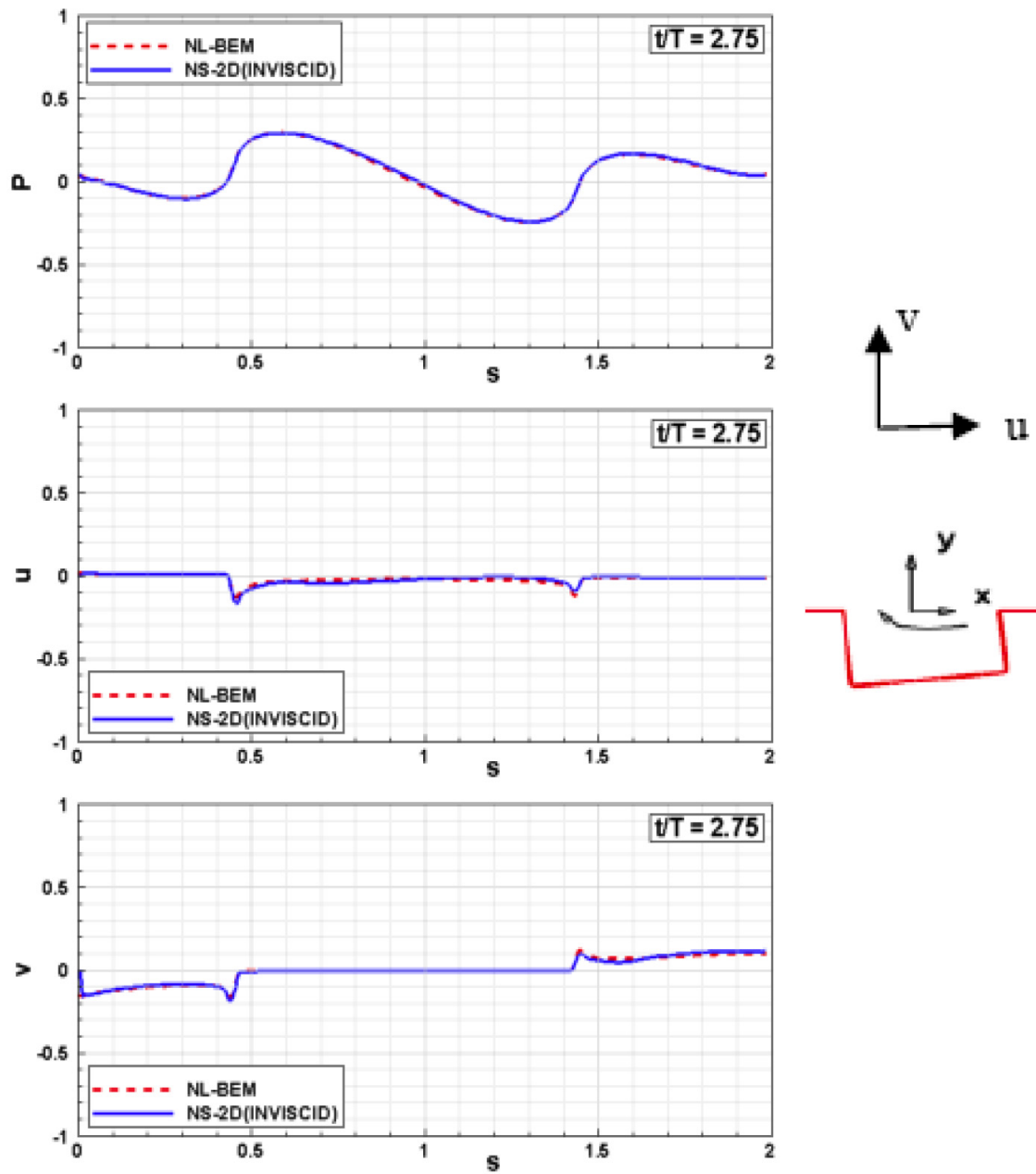


Figure 5.9: Comparison of pressure and velocity components between NS2D(IN) and NL-BEM (Vinayan et al. 2005) (round bilge hull, $\alpha_0=5.75^\circ$, $Fn=1.0$ and $t/T=2.75$).

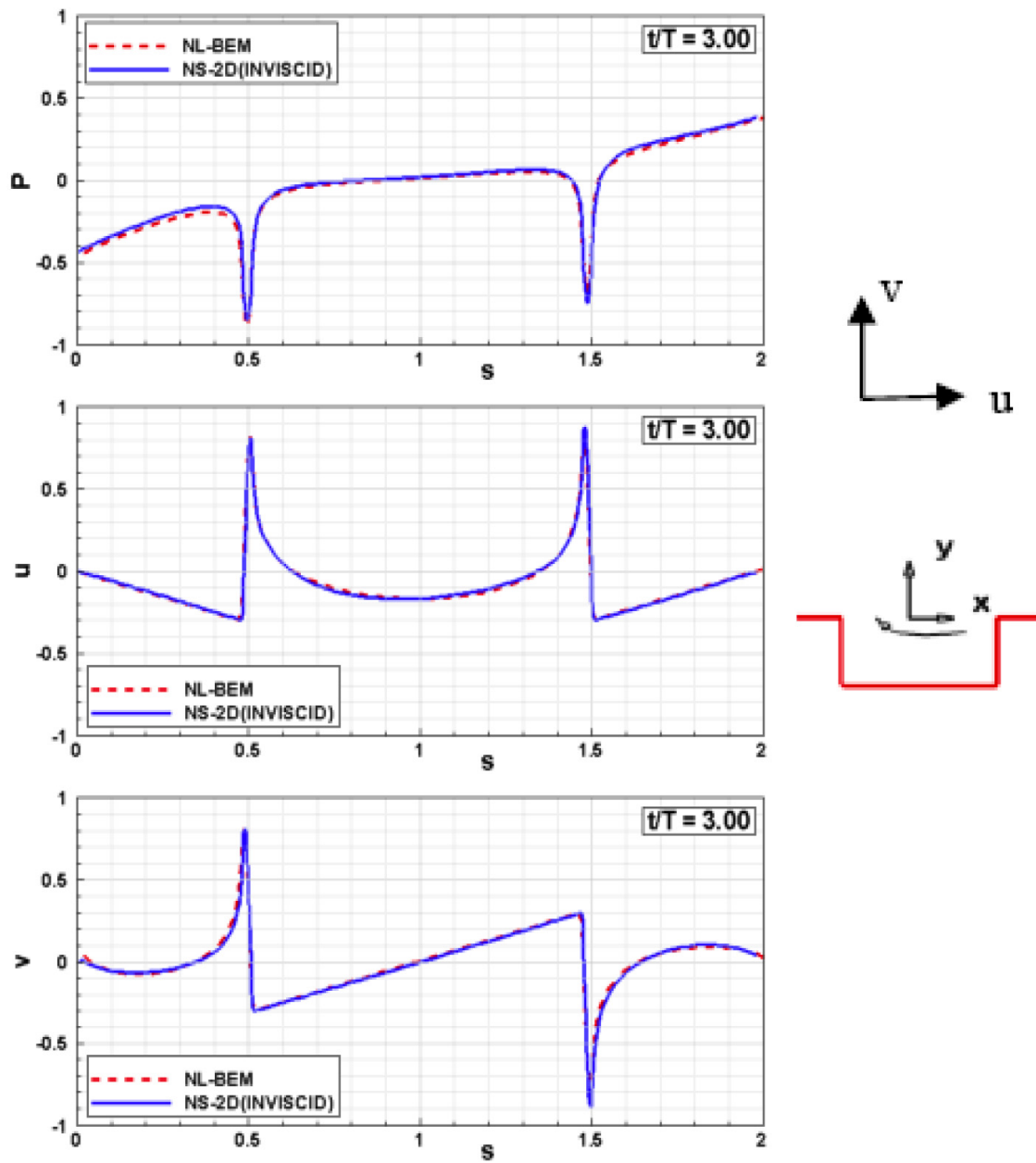


Figure 5.10: Comparison of pressure and velocity components between NS2D(IN) and NL-BEM (Vinayan et al. 2005) (round bilge hull, $\alpha_0=5.75^\circ$, $Fn=1.0$ and $t/T=3.00$).

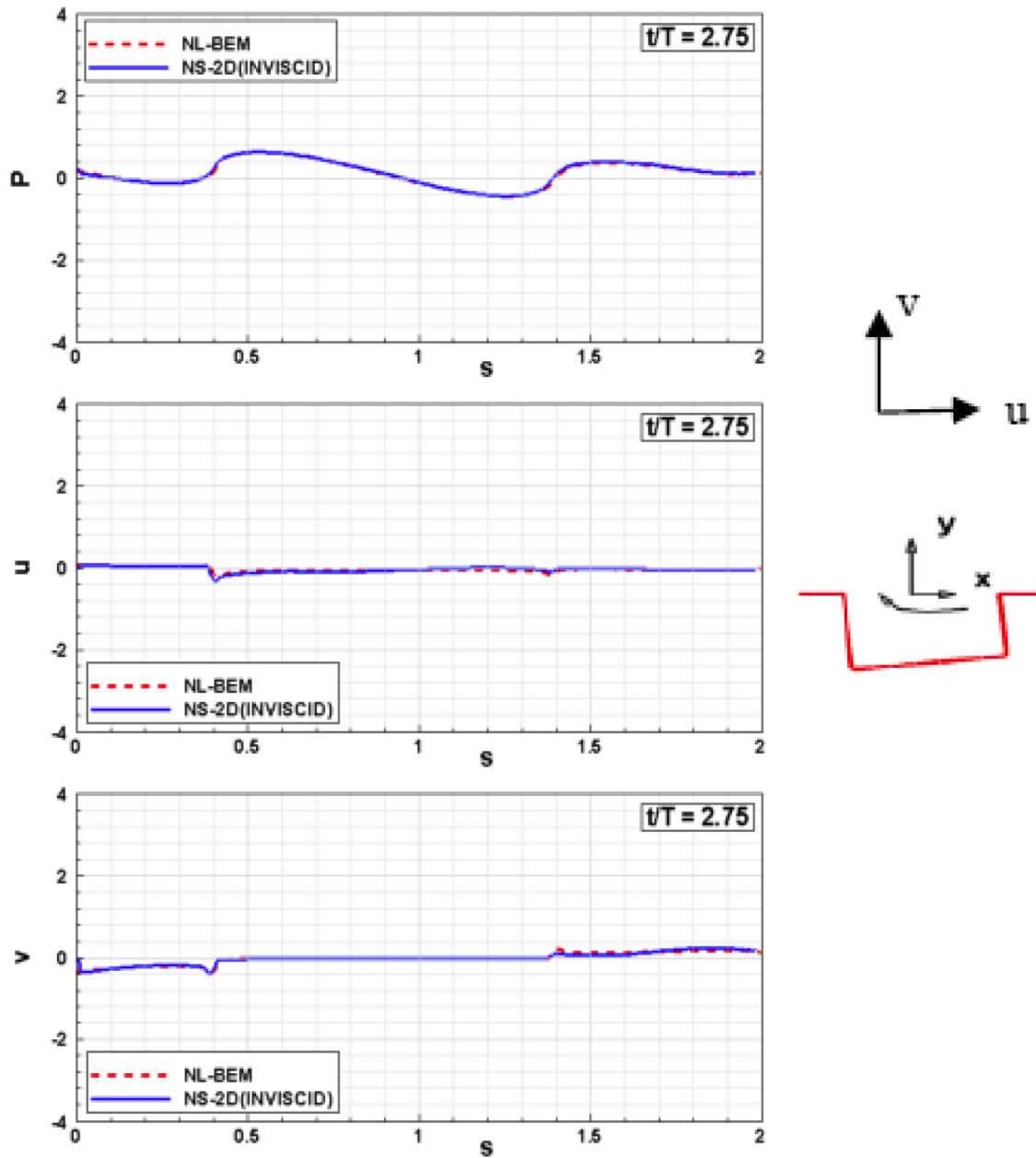


Figure 5.11: Comparison of pressure and velocity components between NS2D(IN) and NL-BEM (Vinayan et al. 2005) (round bilge hull, $\alpha_0=11.5^\circ$, $Fn=1.0$ and $t/T=2.75$).

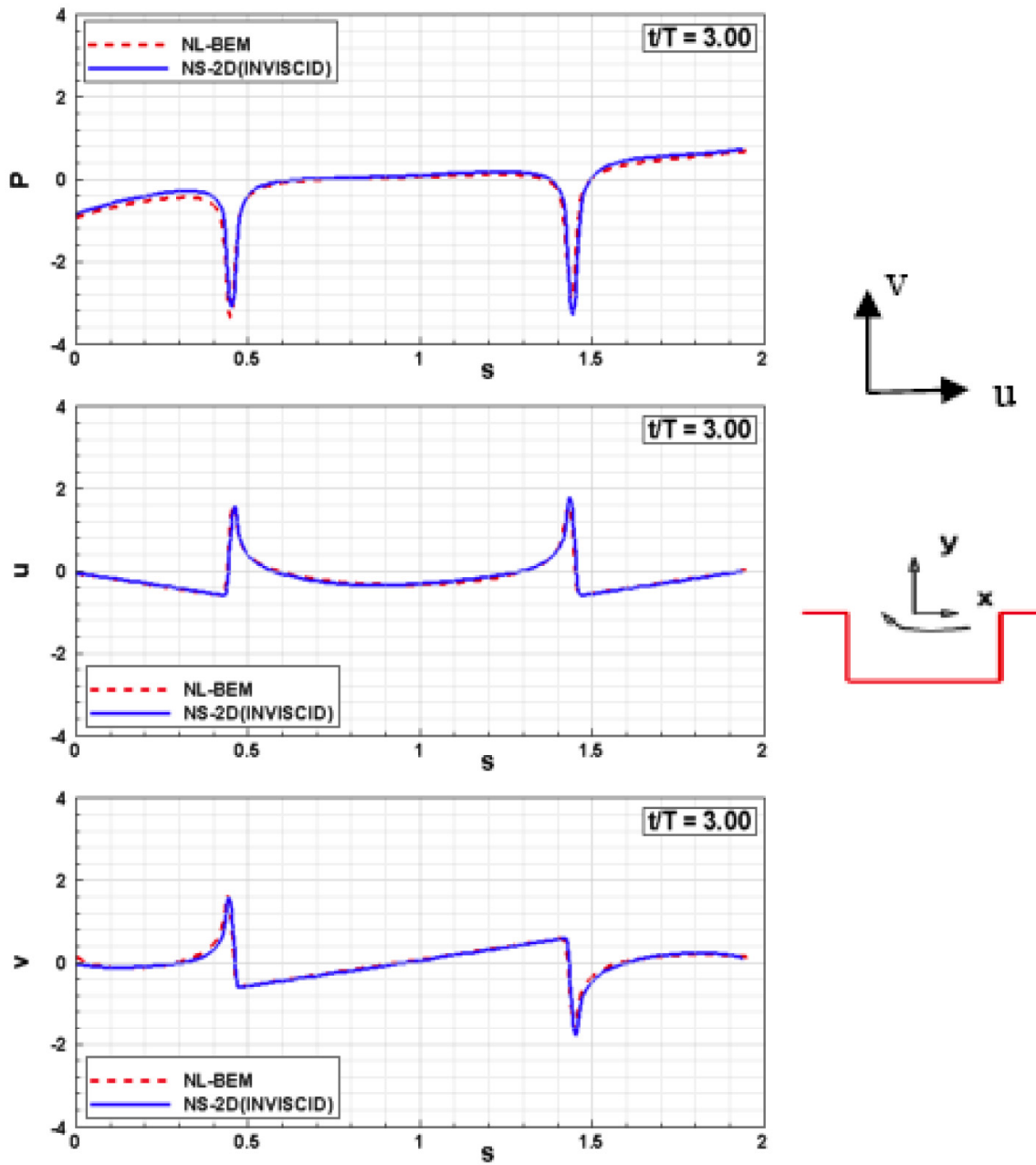


Figure 5.12: Comparison of pressure and velocity components between NS2D(IN) and NL-BEM (Vinayan et al. 2005) (round bilge hull, $\alpha_\theta=11.5^\circ$, $Fn=1.0$ and $t/T=3.00$).

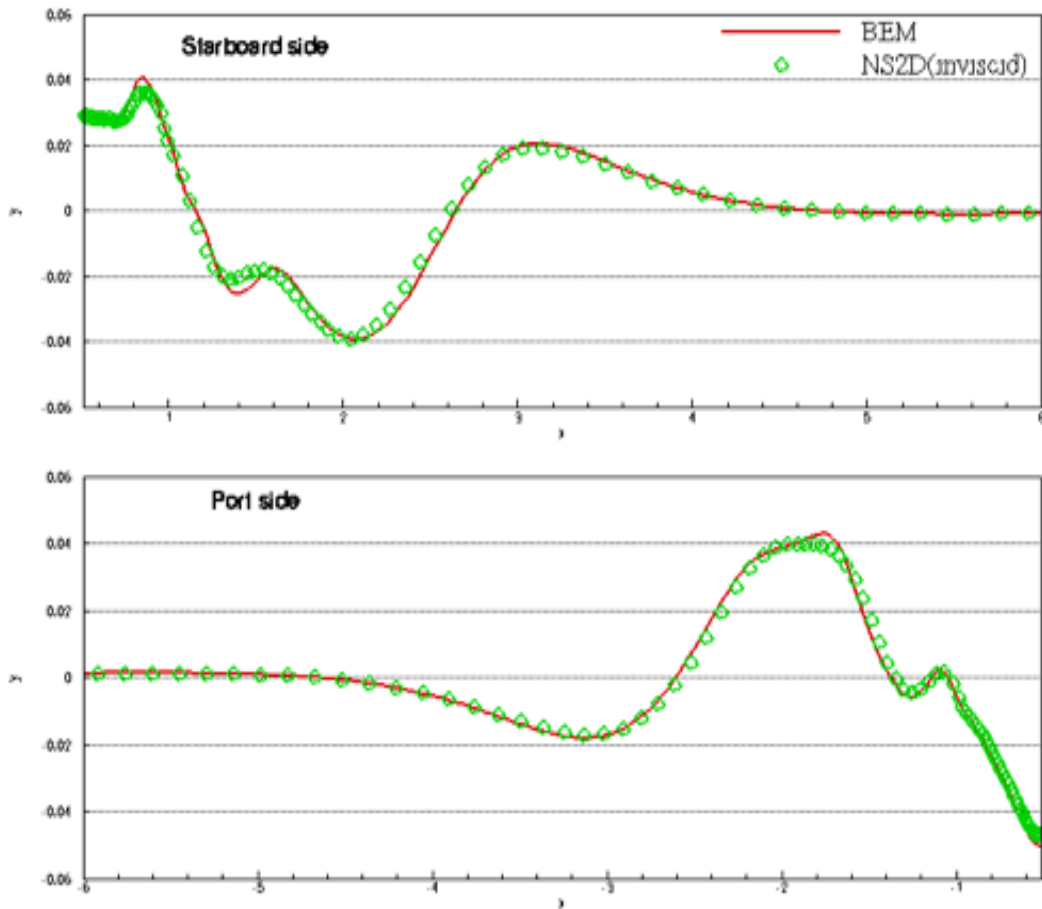


Figure 5.13: Comparison of the moment histories between NS2D and NL-BEM (Vinayan et al. 2005) results (round bilge hull, $\alpha_0=5.75^\circ$, $Fn=1.0$ and $t/T=2.45$).

Figure 5.14 presents the moment histories from NS2D(IN) and the viscous version of the Navier-Stokes solver, NS2D(VS). As expected, the moment history predicted from NS2D(VS) is higher in amplitude and a phase shift is found between the viscous and inviscid results. It is due to the boundary layer effect, where the vorticity is generated, especially near the bilge area (as will be shown in the later section). As shown in Fig. 5.15, those vortices result in a modified pressure distributions on the hull close to the bilge area. All the studies in the following subsections are performed in viscous flow,

where "NS2D" will represent the viscous version of the present method, unless mentioned otherwise.

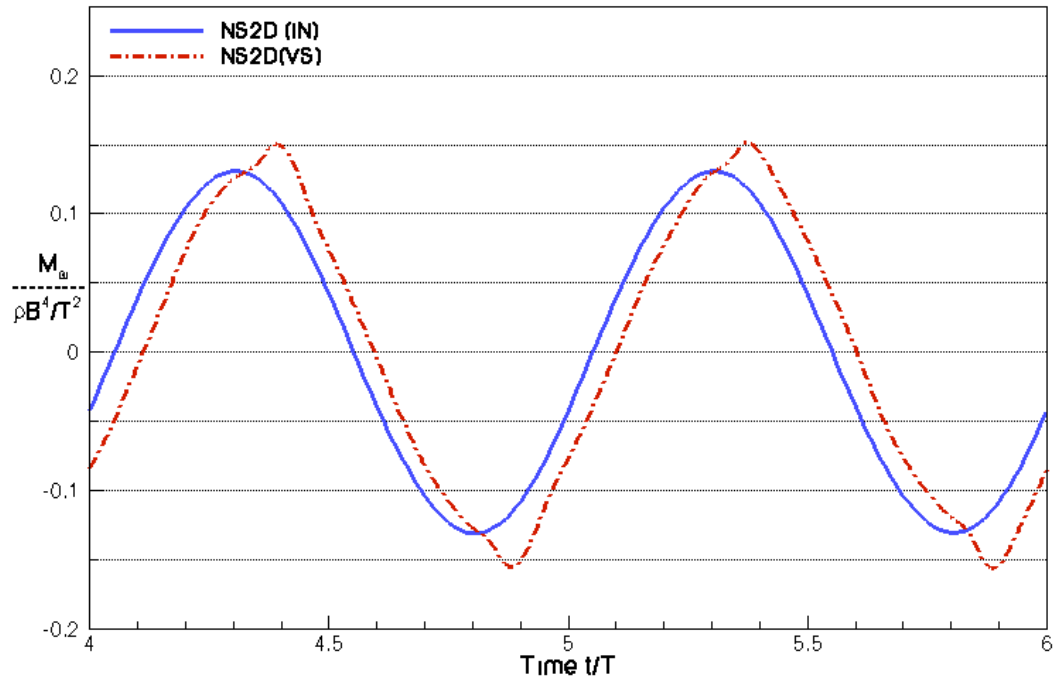


Figure 5.14: Comparison between the moment histories from NS2D(IN) and NS2D(VS). (round bilge hull, $\alpha_0=5.75^\circ$, $Fn=0.6$).

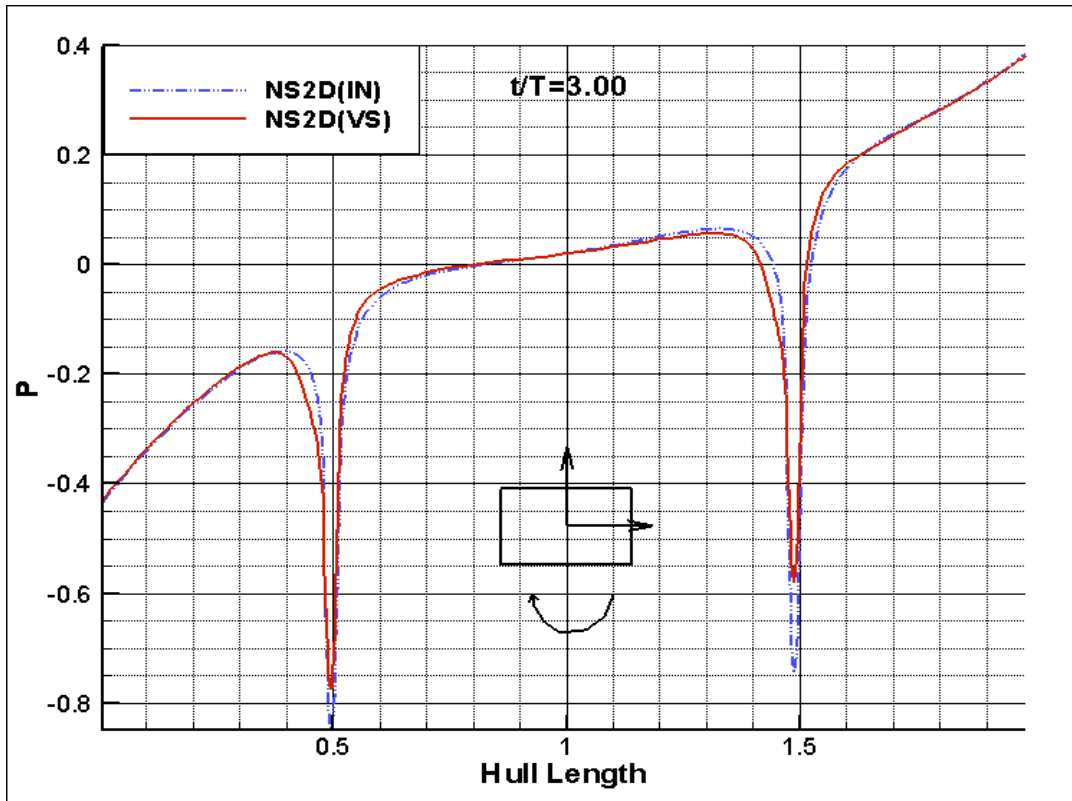


Figure 5.15: Comparison of the pressure distribution along the FPSO hull between results from NS2D(IN) and NS2D(VS) (round bilge hull, $\alpha_0=5.75^\circ$, $Fn=1.0$ and $t/T=3.00$).

The meshes used in NS2D and FLUENT are presented in Fig. 5.16 and Fig. 5.17, respectively. For the round bilge model, The total number of cells used in NS2D is around 10,000, and the FLUENT mesh has a total number of 62,000 cells consisting of 22,000 cells in air and 40,000 cells in water. In FLUENT, the VOF algorithm is implemented to predict the free surface, which increases the total number of cells significantly. Moreover, based on the numerical experience, a much higher resolution is needed near the hull in order to capture the boundary layer vorticity. Therefore, a grid refinement zone is applied to the area near the hull and close to the free surface, where a

quadrilateral cell is divided into four cells and hanging nodes are allowed at the boundary of the grid refinement zone.

The free-surface elevations from both solvers are presented in Fig. 5.18, where the roll frequency is fixed at $F_n=0.8$ and the roll amplitude is given as $\alpha_o=5.75^\circ$. The background contour represents the volume fraction of water from FLUENT, where the three contour levels are 0.45, 0.50, and 0.55, and the level of 0.5 represents the free-surface elevation. Note that in FLUENT, as mentioned earlier, a small numerical reflection is observed at the grid zone interface, which is very difficult to avoid. The assumption here is that the grid zone interface is far enough and the numerical reflection is small enough to be neglected. For the same case, the corresponding roll moment histories are shown Fig. 5.19. Note that the moment history presented in this chapter indicates the hydrodynamic roll moment, unless mentioned otherwise. Figures 5.20 to 5.22 present the vorticity magnitude contours from NS2D, FLUENT(L) and FLUENT(T) respectively. Note that in FLUENT(T), the $k-\omega$ turbulent model is applied, where the y -plus for the corresponding mesh is around 10. A good correlation has been found between the results from NS2D and FLUENT, where the slight difference on the vorticity magnitude is due to grid resolution. Also, the turbulent flow effect is found to be insignificant in the case of a round bilge hull. The dash-dotted line represents the moment history obtained using Eq. (5.3), where the hydrodynamic coefficients are extracted from the NS2D roll moment history in the same figure by following Eq. (5.4). It has been found that using added-mass and damping coefficients to represent a periodic force or moment histories can be inadequate, particularly for the hulls subject to roll motions. In fact, two moment histories with a 15% difference on the amplitude can have same hydrodynamic coefficients, and a slight phase shift between two moment histories can

result in a significant difference on the corresponding coefficients even with same roll moment amplitude.

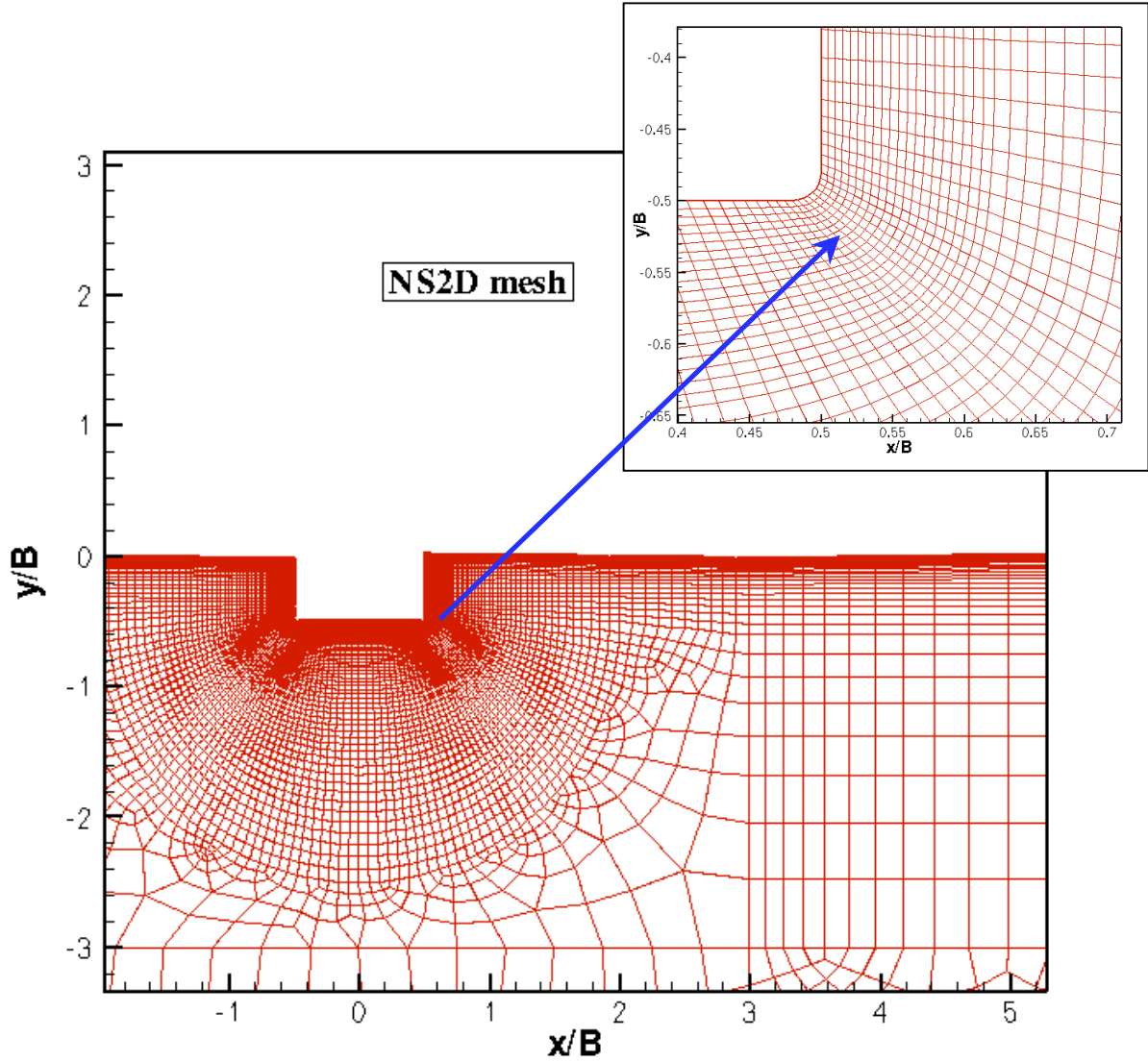


Figure 5.16: Mesh used in NS2D ($N \approx 10,000$) and the blowup view at the bilge area.

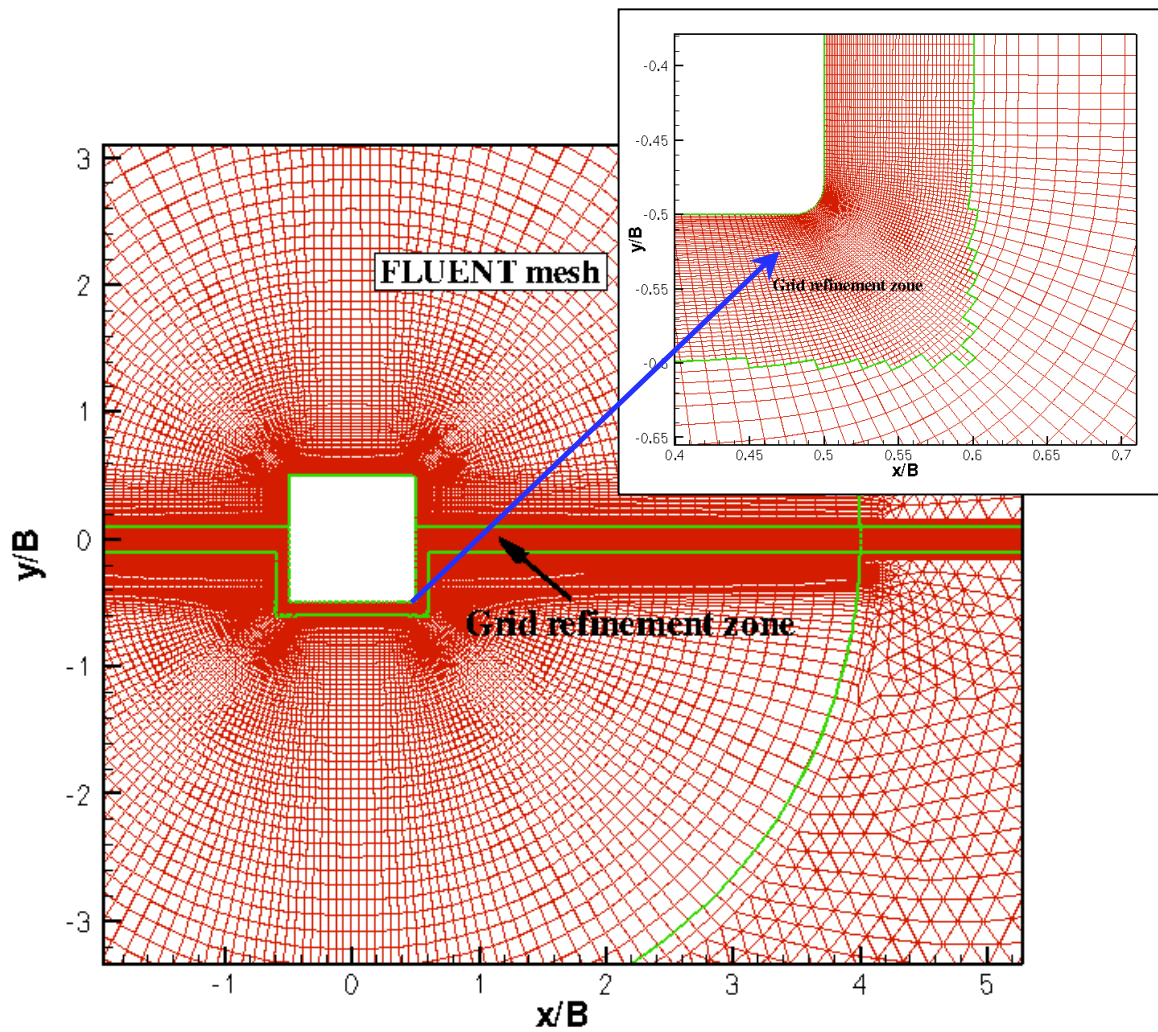


Figure 5.17: Mesh used in FLUENT ($N \approx 62,000$, air/water $\approx 22,000/40,000$) and the blowup view at the bilge area.

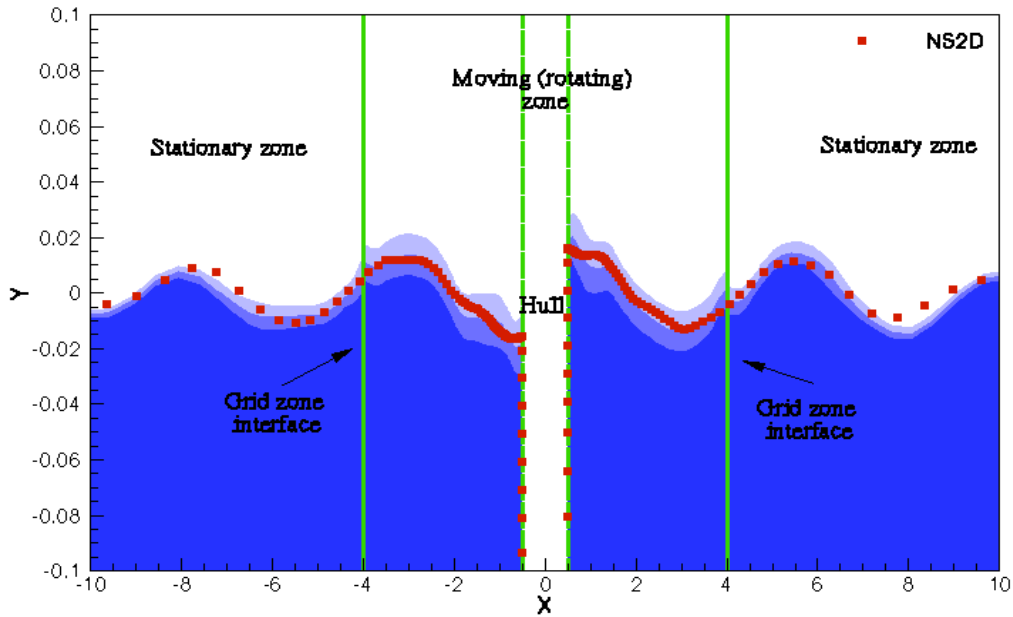


Figure 5.18: Comparison between the wave elevations from NS2D and the volume fraction of water (background contour) from FLUENT(L) at three levels, 0.45, 0.50 and 0.55 (round bilge hull, $\alpha_0=5.75^\circ$, $Fn=0.8$ and $t/T=5.00$).

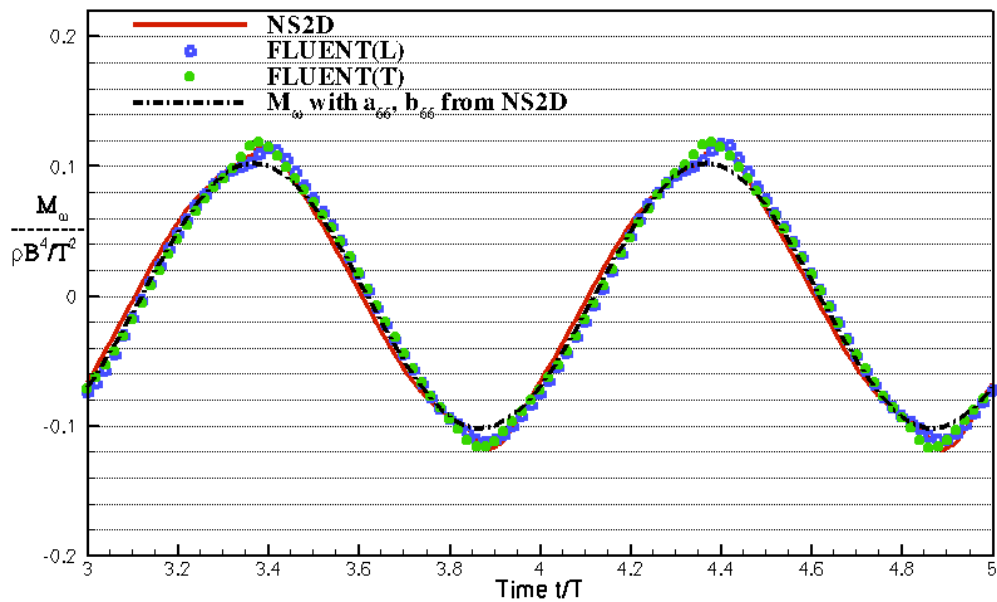


Figure 5.19: Comparison of the moment histories from NS2D, FLUENT(L), FLUENT(T) (round bilge hull, $\alpha_0=5.75^\circ$, $Fn=0.8$ and $t/T=5.00$).

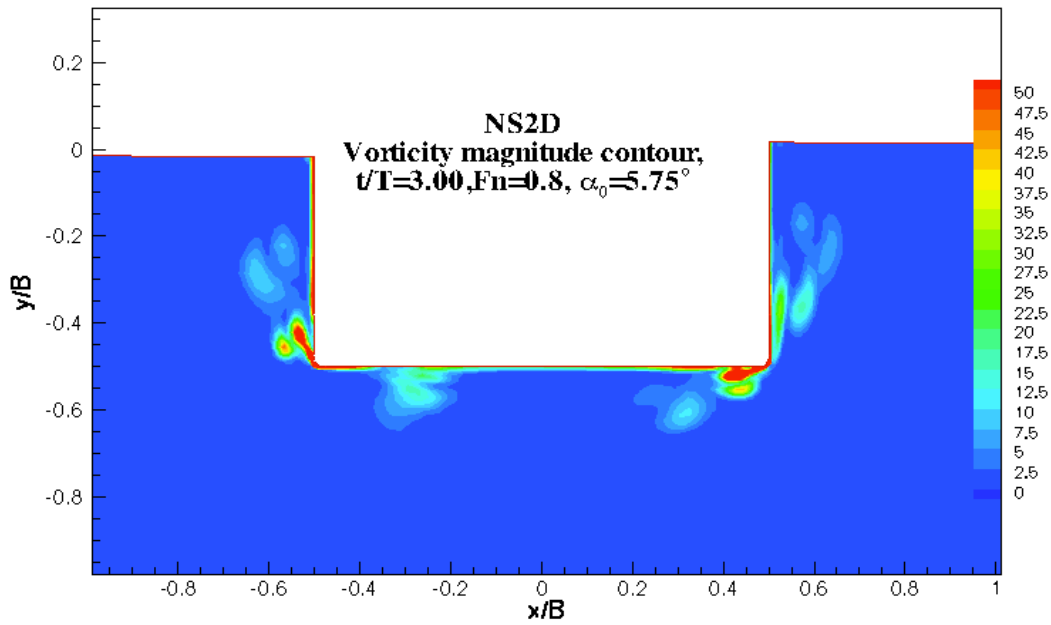


Figure 5.20: Vorticity magnitude contour From NS2D (round bilge hull, $\alpha_0=5.75^\circ$, $Fn=0.8$ and $t/T=3.00$).

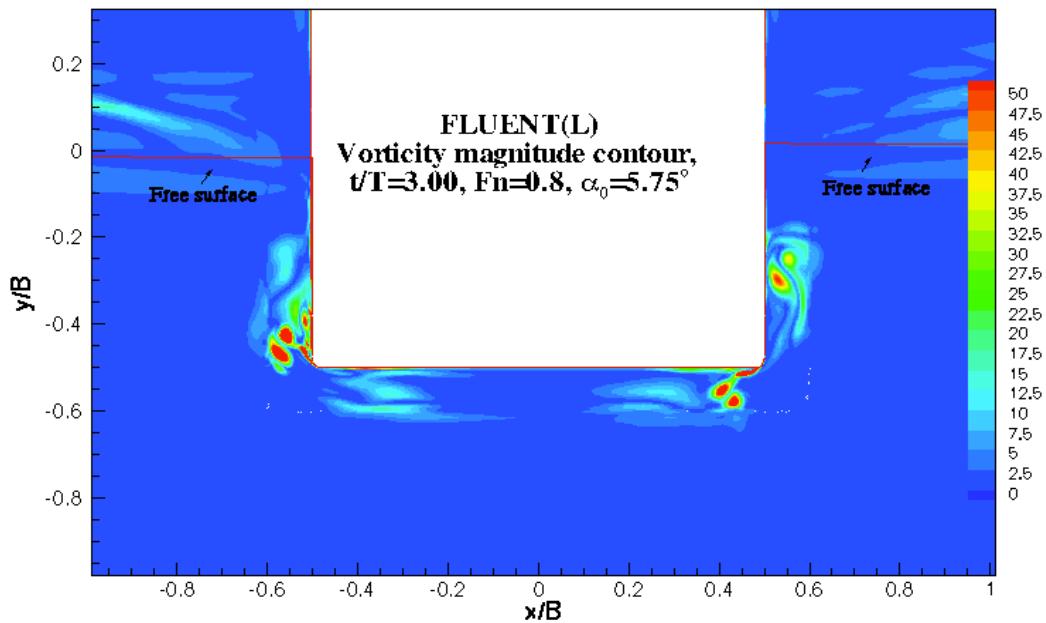


Figure 5.21: Vorticity magnitude contour From FLUENT(L) (round bilge hull, $\alpha_0=5.75^\circ$, $Fn=0.8$ and $t/T=3.00$).

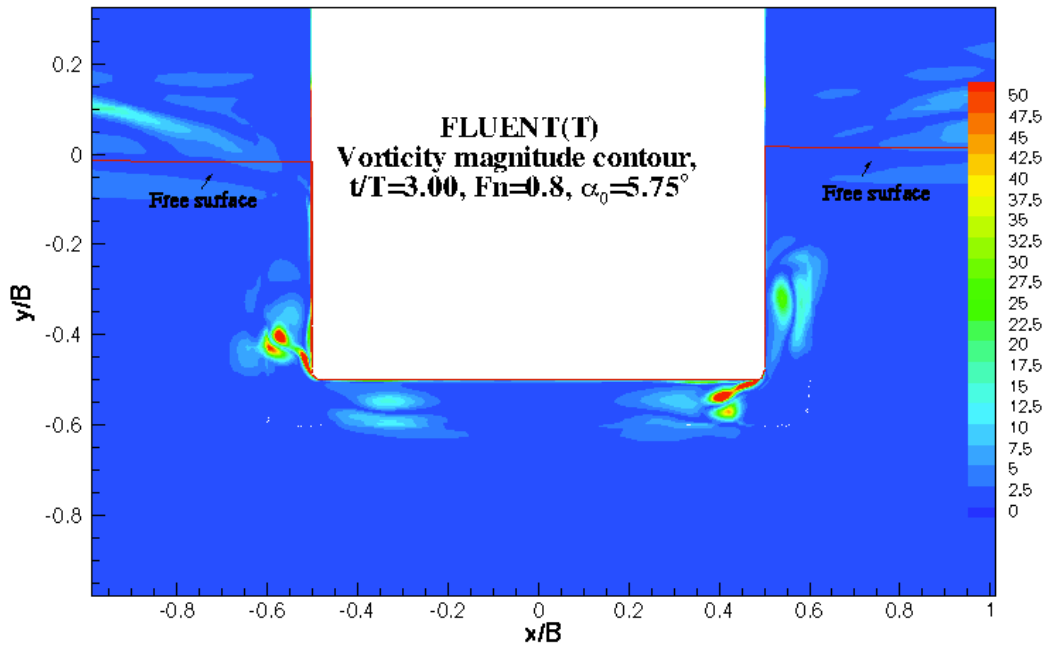


Figure 5.22: Vorticity magnitude contour From FLUENT(T) (round bilge hull, $\alpha_0=5.75^\circ$, $Fn=0.8$ and $t/T=3.00$).

The NS2D results are also compared to the numerical results from FSRVM and the experimental measurements provided by Yeung et al. (1998) and Roddier (2000)⁶. Figures 5.23 and 5.24 show the comparison of the moment histories from NS2D and from other methods. The moment history from NS2D agrees well with the numerical and experimental results from Roddier (2000). In fact, the results from NS2D are closer to Roddier's (2000) experimental data as compared to his own numerical results. As mentioned earlier, it may not be adequate to use added-mass and damping coefficients to represent the moment history. However, in order to compare with other methods, the corresponding added-mass and damping coefficients from NS2D(IN), NS2D(VS), FLUENT(L), FLUENT(T) and all other methods are all presented in Fig. 5.25 and Fig.

⁶ Note that the experimental uncertainty is not mentioned in their study.

5.26. The NS2D results also agree fairly well with those from other methods except for low Froude number cases, where slight differences are observed. As expected, the inviscid results are high in added-mass coefficients and low in damping coefficients. When the roll frequency is lower, a longer wavelength is created. Therefore, it is much more difficult for either NS2D or FLUENT to simulate those cases because a much larger numerical domain is required in order to avoid the wave reflection from the far boundaries. In terms of added-mass coefficients, FLUENT results are slight closer to the experimental data as compared to the NS2D results for $F_n=0.4$ and $F_n=0.6$. As to the damping coefficients, it is the results from NS2D that show better agreement with the experimental data than those from FLUENT.

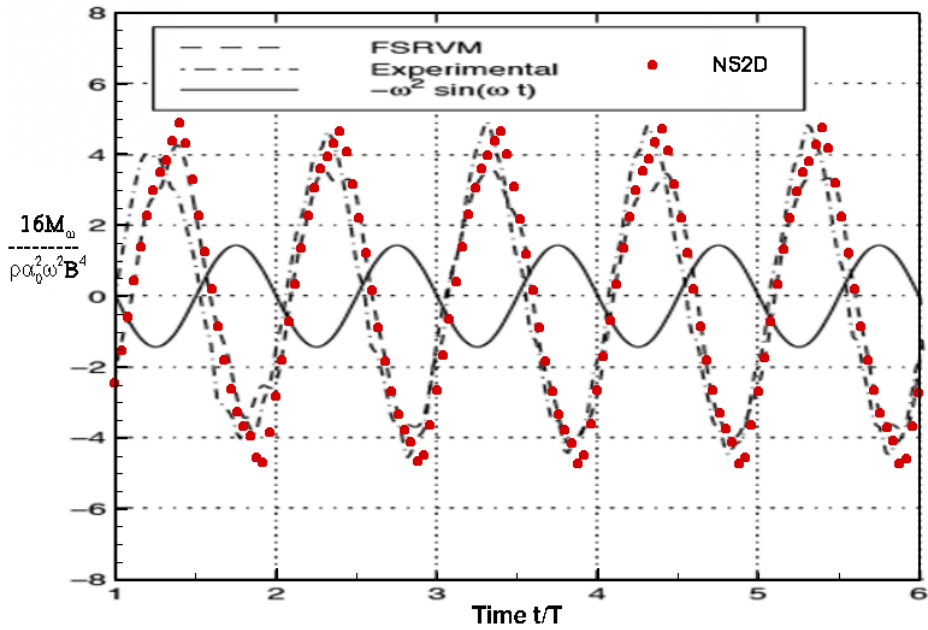


Figure 5.23: Moment histories from NS2D and other methods (round bilge hull, $\alpha_0=5.75^\circ$, $Fn=0.8$ and $-\omega^2 \sin(\omega t)$ represents the angular acceleration).

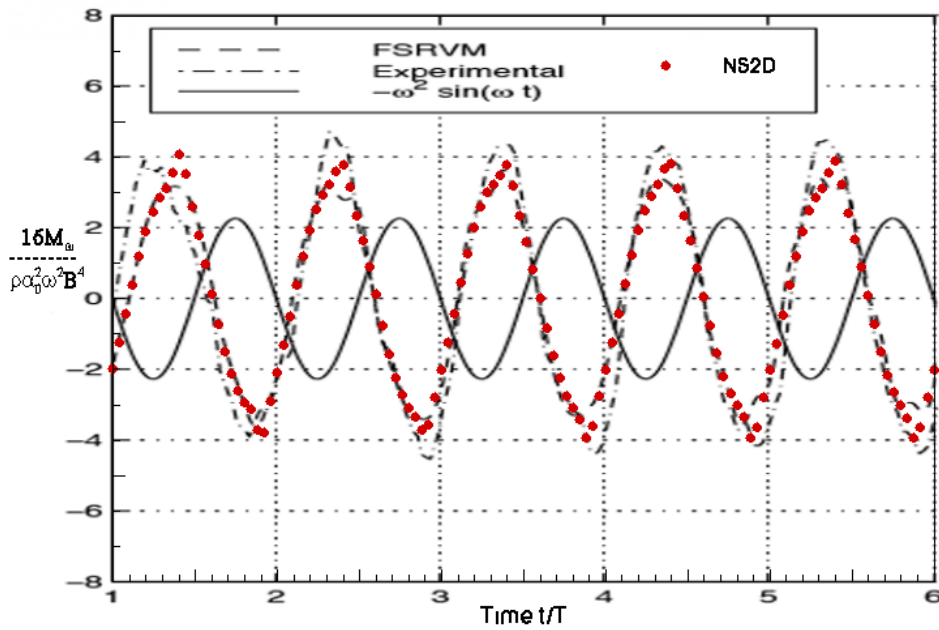


Figure 5.24: Moment histories from NS2D and other methods (round bilge hull, $\alpha_0=5.75^\circ$, $Fn=1.0$ and $-\omega^2 \sin(\omega t)$ represents the angular acceleration).

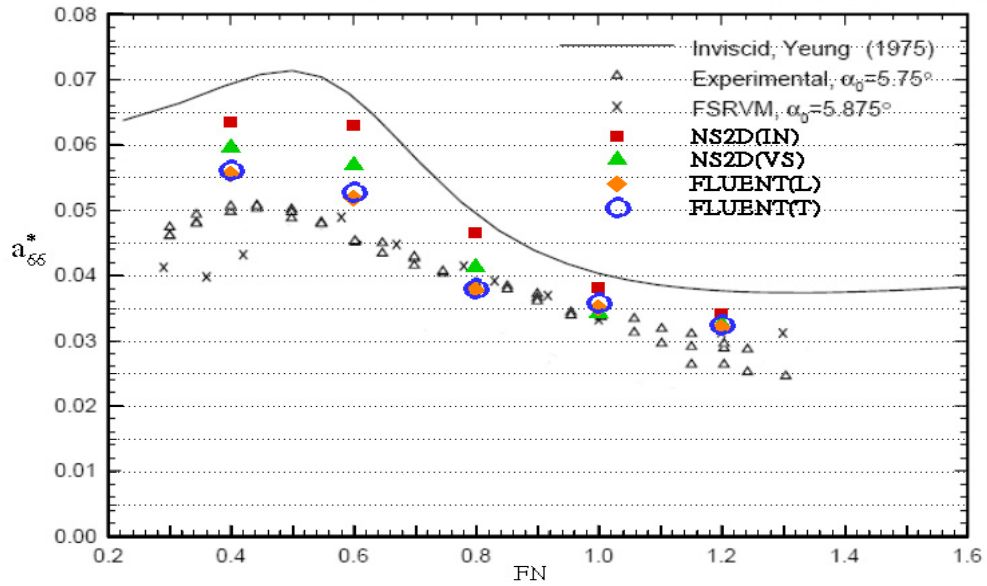


Figure 5.25: Added-mass coefficients from NS2D, FLUENT, and other methods (round bilge hull and $\alpha_0=5.75^\circ$).

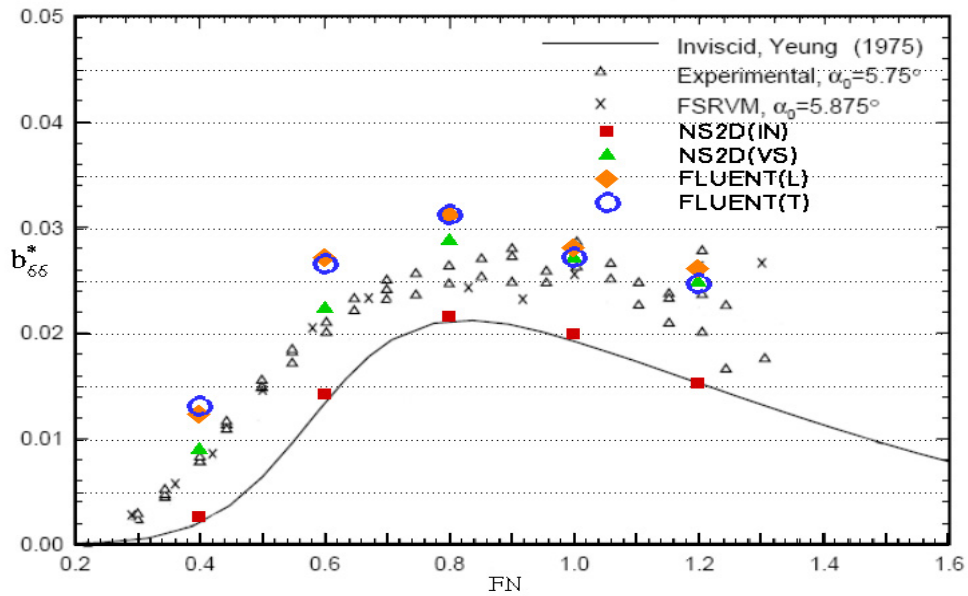


Figure 5.26: Damping coefficients from NS2D, FLUENT, and other methods (round bilge hull and $\alpha_0=5.75^\circ$).

4% Bilge Keel Model, Box Model and Step Model

The following discussions present the comparisons of the simulations for 4% bilge keel model, box model and step model from NS2D and other methods.

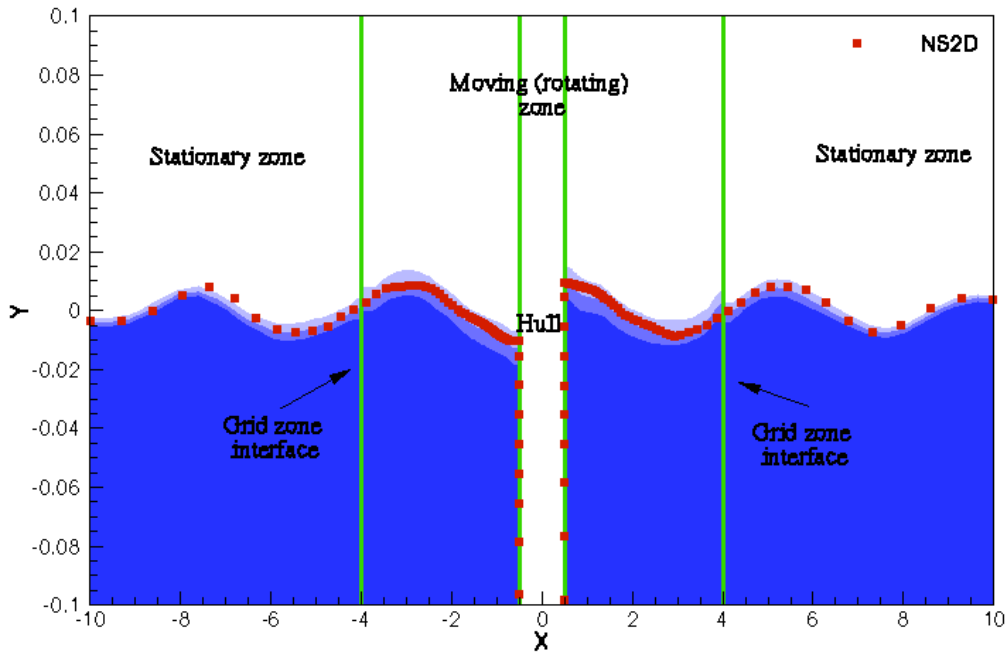


Figure 5.27: Comparison between the wave elevations from NS2D and the volume fraction of water (background contour) from FLUENT(L) at three levels, 0.45, 0.50 and 0.55 (4% bilge keel hull, $\alpha_0=2.87^\circ$, $Fn=0.8$ and $t/T=6.00$).

In the case of the 4% bilge keel model, the simulations are performed with a given roll angle amplitude, $\alpha_0=2.87^\circ$. The comparison between the free-surface elevations from NS2D and FLUENT(L) is presented in Fig. 5.27, and the results from these two solvers agree well. The vorticity magnitude contours for $Fn=0.8$ from NS2D, FLUENT(L) and FLUENT(T) are presented in Fig. 5.28 to Fig. 5.30, respectively. Moreover, the moment histories from these three solvers for $Fn=0.6$ and $Fn=0.8$ are shown in Fig. 5.31 and Fig. 5.32. The simulations from NS2D, FLUENT(L) and FLUENT(T) show similar flow

visualization near the bilge keel area. For flows away from the hull, the FLUENT(T) simulation has the strongest dissipation, where the shed vortices are dissipated faster as compared to the other two simulations. In fact, these shed vortices have very little impact on the pressure distribution on the hull surface. As a result, the moment histories from these simulations show fairly good agreement. The dash-dotted line in Fig. 5.31 and Fig. 5.32 represents the moment history obtained using the linear combination of a_{66} and b_{66} , which are extracted from the NS2D roll moment history in the same figure. The difference between the dash-dotted line and the moment history from NS2D shows that even with a small roll angle amplitude ($\alpha_o=2.87^\circ$), the non-linear effects are still observed, particularly for hulls with sharp corners. Also notice that the FLUENT mesh in this case uses the grid refinement, which gives a much higher grid resolution in the area close to the hull. It also explains the reason why the predictions of the shed vortices from NS2D are different from the FLUENT(L) results. It has also been found that the effect of turbulence has very little impact on the prediction of hydrodynamic loads on the hull in the case of ship-shaped hull roll motions. Therefore, no turbulent model is applied in NS2D, and all the following studies are performed in laminar flow.

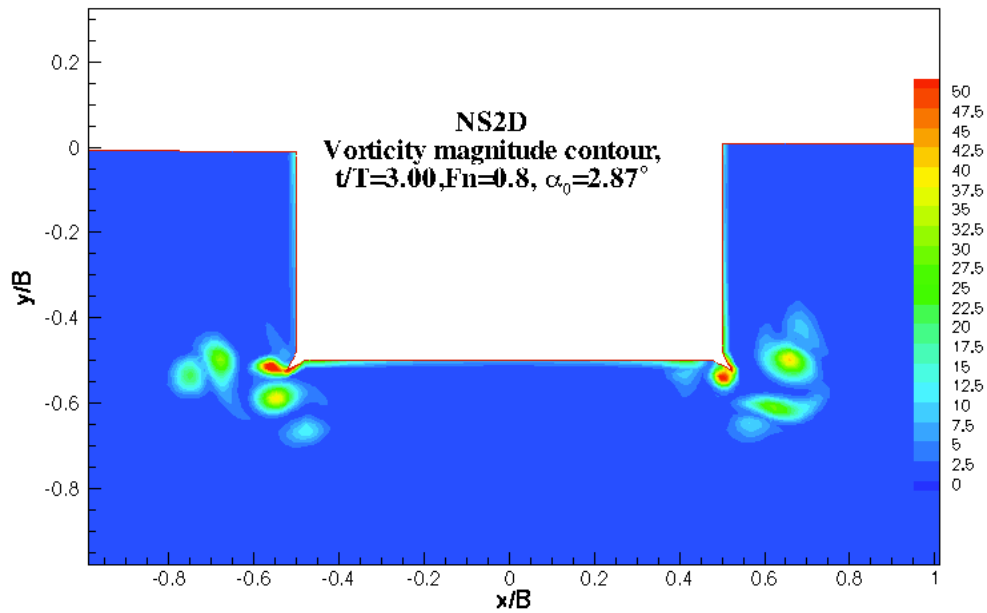


Figure 5.28: Vorticity magnitude contour From NS2D (4% bilge keel hull, $\alpha_0=2.87^\circ$, $Fn=0.8$ and $t/T=3.00$).

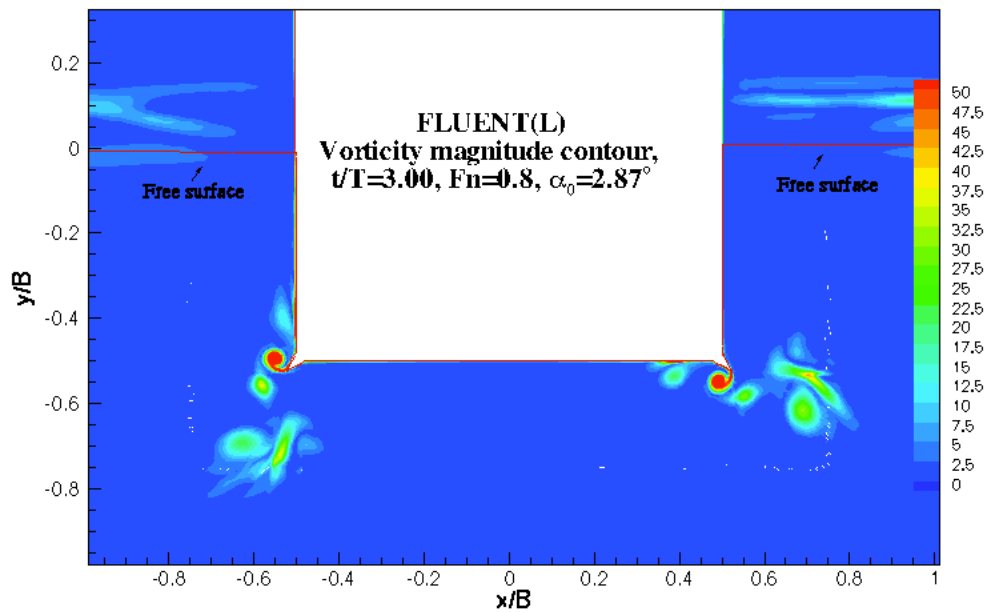


Figure 5.29: Vorticity magnitude contour from FLUENT(L) (4% bilge keel hull, $\alpha_0=2.87^\circ$, $Fn=0.8$ and $t/T=3.00$).

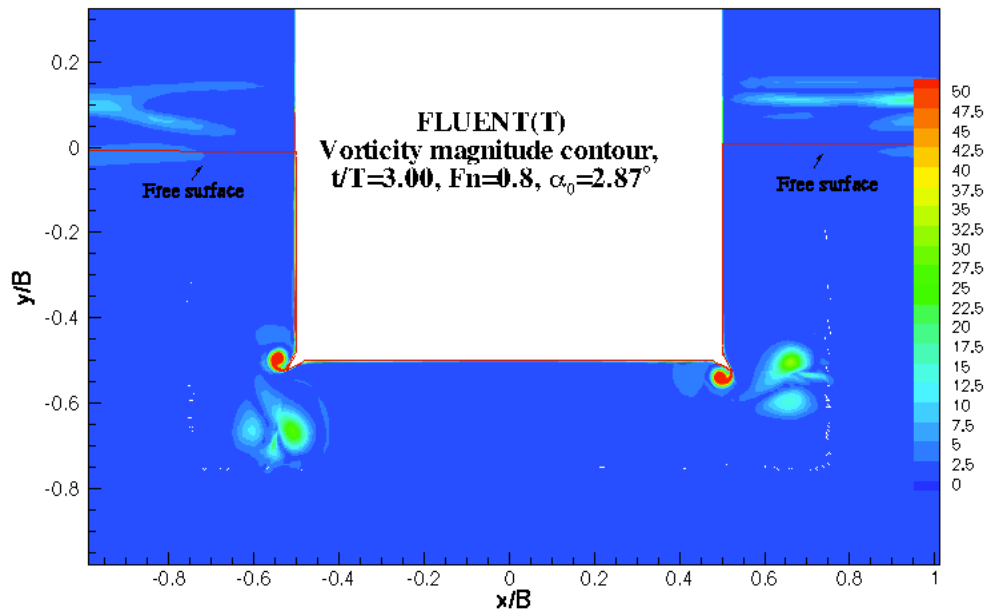


Figure 5.30: Vorticity magnitude contour from FLUENT(T) (4% bilge keel hull, $\alpha_0=2.87^\circ$, $Fn=0.8$ and $t/T=3.00$).

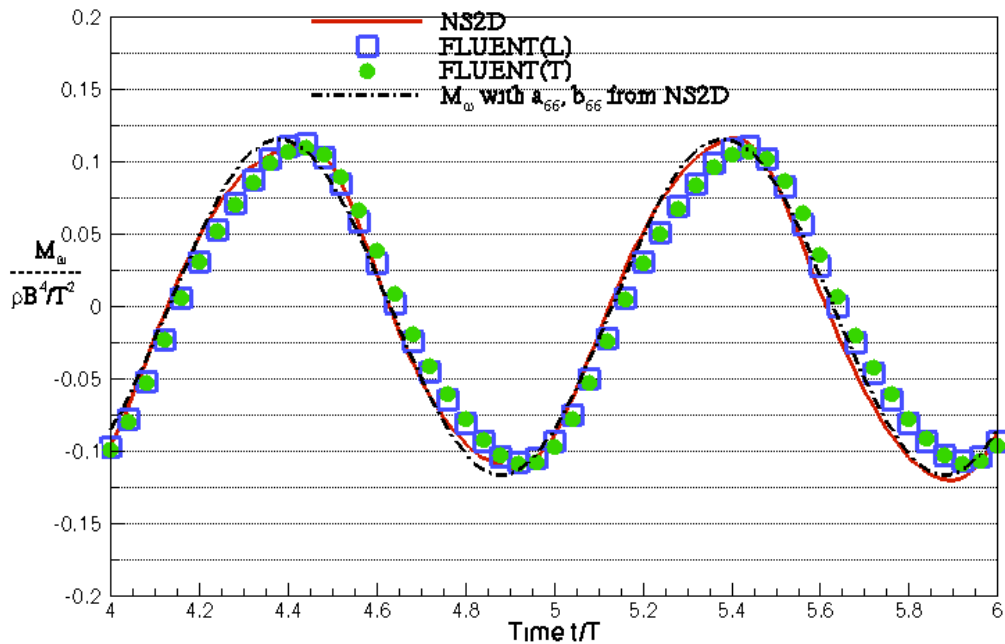


Figure 5.31: Moment histories for $Fn=0.6$ from NS2D, FLUENT(L), and FLUENT(T) (4% bilge keel hull, $Fn=0.8$ and $\alpha_0=2.87^\circ$).

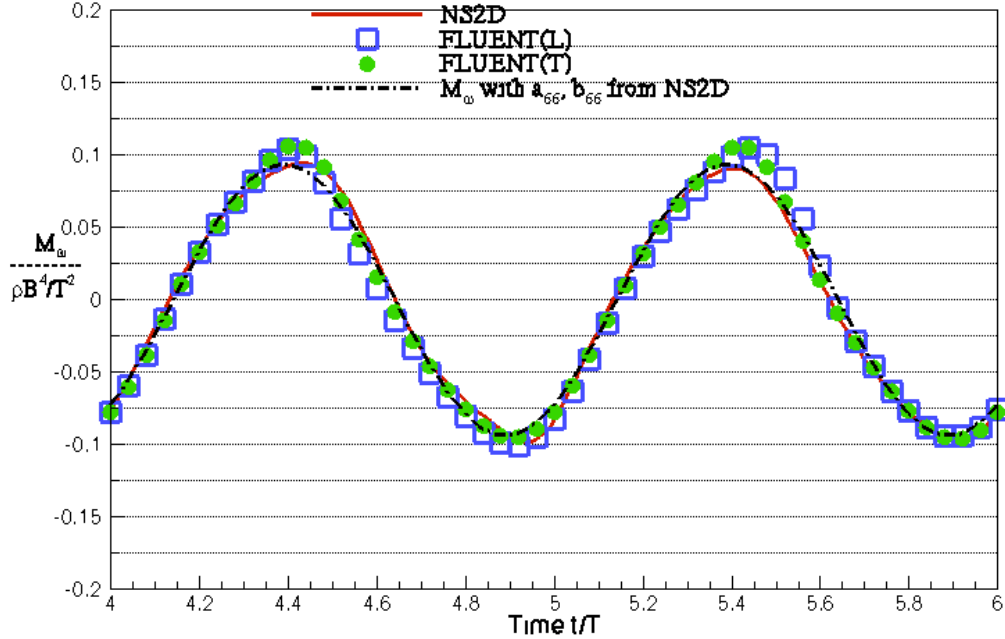


Figure 5.32: Moment histories for $Fn=0.8$ from NS2D, FLUENT(L) and FLUENT(T) (4% bilge keel hull and $\alpha_0=2.87^\circ$).

The NS2D results for the 4% bilge keel model are also compared to those from other numerical methods (FSRVM and BFFDM) and to the experiment data provided by Yeung et al. (2000), where the hull geometry in NS2D is exactly the same as the one used in Yeung et al.'s (2000) numerical simulation. Figure 5.33 shows the corresponding moment histories for $\alpha_0=2.87^\circ$ and $Fn=0.8$. According to Yeung et al. (2000), the numerical and experimental data presented in the figure are the hydrodynamic moments. It has been found that in order to be consistent with the hydrodynamic coefficients, as shown in Fig. 5.34 and Fig. 5.35, it is more reasonable to believe that the data in Fig. 5.33 from Yeung et al. (2000) represent the total moment histories. The moment history from the NS2D simulation compares fairly well with those from other methods. However, the prediction of hydrodynamic coefficients from NS2D and FLUENT tend to be higher than those from Yeung et al. (2000), particularly for damping coefficients, and unfortunately,

their article is the only literature that provides a complete study for hulls with sharp bilge keel subject to prescribed rolls. On the other hand, the comparisons between NS2D and FLUENT show good agreement for all cases except for $F_n=0.6$, where the prediction of the added-mass coefficient from NS2D is much higher than the one from FLUENT. It is interesting that even though the moment histories for $F_n=0.6$ from NS2D and FLUENT show good agreement, particularly in terms of roll moment amplitude, as plotted in Fig. 5.31, the corresponding added-mass coefficients can have a significant difference. It has been found that, it is more difficult for numerical solvers to perform studies on low roll frequencies. The simulation for low roll frequencies requires a larger computational domain due to the longer outgoing wavelength. Moreover, because the wave elevation is smaller for low roll frequencies, a higher grid resolution is needed near the free surface in order for NS2D or FLUENT to maintain the accuracy for tracking or capturing the free surface.

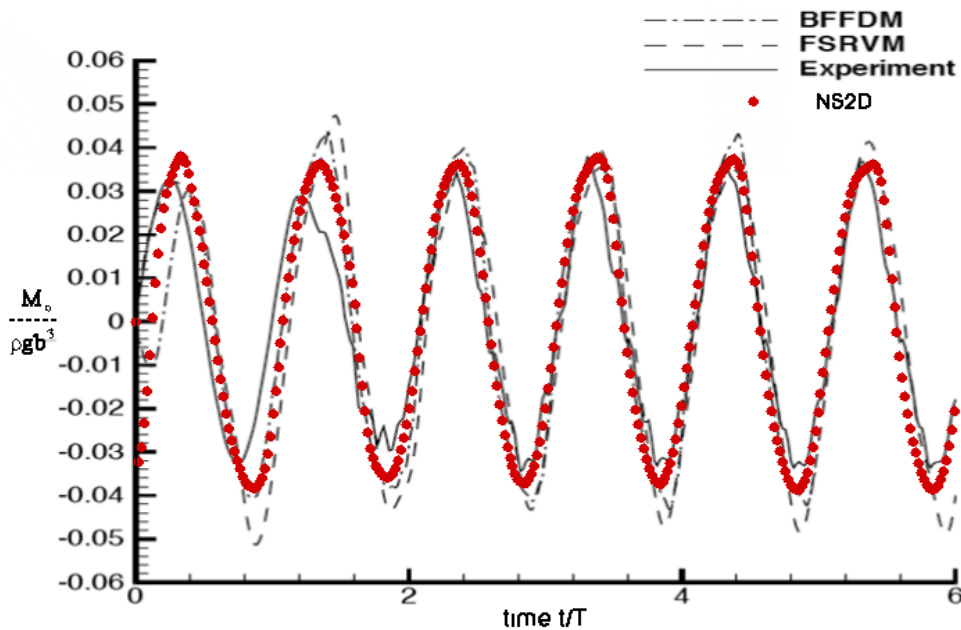


Figure 5.33: Histories of total moment from NS2D and other methods ($F_n=0.8$ and $\alpha_0=2.87^\circ$).

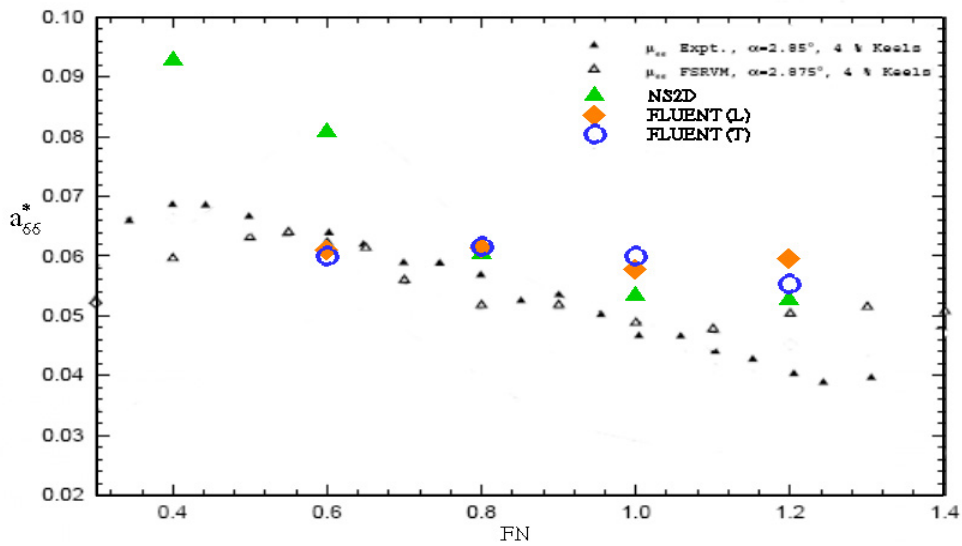


Figure 5.34: Added-mass coefficients from NS2D, FLUENT, and other methods (4% bilge keel hull and $\alpha_0=2.87^\circ$).

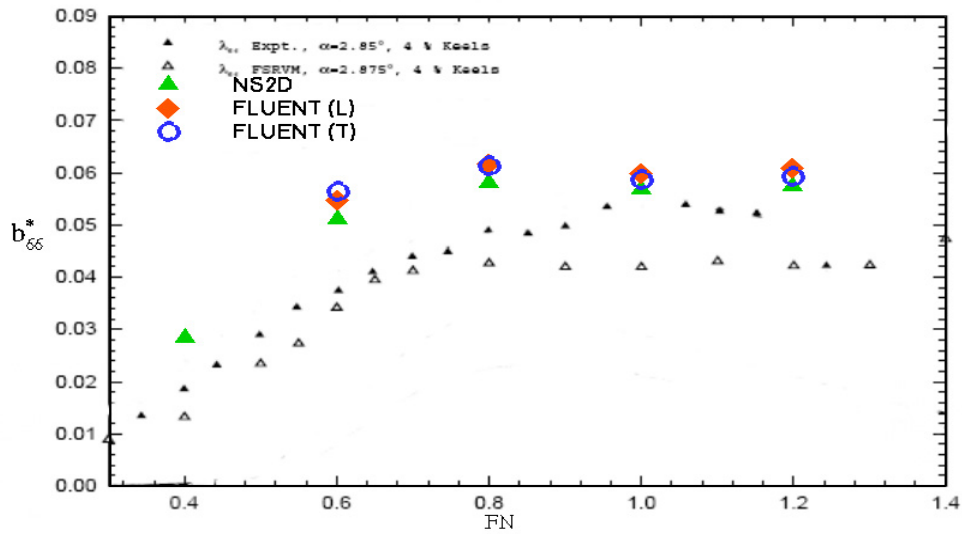


Figure 5.35: Damping coefficients from NS2D, FLUENT, and other methods (4% bilge keel hull and $\alpha_0=2.87^\circ$).

In the following studies, NS2D is applied to two other hull geometries, the box and step models, where NS2D results are compared to those experimental data measured by Yuck et al. (2003). According to the definition of the bilge keel length, the geometry of a box hull is very similar to the one of 1% bilge keel, and the length of the "step" in a step model is very close to the length of a 4% bilge keel. The damping coefficients for the box and step models with a roll amplitude of $\alpha_0=5^\circ$ are presented in Fig. 5.36 and Fig. 5.37, respectively. As shown in the figure, the results from NS2D compare extremely well to the experimental data provided by Yuck et al. (2003). Thus, it proves that the NS2D simulation is reliable for predicting the corresponding hydrodynamic loads on hulls with sharp corners.

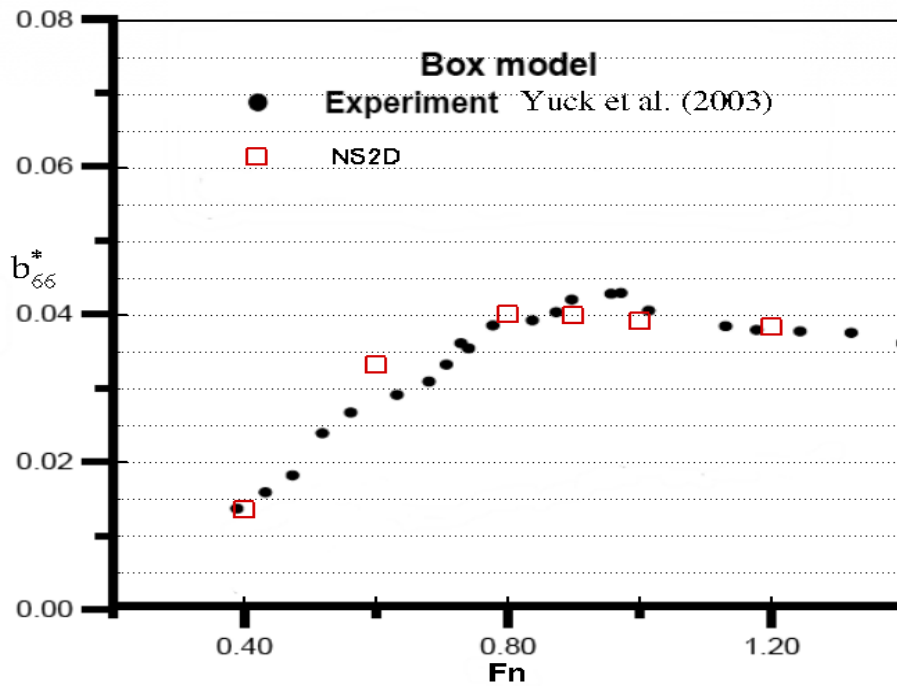


Figure 5.36: Damping coefficients for the box model with $\alpha_0=5.0^\circ$.

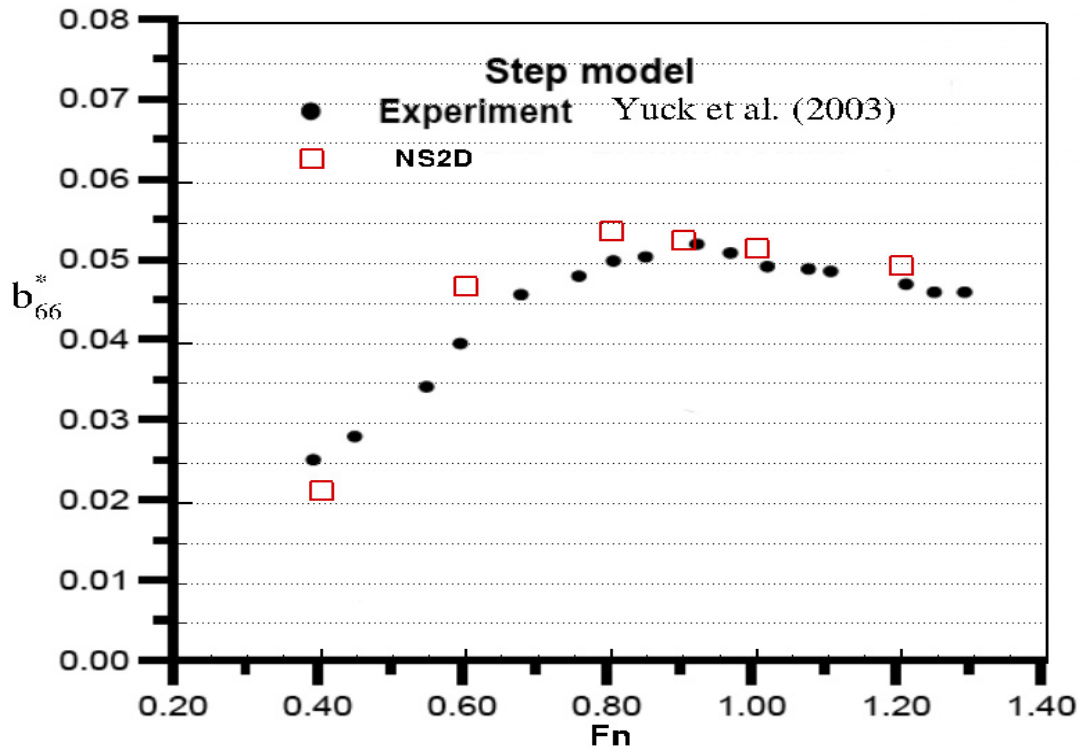


Figure 5.37: Damping coefficients for the step model $\alpha_0=5.0^\circ$.

5.1.5 The Effect of The Free Surface

It is essential to observe the effects of the free surface, which are studied by comparing the results from a submerged hull to those from a ship-shaped hull. In the study, a fixed roll angle amplitude is give at $\alpha_0=5.75^\circ$. Figure 5.38 shows the comparison of the free-surface elevation of two extreme cases, $Fn=0.4$ and $Fn=1.2$. As expected, a higher roll frequency creates a higher acceleration, which results in a larger wave. Figures 5.39 and 5.40 compare the moment histories from a submerged hull and a ship-shaped hull for $Fn=0.4$ and $Fn=1.2$, respectively. Note that the round bilge model is used in the studies, and the moment history from the submerged hull needs to be divided by 2

in order to have the same hull length as compared to a ship-shaped hull. In the case of a submerged hull, the study for different roll frequencies becomes the study of the viscous effect, and it is negligible in this case. On the other hand, with the presence of the free surface, the moment amplitude increases as the roll frequency decreases. It is understandable that when the hull rotates, flow near the hull moves along with the body. Nevertheless, with the presence of the free surface, the flow movement is limited in the hull-rotating direction, and the hull motion induces a wave on each side of the hull, which propagates from the hull toward the far boundary. In the case of a higher roll frequency, the wave amplitude is larger, which carries more energy away from the hull, and results in a larger phase shift on the moment history. Conversely, more energy is constrained in the case of a lower roll frequency, which results in a greater amplitude in roll moment.

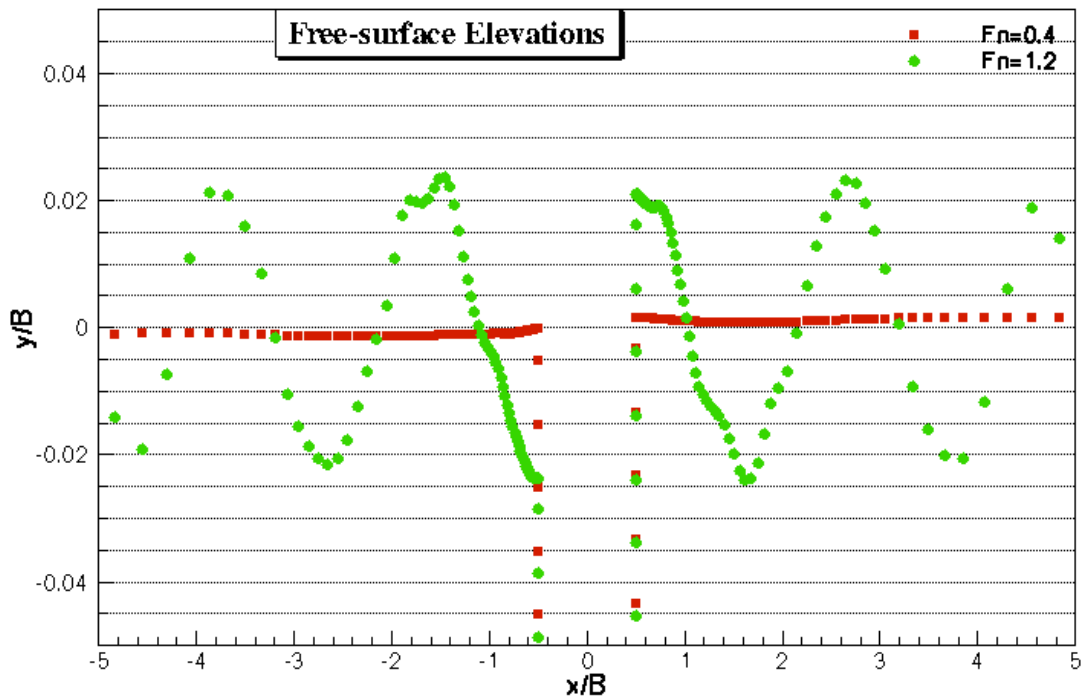


Figure 5.38: Free-surface elevations in the case of $F_n=0.4$ and $F_n=1.2$ ($\alpha_0=5.75^\circ$).

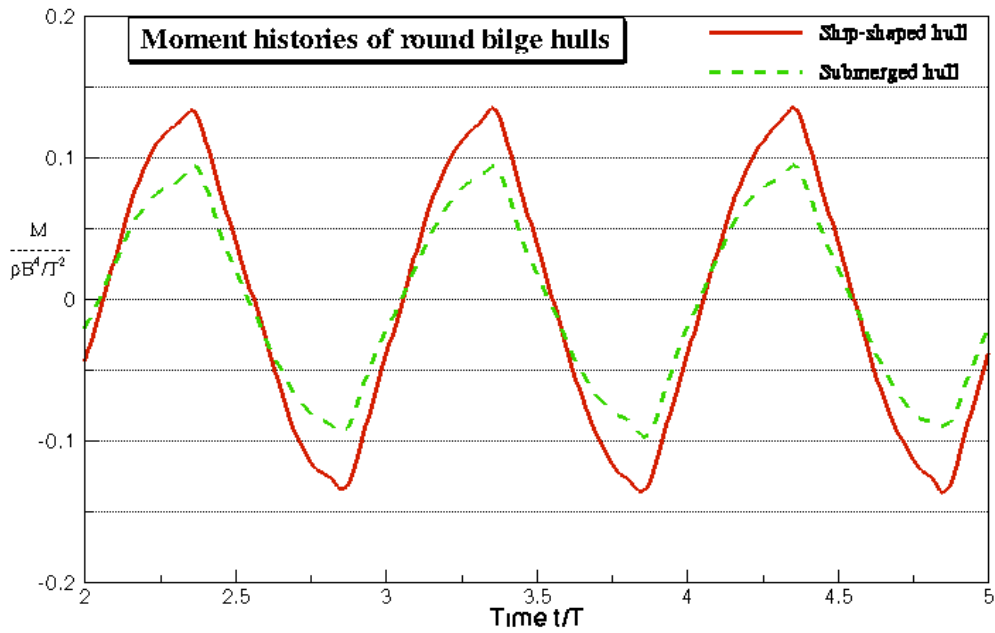


Figure 5.39: Comparison between the moment histories for a ship-shaped hull and a submerged hull (round bilge hull, $F_n=0.4$ and $\alpha_0=5.75^\circ$).

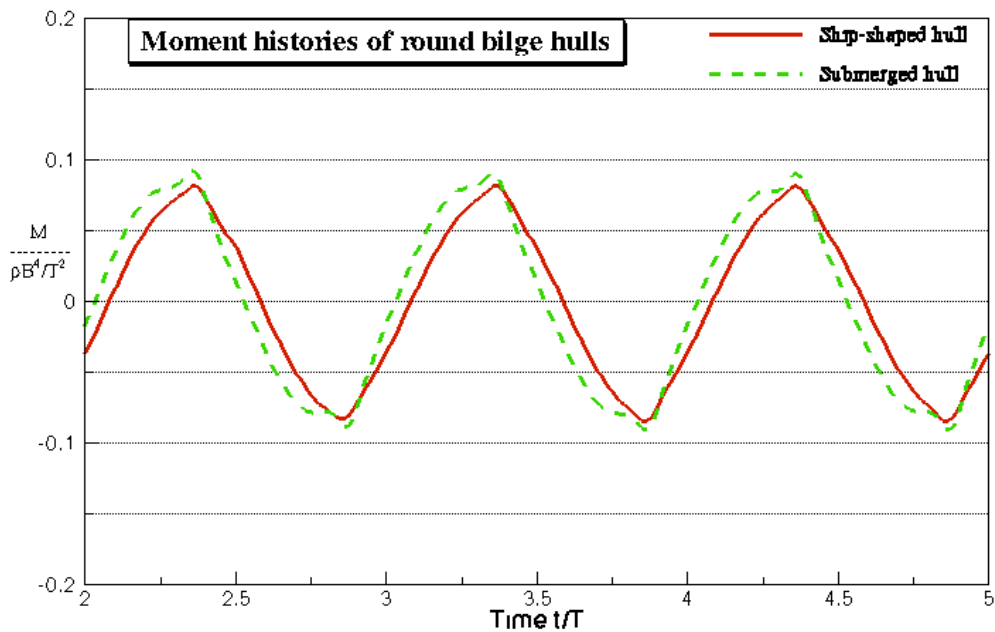


Figure 5.40: Comparison between the moment histories for a ship-shaped hull and a submerged hull (round bilge hull, $F_n=1.2$ and $\alpha_0=5.75^\circ$).

5.1.6 The Effect of Roll Angle Amplitude

The maximum roll angle that the present numerical scheme can handle is up to 20 degrees. Therefore, in the following studies, the maximum roll angle is set to $\alpha_0=20^\circ$, along with three other roll angles, $\alpha_0=5^\circ$, 10° and 15° . The moment histories for the round bilge model with different roll amplitudes are shown in Fig. 5.41. The curve of the scaled roll motion α/α_0 is presented as a reference. F_n is equal to 1, and the moment histories are scaled by $\alpha_0=5^\circ$. The non-linear behavior of the moment histories can be found when the roll angle is beyond 10 degrees, where the viscous effect is more significant.

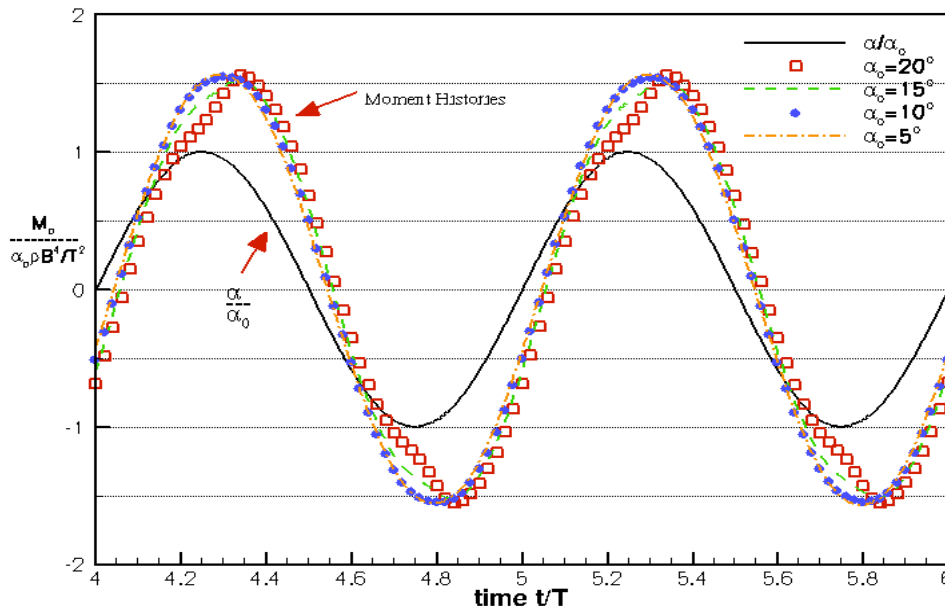


Figure 5.41 Total moment histories of round bilge model for different roll angles (scaled by $\alpha_0=5^\circ$).

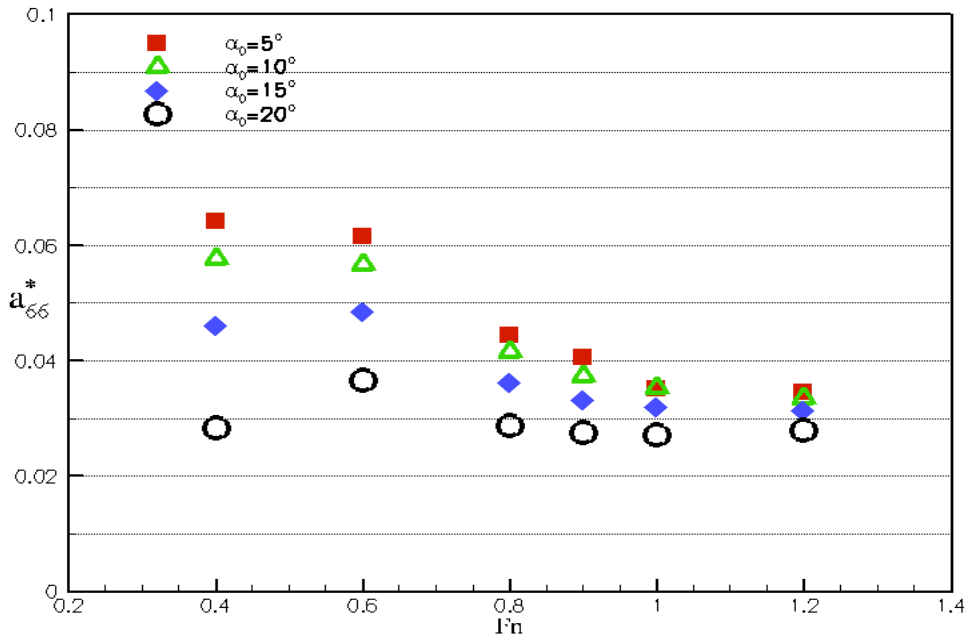


Figure 5.42: Roll added-mass coefficients for the round bilge model ($\alpha_0=5^\circ, 10^\circ, 15^\circ, 20^\circ$).

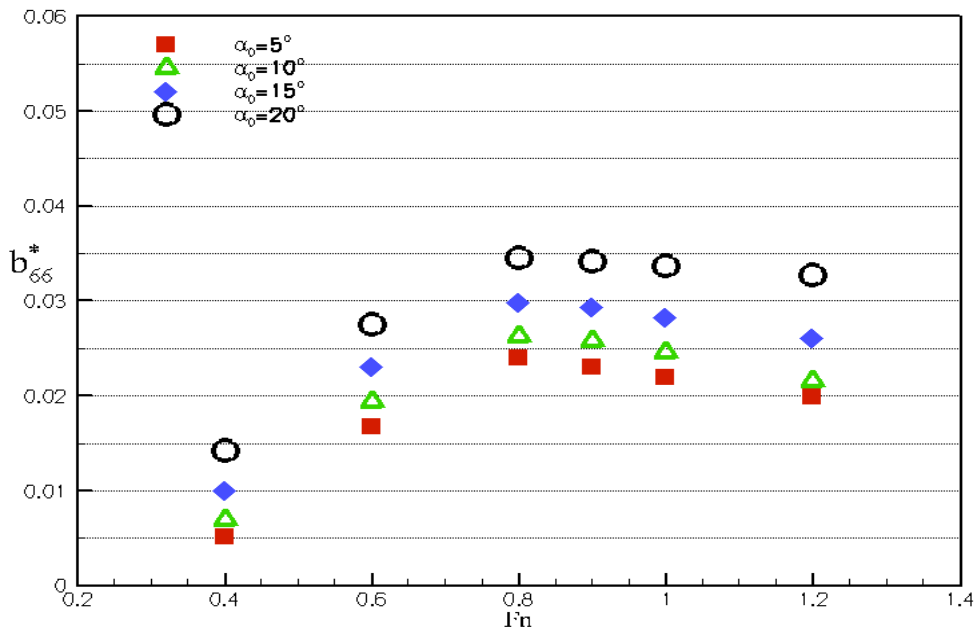


Figure 5.43: Roll damping coefficients for the round bilge model ($\alpha_0=5^\circ, 10^\circ, 15^\circ, 20^\circ$).

The added-mass and damping coefficients for different F_n are presented in Fig. 5.42 and Fig. 5.43 respectively. The moment amplitude is about the same for different α_0 , but a phase shift is found and becomes larger under higher α_0 . It is due to the presence of the viscosity, and those vortices near the bilge are stronger when α_0 is larger. This phase shift results in a decrease on a_{66} and an increase on b_{66} . Note that a similar trend was also found by Vugts (1968).

5.1.7 The Effect of Hull Geometry

Flow visualization and the corresponding forces for four above-mentioned hull geometries are studied with a roll amplitude of $\alpha_0=5.75^\circ$. The moment histories for different hull geometries in the case of $F_n=1$ are plotted in Fig. 5.44. The added-mass and damping coefficients for various F_n are shown in Fig. 5.45 and Fig. 5.46 respectively. The vorticity contours for $F_n=1.0$ are shown in Fig. 5.47. The simulations from different hull models show different flow patterns near the hull, where the shed vortices location and strength are affected by the hull geometries. In fact, the location and strength of the vortices near the hull also affect the pressure distribution near the hull and more importantly, on the hull surface. The pressure distributions along the hull surface for $F_n=0.8$ in the case of these four hull geometries are shown in Fig. 5.48 to Fig. 5.51, respectively. From the flow visualization, the vortices are larger and stronger near the bilge area when the bilge keels are installed. As a result, in the case of the 4% bilge keel model, there is a significant increase in the amplitude of the moment history and a sizable phase shift on the results from other models. A non-linear behavior can be observed in the moment histories at every $0.4T$ and $0.9T$, especially for the 4% bilge keel model, which is due to the strong flow separation created by the bilge keel.

The effect of the bilge keel length is studied by giving four different lengths, $0\%B$ (round bilge hull with a $0.02B$ bilge radius), $2\%B$, $4\%B$ and $6\%B$. The resulting added-mass and damping coefficients, with a roll amplitude of $\alpha_o=2.87^\circ$, are presented in Fig. 5.52 and Fig. 5.53. The effects of the keel length on the hydrodynamic coefficients are similar to what has been found in Yeung et al. (2000). Both hydrodynamic coefficients increase as the bilge keel length increases. However, in our simulation, a larger difference is observed between the damping coefficients of 4% and 6% bilge keels when compared to Yeung et al. (2000).

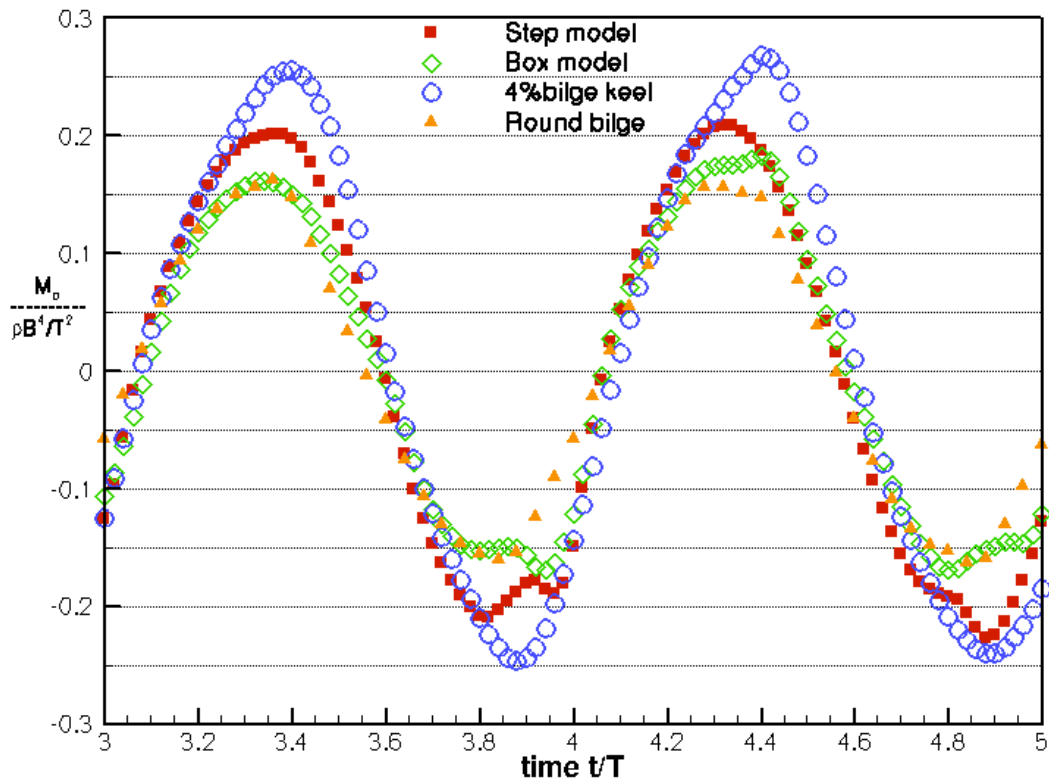


Figure 5.44: Total moment histories for different hull geometries ($F_n=1.0$ and $\alpha_o=5.75^\circ$).

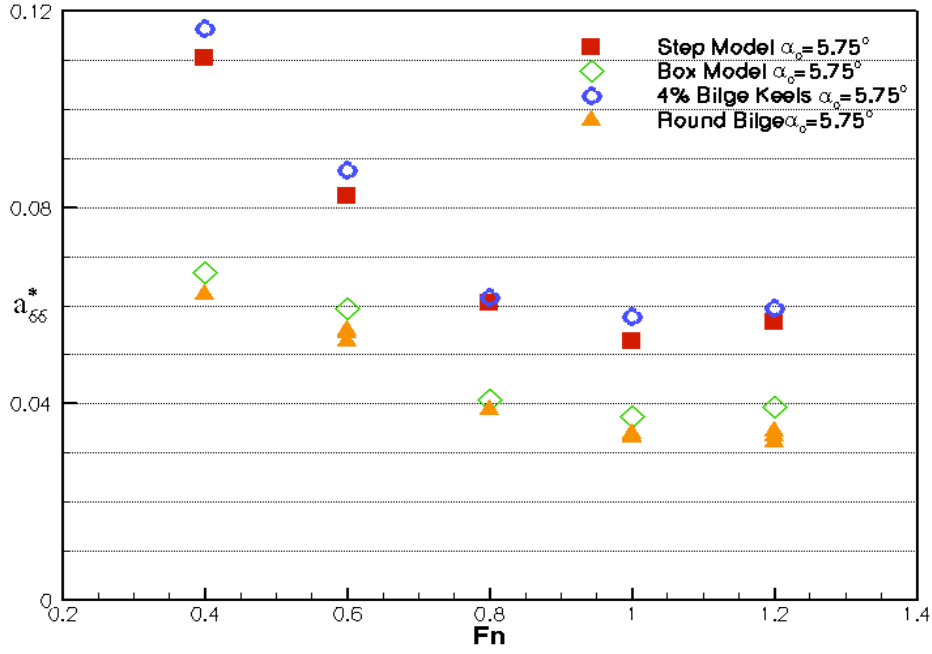


Figure 5.45: Roll added-mass coefficients for different hull geometries.

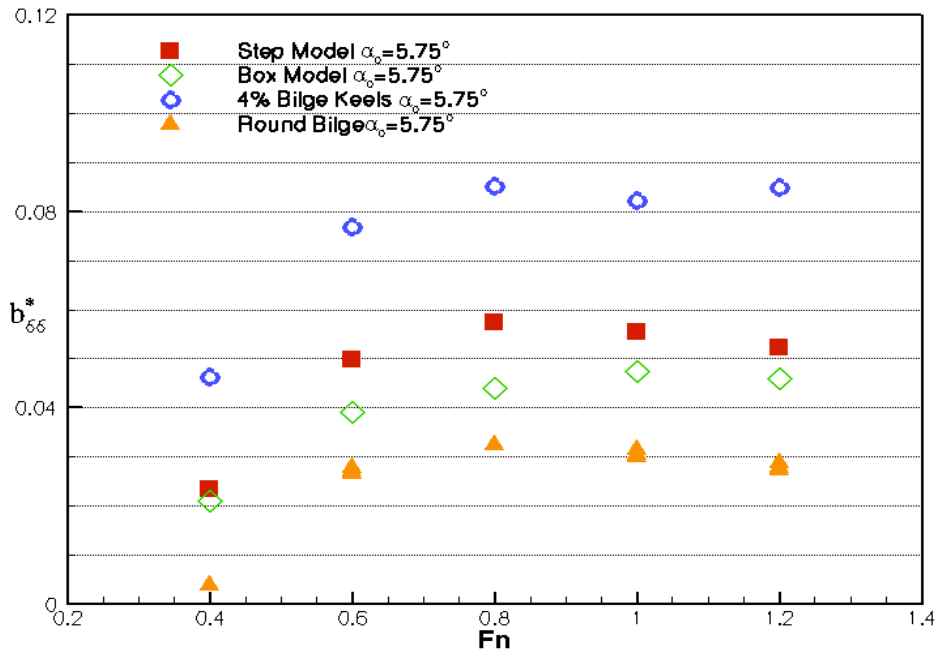
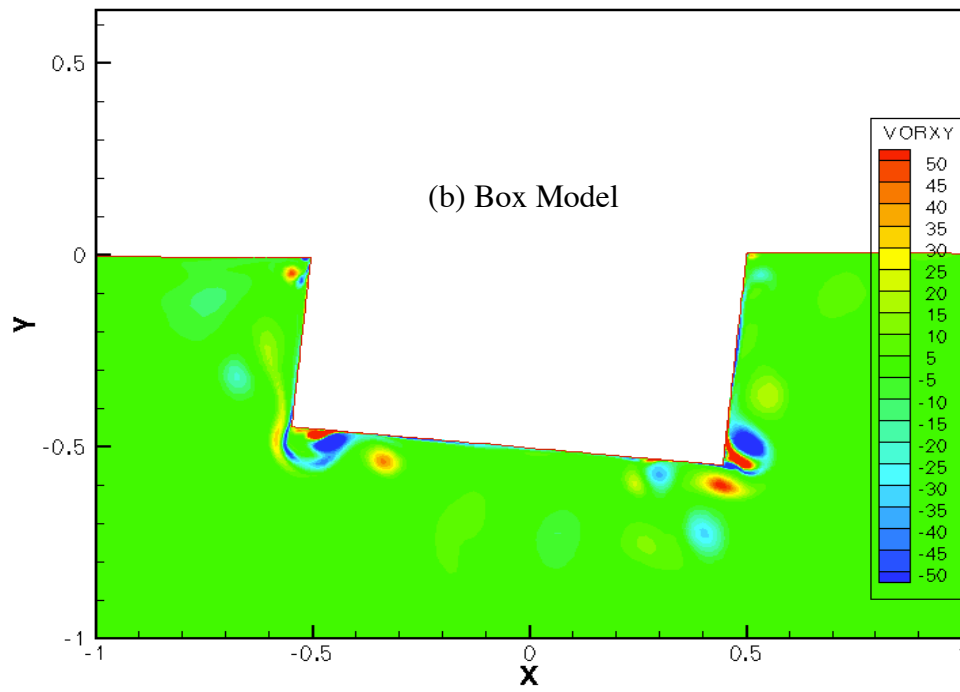
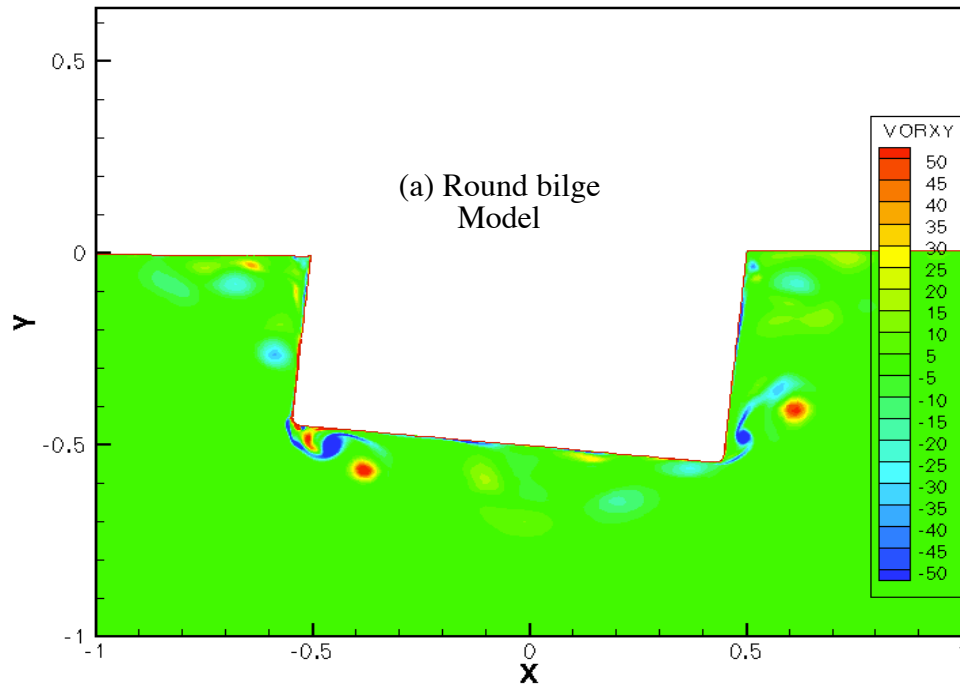


Figure 5.46: Roll damping coefficients for different hull geometries.



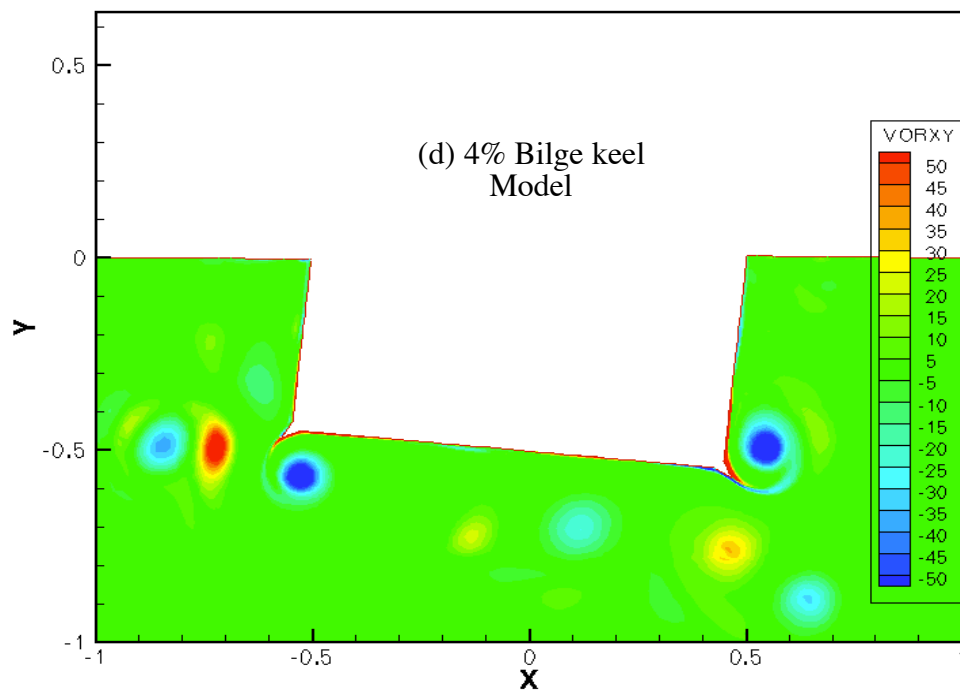
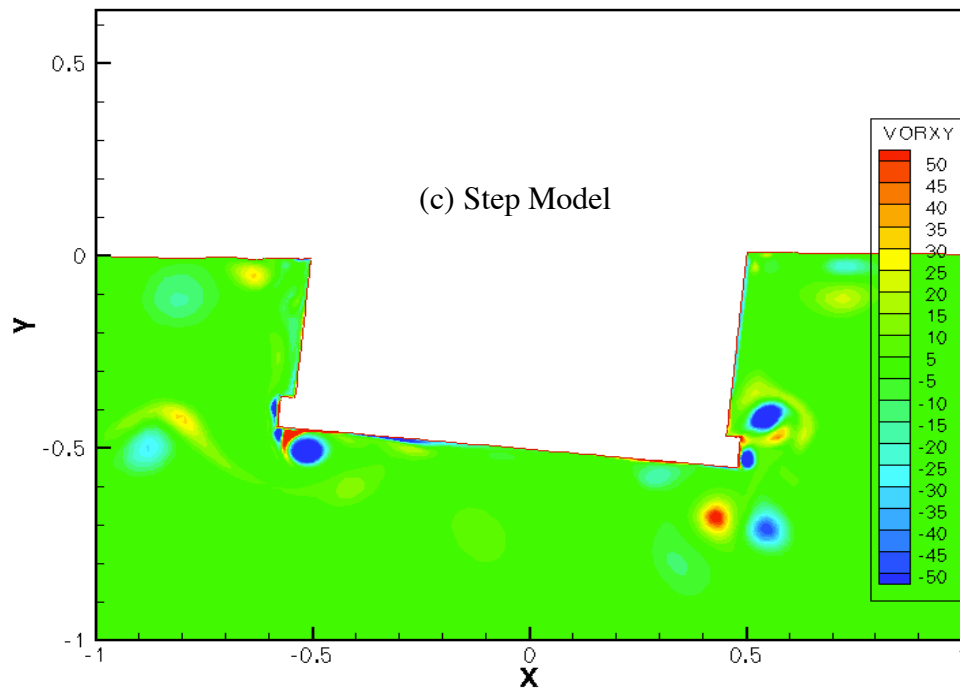


Figure 5.47: Vorticity contours ($t/T=5.75$, $Fn=1.0$ and $\alpha_0=5.75^\circ$), (a) round bilge model, (b) box model, (c) step model, (d) 4% bilge keel model.

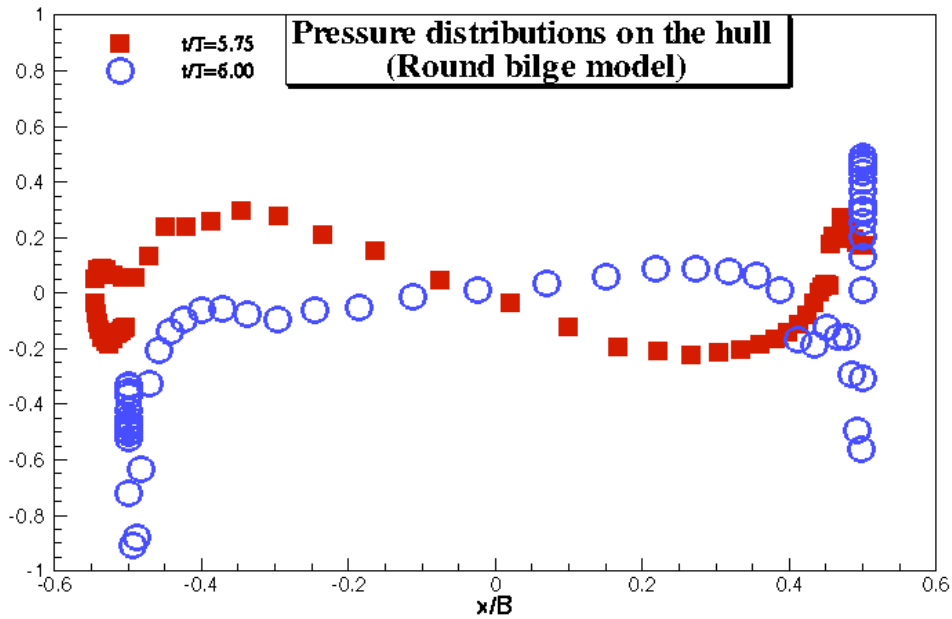


Figure 5.48: Pressure distributions on the hull (round bilge model, $F_n=0.8$ and $\alpha_0=5.75^\circ$).

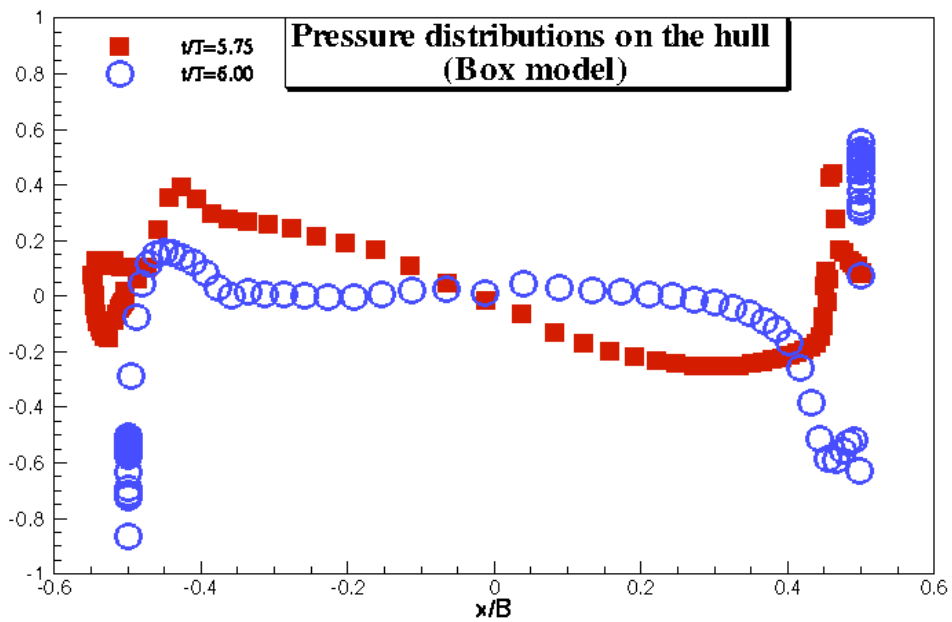


Figure 5.49: Pressure distributions on the hull (box model, $F_n=0.8$ and $\alpha_0=5.75^\circ$).

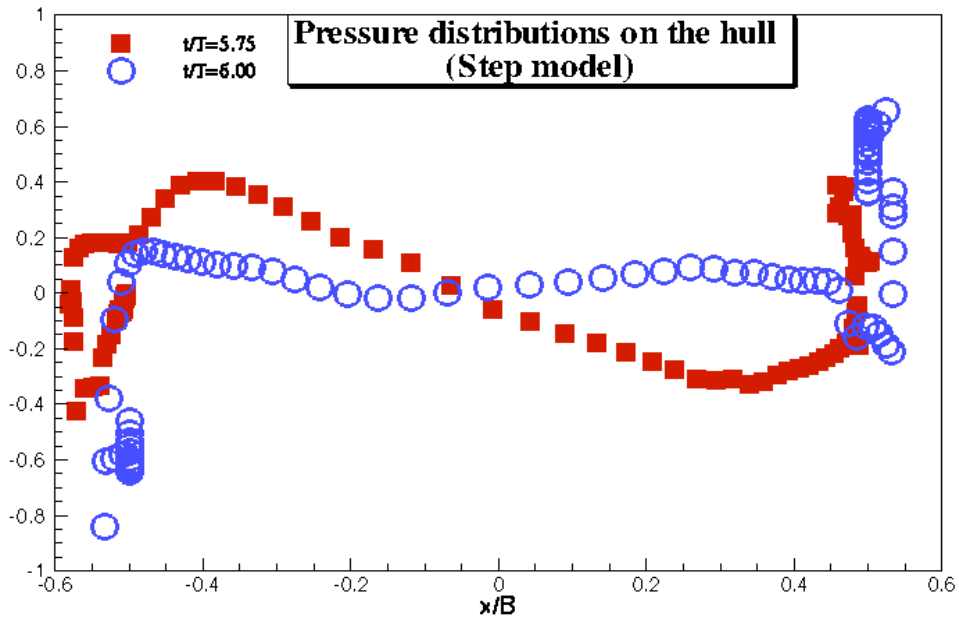


Figure 5.50: Pressure distributions on the hull (step model, $F_n=0.8$ and $\alpha_0=5.75^\circ$).

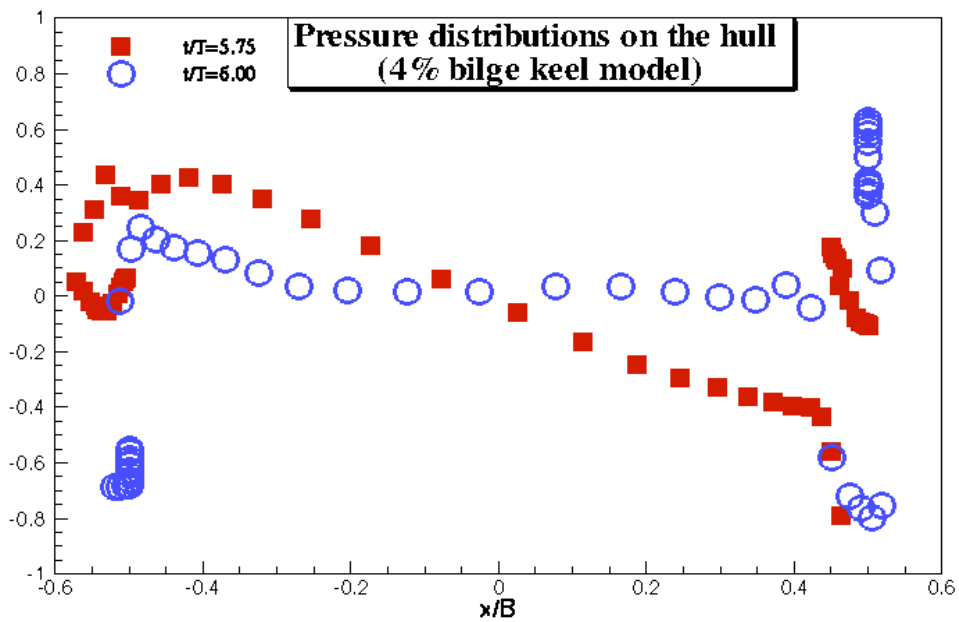


Figure 5.51: Pressure distributions on the hull (4% bilge keel model, $F_n=0.8$ and $\alpha_0=5.75^\circ$).

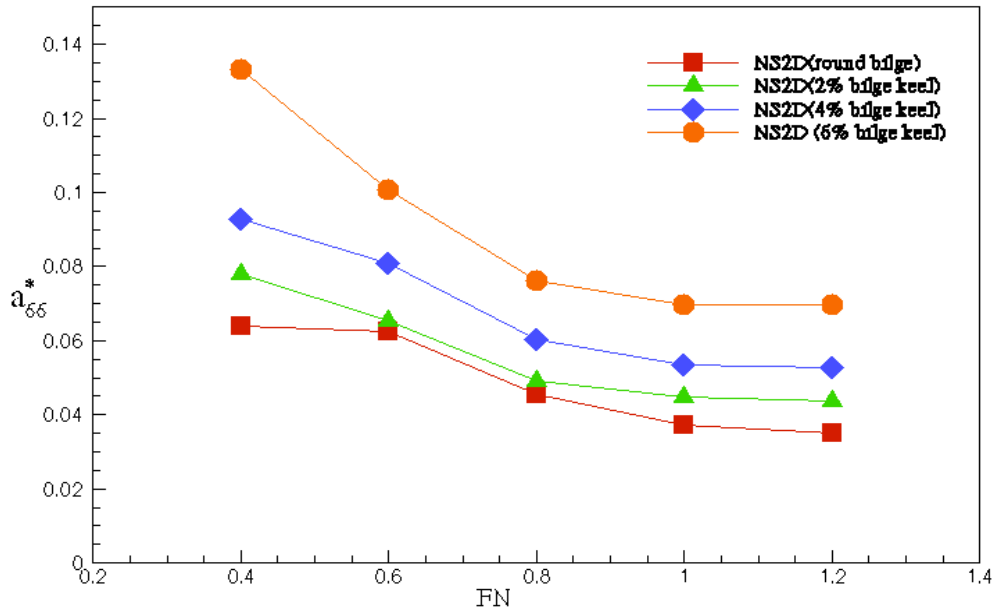


Figure 5.52: Roll added-mass coefficients for different bilge keel lengths ($\alpha_0=2.87^\circ$).

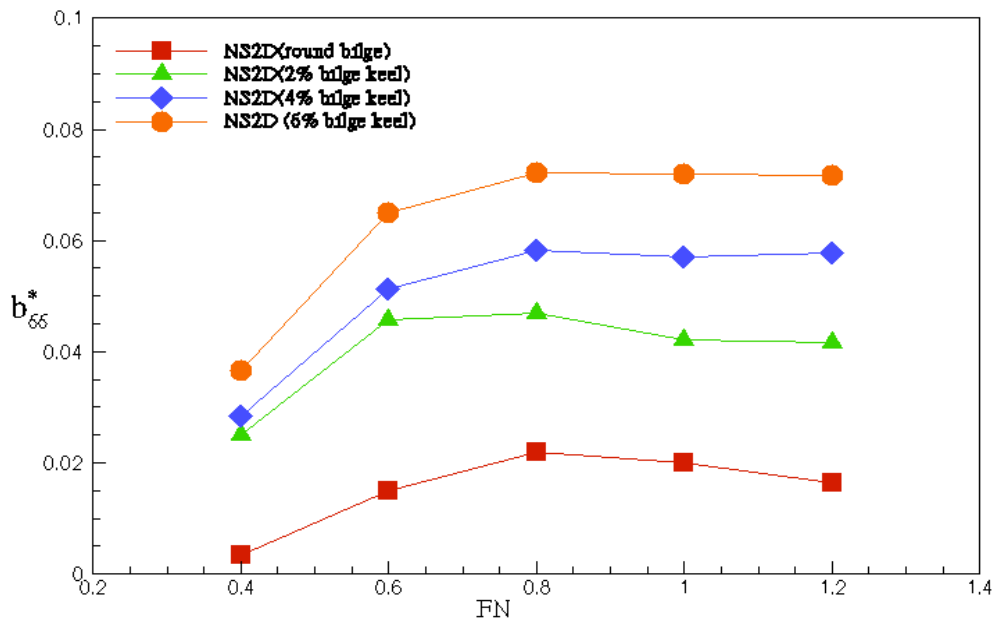


Figure 5.53: Roll damping coefficients for different bilge keel lengths ($\alpha_0=2.87^\circ$).

Comparing to the bilge keel model ($\theta=45^\circ$) in subsection 5.1.2, the horizontal and vertical bilge keels are plotted in Fig. 5.54. The added mass and damping coefficients for different Froude numbers with horizontal or vertical bilge keels are shown in Fig. 5.55. The difference between the added mass coefficients of these two cases is extremely small. On the other hand, the damping coefficients are slightly higher in the case of horizontal bilge keels when the Froude number is small. Although the bilge keel geometry is not exactly the same as those in Na et al. (2002), and Seah and Yeung (2003), a similar variation in the hydrodynamic coefficients is observed. The added-mass coefficients from both cases are almost the same as expected because both cases have the same hull displacement. On the other hand, the corresponding damping coefficients are slightly higher when the horizontal bilge keels are used. As explained in Seah and Yeung (2003), when the horizontal bilge keels are used, the shed vortices are located closer to the free surface. It affects the wave profile near the hull, and thus carries more energy away from the hull. As a result, the horizontal bilge keel creates a larger damping coefficient as compared to the vertical one. Moreover, the viscous effects become weaker when the Froude number increases. Therefore, the deviation in the damping coefficients between the two cases is negligible when the Froude number becomes larger.

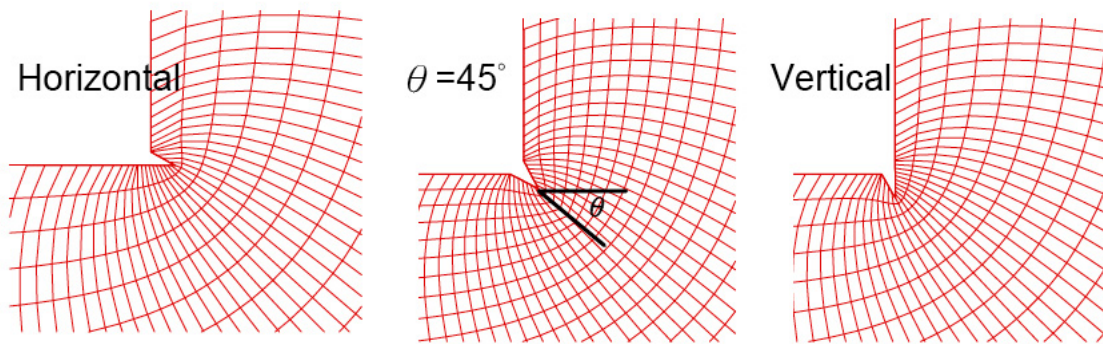


Figure 5.54: The geometries for different types of bilge keels.

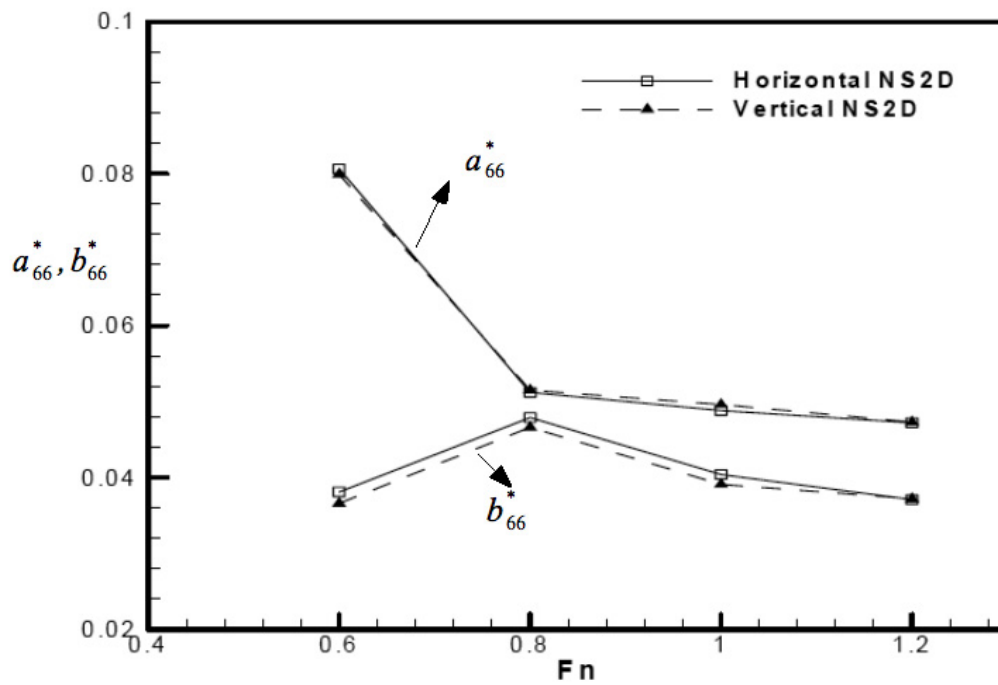


Figure 5.55: Roll added-mass and damping coefficients for horizontal and vertical bilge keels ($\alpha_0=2.87^\circ$).

5.2 DECAY MOTIONS

This section describes the background of the free-decay motions and the calculations of the motion response. The results of the heave decay motion from the NS2D simulation are compared to those from other methods. Also presented in this section are the results of roll decay motions for different hull geometries and various initial roll angles.

5.2.1 Background

The horizontal sway motion is constrained in the present decay motion problem, and the angular acceleration and the vertical acceleration \ddot{y}_b are calculated based on the Newton's second law for the equilibrium:

$$\begin{aligned} F_y - m_b g &= m_b (y_b - y_g \dot{\alpha}^2), \\ M_o - m_b g x_g &= I_o \ddot{\alpha} + m_b x_g \ddot{y}_b, \end{aligned} \tag{5.7}$$

where I_o is the mass-moment of inertia about the center of rotation, $\dot{\alpha}$ stands for the angular velocity, m_b is the mass of the body, x_g and y_g represent horizontal and vertical components of \overline{OG} and y_b indicates the vertical hull movement. In order to simplify the studies, the decay tests are carried out individually by allowing only a single degree of freedom, i.e. either heave or roll. Therefore, the equations of motions can be further modified, where the angular velocity term in the heave motion and the vertical acceleration term in the roll motion are dropped out from the equations of motions, which are given as:

$$\begin{aligned}
 F_y - m_b g &= m_b y_b, \\
 M_o - m_b g x_g &= I_o \ddot{\alpha}.
 \end{aligned}
 \tag{5.8}$$

Note that by using Eq. (5.1), the forces and moments on the hull are evaluated by integrating the pressures on the wetted portion of the body surface. The corresponding vertical hull movement and roll angle are calculated using a time marching scheme similar to the one used for solving the Navier-Stokes equations.

According to Roddier (2000), the center of gravity is located $0.144B$ below the origin O , as shown in Fig. 5.56, and the radius gyration about O is equal to $0.394B$. Figure 5.57 illustrates the heave or roll decay motion of a hull and its mean position. All the variables are made non-dimensional with respect to the hull beam and $\sqrt{B/g}$, and the corresponding Reynolds number is equal to 5.27×10^5 .

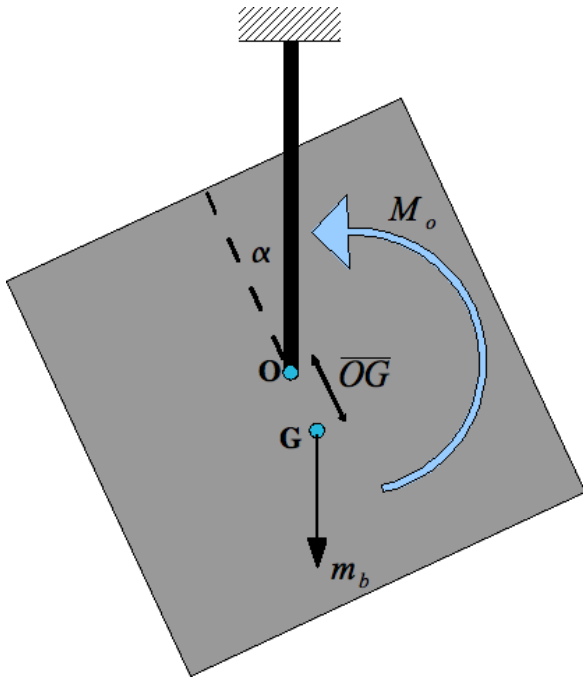


Figure 5.56: Center of gravity in roll decay.

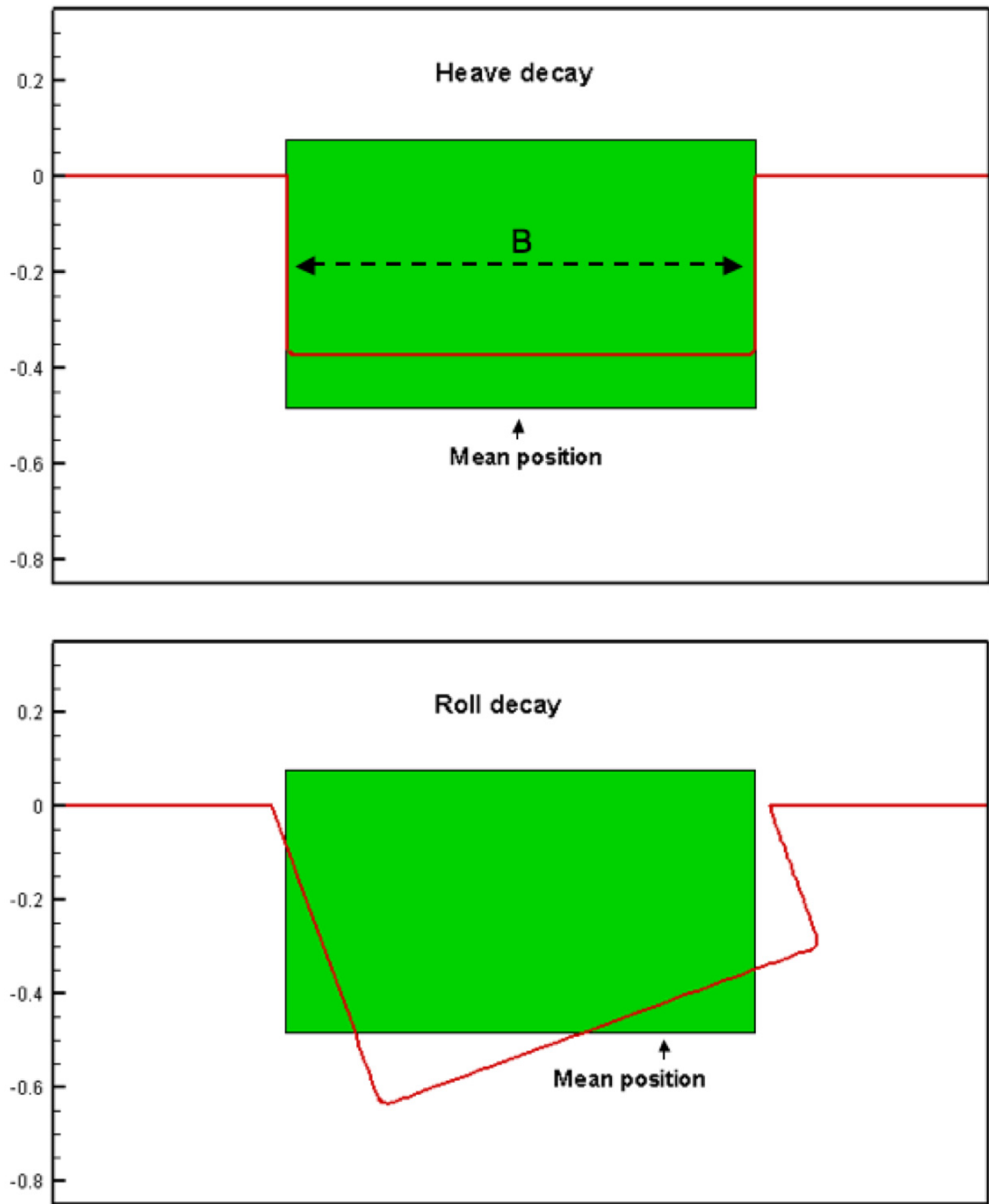


Figure 5.57: The heave or decay motion of a hull and its mean position.

Based on the dynamic theory and the assumption that the motion is damped linearly, the nominal roll period T_D is equal to

$$T_D = 2\pi \sqrt{\frac{I_o + a_{66}}{\rho g \nabla H_{GM}}}, \quad (5.9)$$

where H_{GM} denotes the roll metacentric height. Note that the roll decay response in the present study is calculated following Eq. (5.7) and it is coupled in the numerical simulation. Eq. (5.9) is given as a reference to explain the relation between roll decay period and the added-mass coefficient.

5.2.2 Results

In the heave decay problem, an initial displacement at $t=0$ is given as $y_0 = 0.125B$. Figure 5.58 plots the heave motion responses predicted from NS2D, and from the experimental measurements and the numerical modeling of Roddier (2000). The NS2D result agrees well with those from Roddier (2000). Figure 5.59 shows the logarithmic difference of successive peaks in the heave decay motion. Theoretically, it should be a constant versus time by following an exponential law. The logarithmic difference of successive peaks has been recovered perfectly using present numerical scheme, NS2D(IN) and NS2D(VS), and the BEM based potential flow solver, NL-BEM. In fact, the numerical prediction from the present scheme has shown a better agreement with the experimental data from Roddier (2000) as compared to his numerical solutions.

In the roll decay problem, an initial roll angle at $t=0$ is specified. The hull geometry is exactly the same as those used in the prescribed roll problem. Figure 5.60 shows the roll angle response for different hull geometries with initial displacement of

$\alpha_0=14.32^\circ$, and the inviscid flow result for the round bilge model is also presented in the figure. The roll response decreases faster in viscous flow in comparison to inviscid flow, but the roll decay periods are found to be about the same. The responses for different initial displacements of roll angle ($\alpha_0=10^\circ, 14.32^\circ, 20^\circ$) are presented in Fig. 5.61. The vorticity contours for all the analyzed hull geometries and their hull position are shown in Fig. 5.62 to Fig. 5.65, where the top figures illustrate the initial solution, and the bottom figures show the result at the end of first roll decay period. Note that the roll decay frequency varies with different hull geometries. Therefore, those bottom figures in Fig. 5.62 to Fig. 5.65 are plotted at different time. It has been found that the 4% bilge keel model is the most effective model in terms of damping the roll motion, where the roll response amplitude of the 4% bilge keel model decays faster than those of all the other analyzed geometries. Also, it has the longest roll decay period. On the other hand, the round bilge model is the least efficient as expected. In the study of different initial roll angles, larger initial roll angle tends to have a higher decay rate in terms of scaled roll response amplitude but a shorter roll decay period. This can be explained by using the corresponding hydrodynamic coefficients found in the prescribed roll motion problem. The amplitude of the normalized roll angle decays faster when the damping coefficient is higher. By following Eq. (5.9), the roll decay period is proportional to the square root of I_o+a_{66} . Therefore, the period increases when the added-mass coefficient becomes larger.

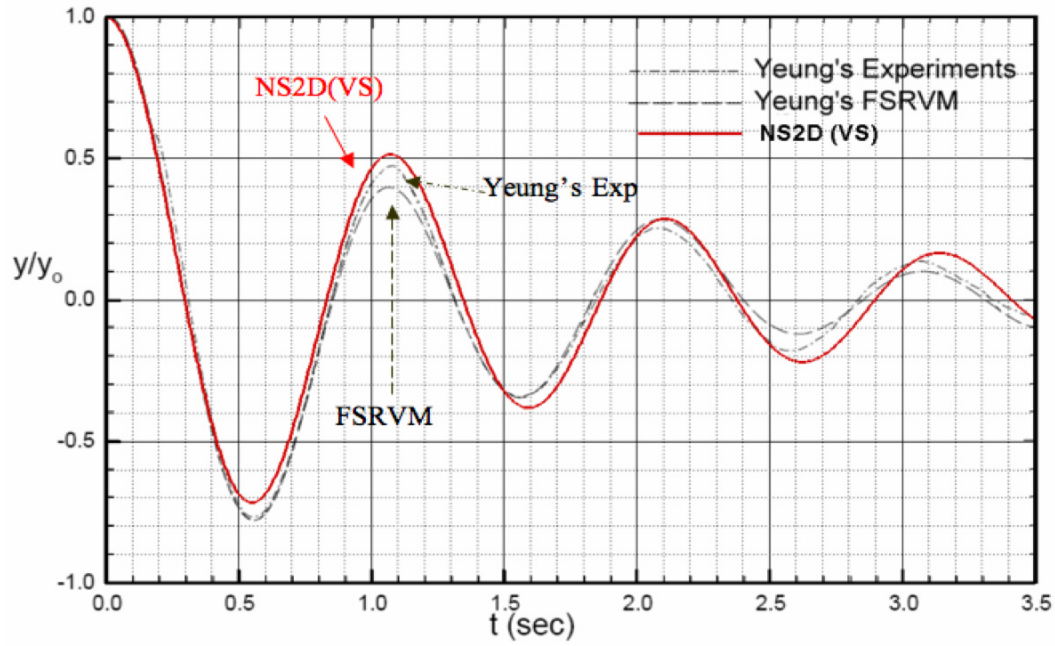


Figure 5.58: Heave motions responses from NS2D and other methods (round bilge hull and $y_0=0.125B$).

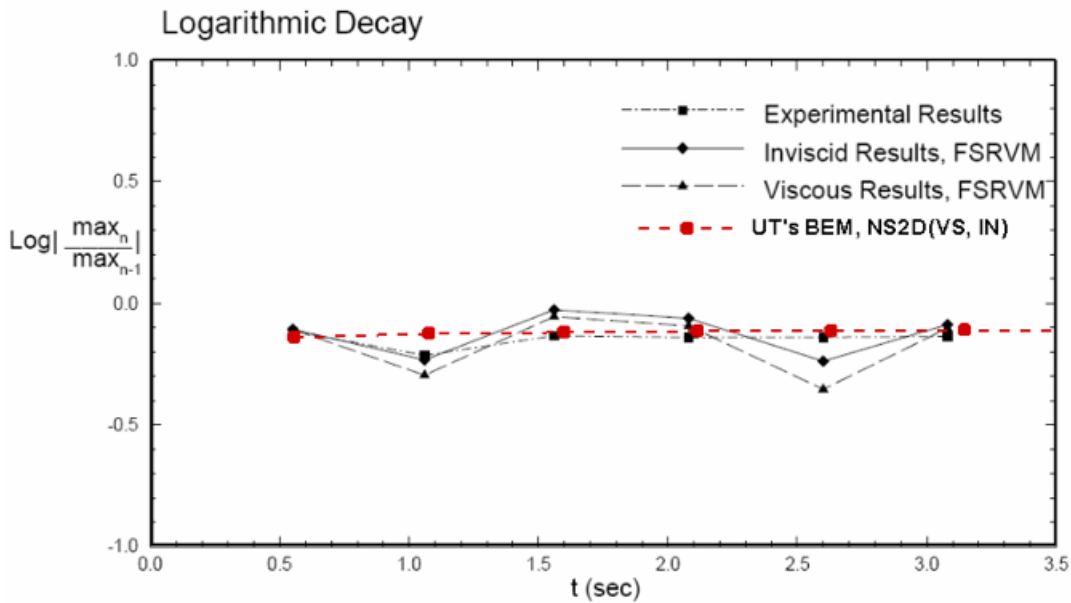


Figure 5.59: Logarithmic decay of the heave motions from NS2D and other methods (round bilge hull and $y_0=0.125B$).

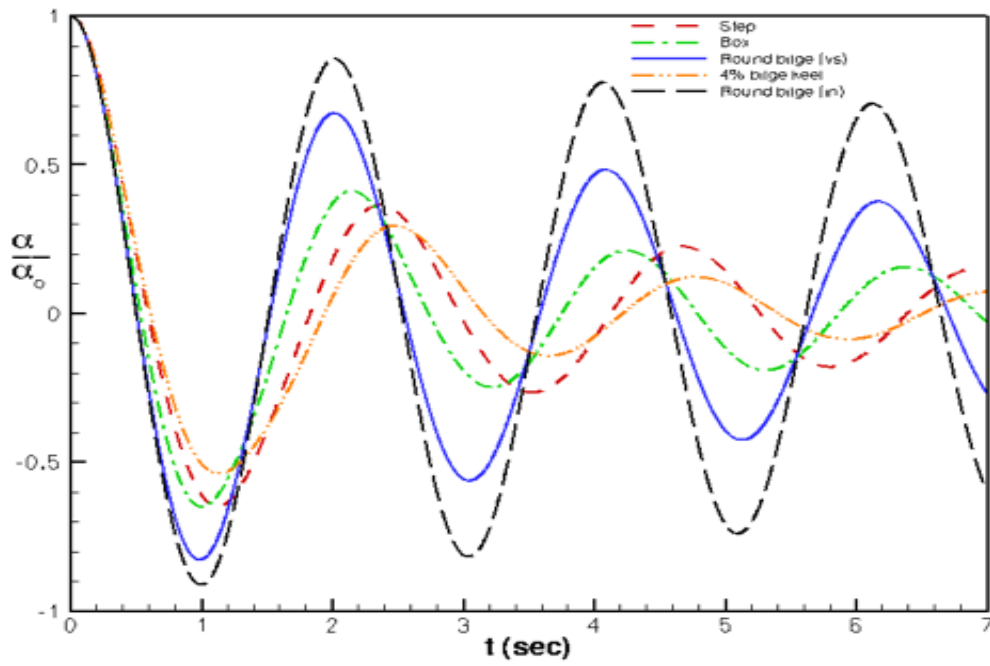


Figure 5.60: Roll response for different hull geometries ($\alpha_0=14.32^\circ$).

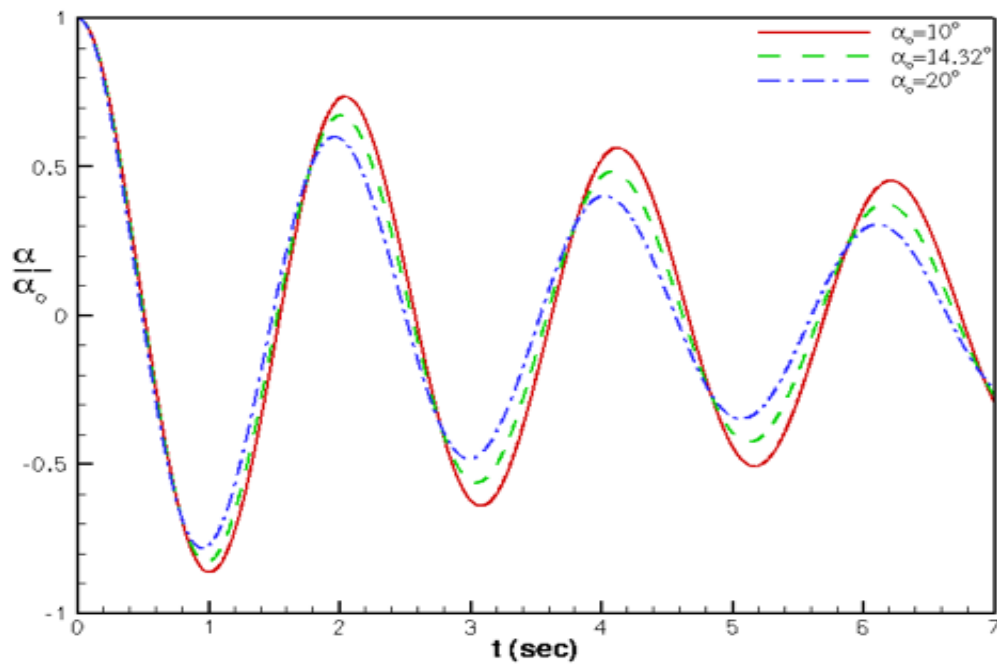


Figure 5.61: Roll response for different initial roll displacements (round bilge hull).

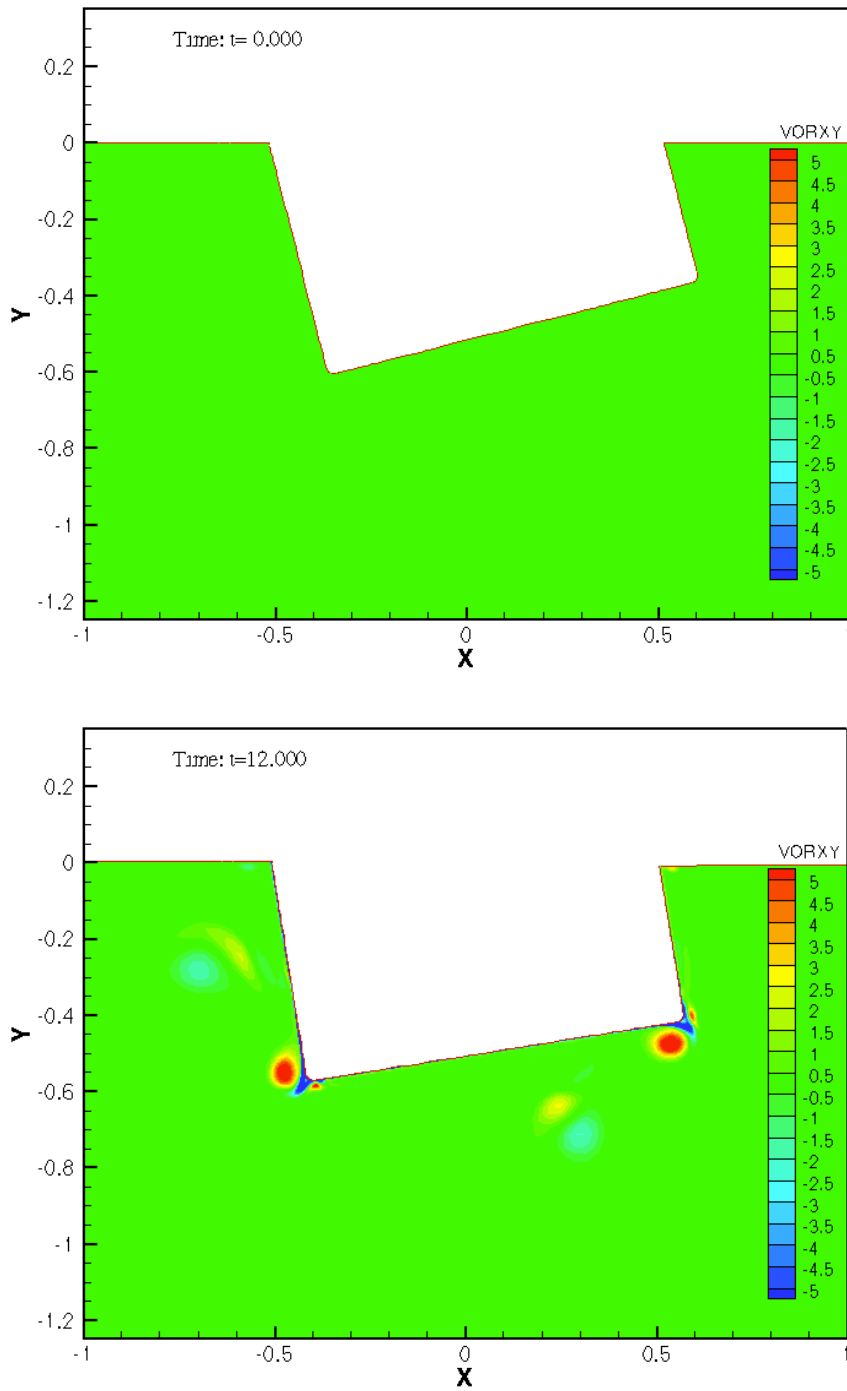


Figure 5.62: Vorticity contours and the corresponding hull positions for round bilge model at $t^* = t/\sqrt{B/g} = 0$ and $t^* = t/\sqrt{B/g} = 12$ ($\alpha_0 = 14.32^\circ$).

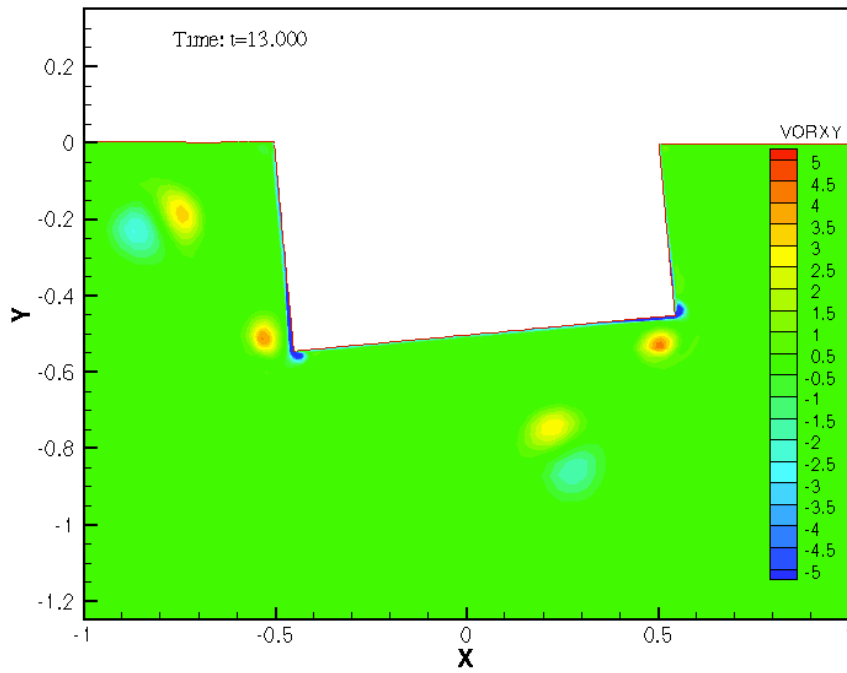
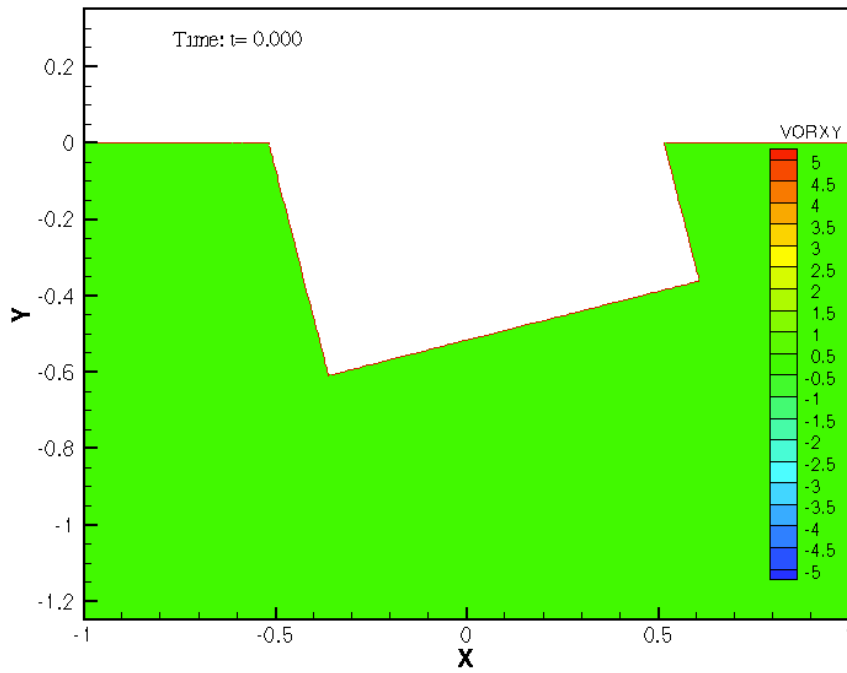


Figure 5.63: Vorticity contours and the corresponding hull positions for box model at $t^* = t/\sqrt{B/g} = 0$ and $t^* = t/\sqrt{B/g} = 13$ ($\alpha_0 = 14.32^\circ$).

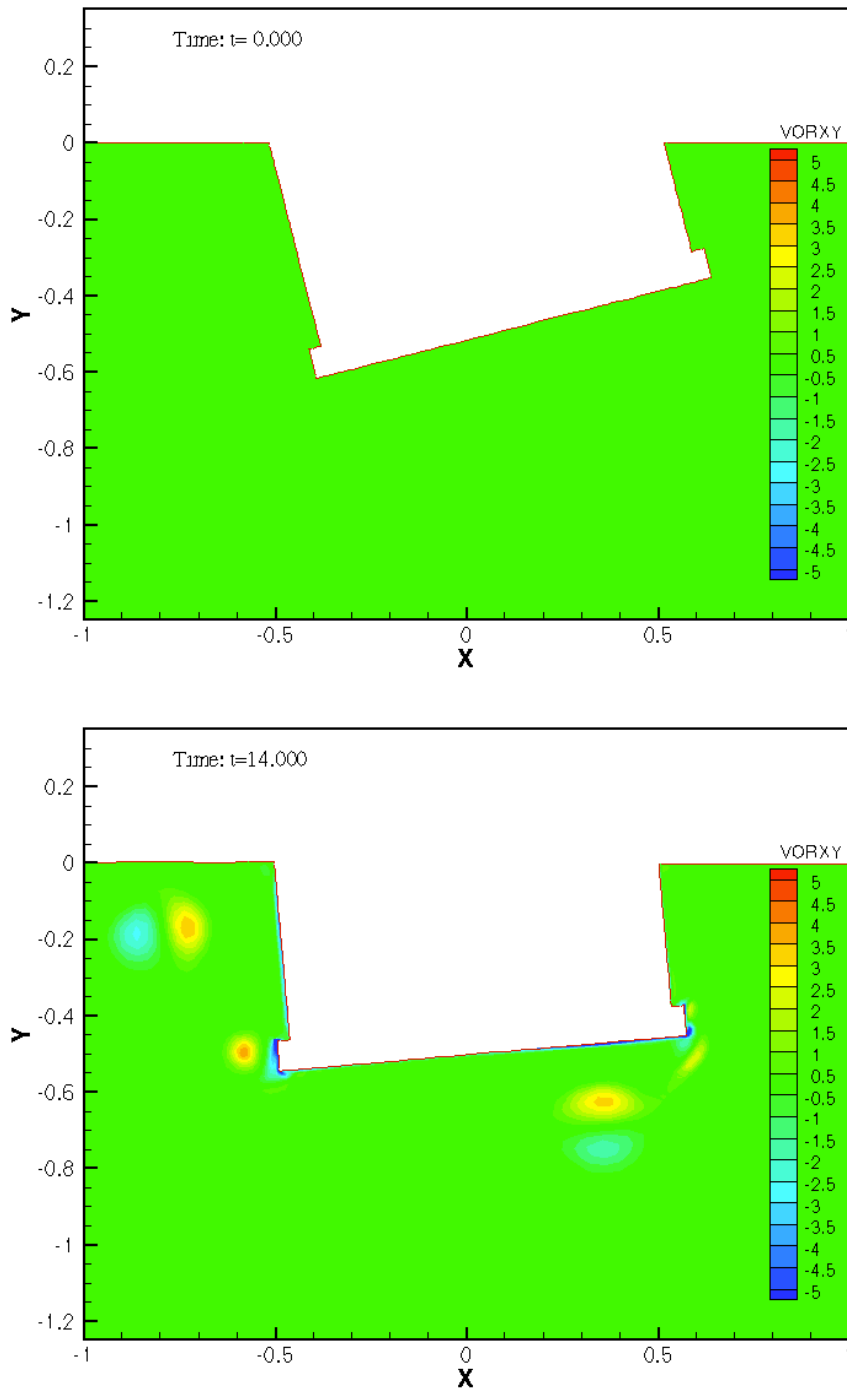


Figure 5.64: Vorticity contours and the corresponding hull positions for step model at $t^* = t/\sqrt{B/g} = 0$ and $t^* = t/\sqrt{B/g} = 14$ ($\alpha_0 = 14.32^\circ$).

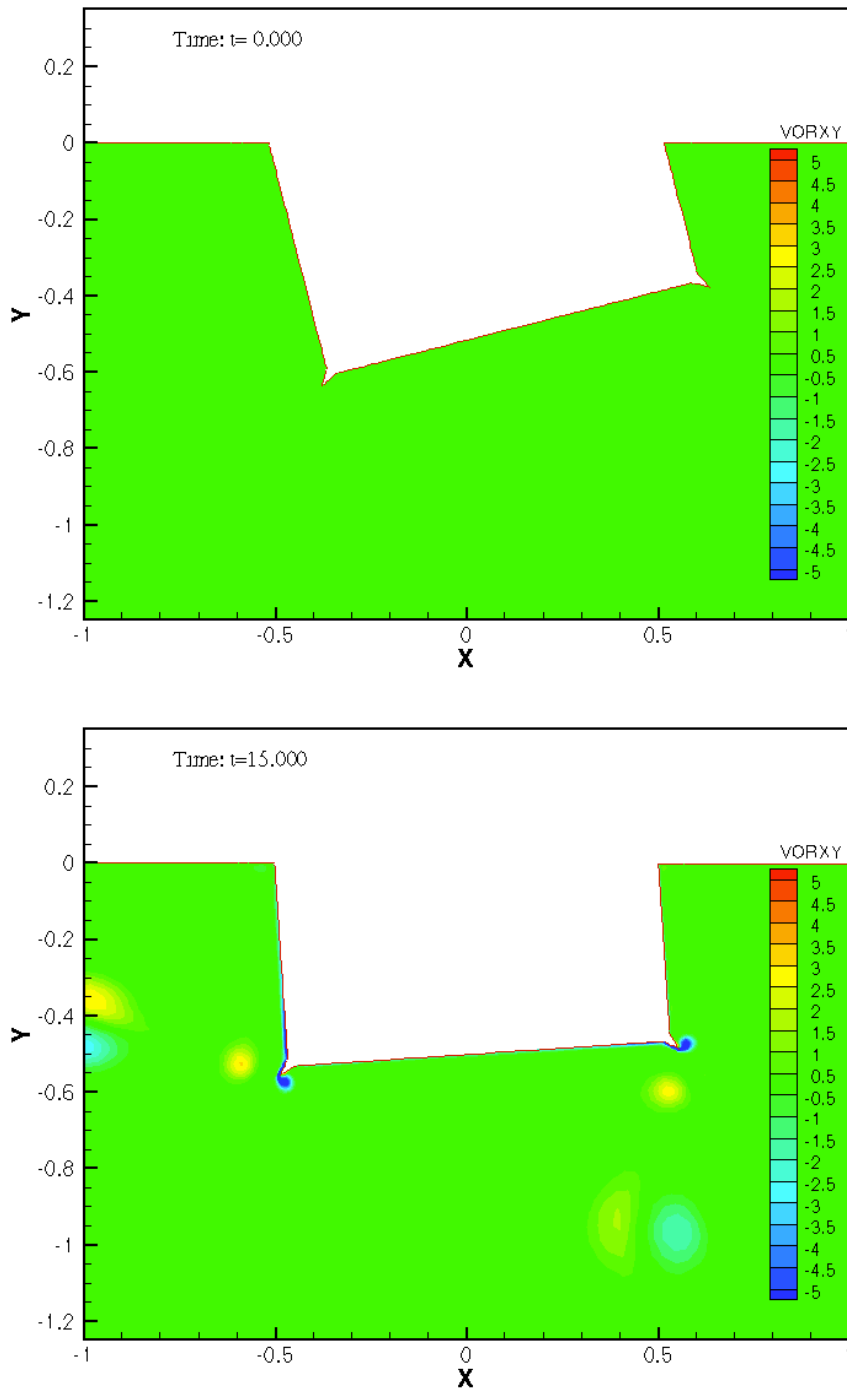


Figure 5.65: Vorticity contours and the corresponding hull positions for 4% bilge keel model at $t^* = t/\sqrt{B/g} = 0$ and $t^* = t/\sqrt{B/g} = 15$ ($\alpha_0 = 14.32^\circ$).

5.3 SUMMARY

A two-dimensional Navier-Stokes based solver has been applied to model the separated flow for different hull geometries subject to prescribed roll motions or in free-decay motions. Sensitivity analyses in space and in time were performed, and the results for various hull geometries from the present numerical scheme compare well with those from FLUENT and other methods. The effect of turbulence is found to be very small in the ship-shaped hull roll motion problem. The current model can handle roll angles up to 20 degrees. The non-linear effects were observed in small as well as large amplitudes of roll, which make using a linear combination of added-mass and damping coefficients to represent the corresponding hydrodynamic loads inadequate. Therefore, the calculation of the hull response in the time domain becomes inevitable. Among all the analyzed geometries, the bilge keel model (at least longer than $4\%B$) was found to be the most effective model for mitigating roll motions, and to have the lowest roll damping frequency.

The present numerical scheme has been successfully applied to several 2D ship-shaped hull roll motion problems, and the results agree well with other methods. Thus, the present 2D solver is extended into three dimensions, and it will be applied to 3D problems in the next chapter.

Chapter 6: Three-Dimensional Results

The verification and the validation of the three-dimensional Navier-Stokes (NS3D) solver are discussed in this chapter. The NS3D solver is applied in this chapter to the piston type wave-maker problem and the prescribed roll motion problems of a uniform or a non-uniform cross-section cylindrical hull. In the first two cases, the results from NS3D are validated with those from NS2D. In the last case, the NS3D results are compared to those from the 2D approach using strip theory.

6.1 PISTON TYPE WAVE-MAKER

The inviscid version of the NS3D solver is applied to the 3D piston type wave-maker problem, which is extended from the 2D wave-maker problem described in section 4.4. The computational domain and the corresponding domain boundaries are shown in Fig. 6.1. In this study, the grid and domain configurations in x - y plane are identical to the 2D case. The wave channel is h_d wide and has a uniform cross-section. Five strips of hexahedral cells are used, which give a total number of 32,000 cells for the entire 3D computational domain. Two additional slip-wall boundaries are used as the sidewalls and are placed at $z=0$ and $z=h_d$. All the variables are made non-dimensional with exactly the same parameters used in 2D case. Therefore, the piston wave-maker also moves periodically with a frequency of $(\pi/2)\sqrt{g/h_d}$, a wave height of $A=0.05h_d$, and a time step size of $\Delta t / \sqrt{h_d/g} = 0.1$. Figure 6.2 shows three slices of the pressure contours for x - y plane, and each pressure contour is identical to the other. The 3D free-surface elevation is presented in Fig. 6.3. Figure 6.4 shows the comparison of the free-surface elevation among the results from NS2D and NS3D, and the one predicted by Lin (1984). As expected, the 3D free-surface elevation is identical to the one solved in the 2D case.

The results show that the NS3D solver is well validated in this case, and a study on the prescribed roll motion of a 3D hull with a uniform hull cross-section will be presented in the next section.

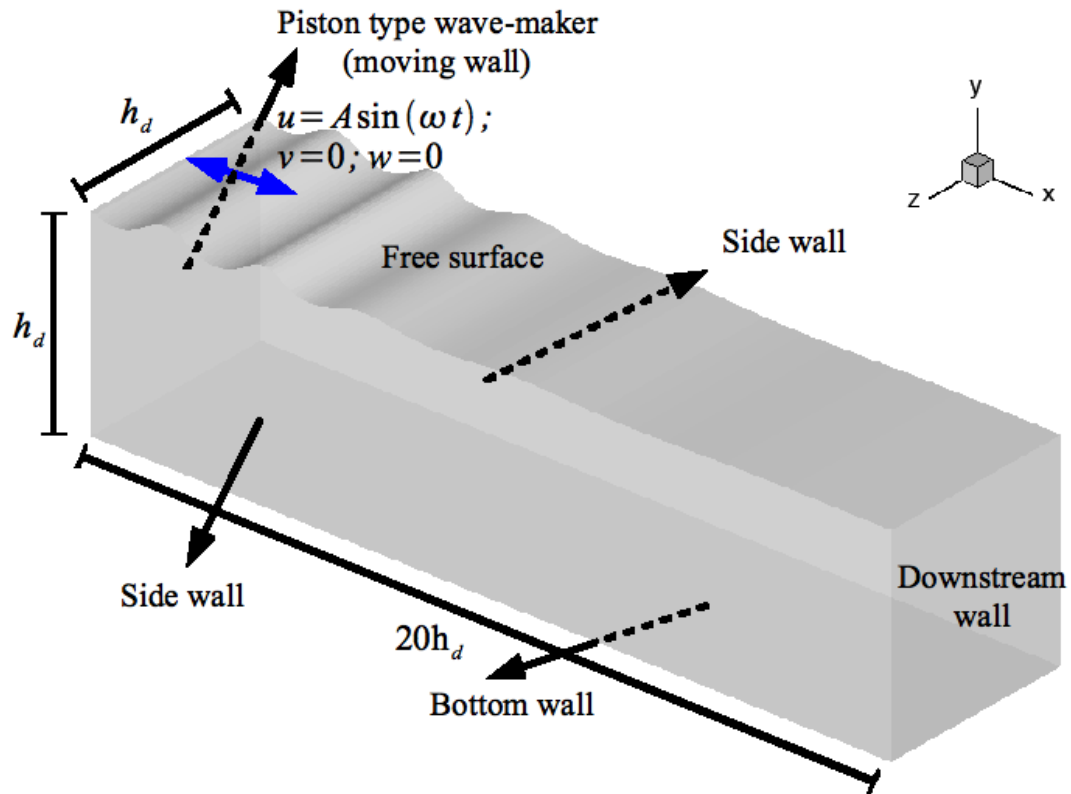


Figure 6.1: Computational domain and corresponding domain boundaries of a 3D piston type wave-maker problem.

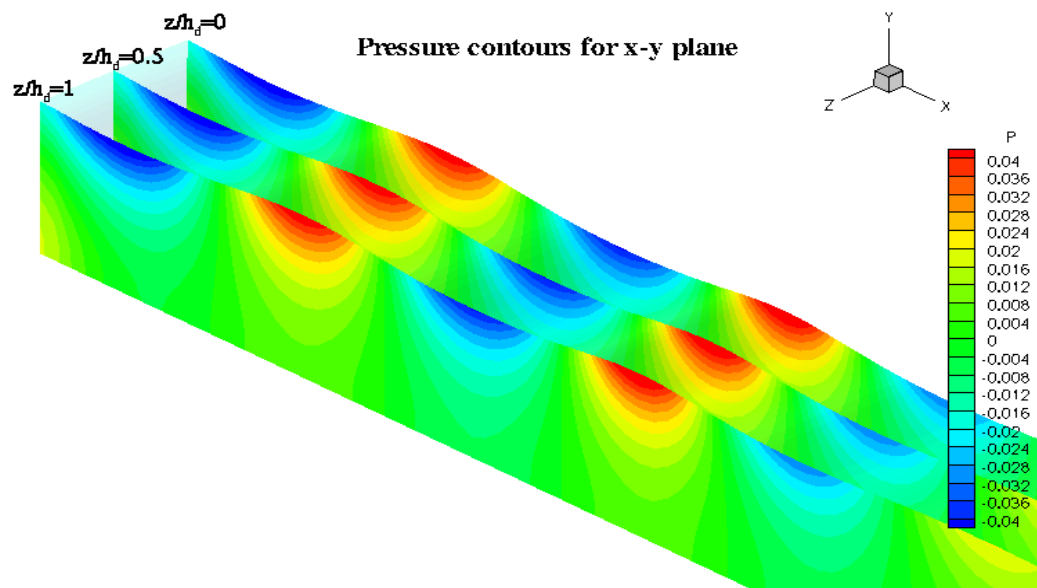


Figure 6.2: Three slices of the pressure contours for x-y plane at $t / \sqrt{h_d / g} = 20$.

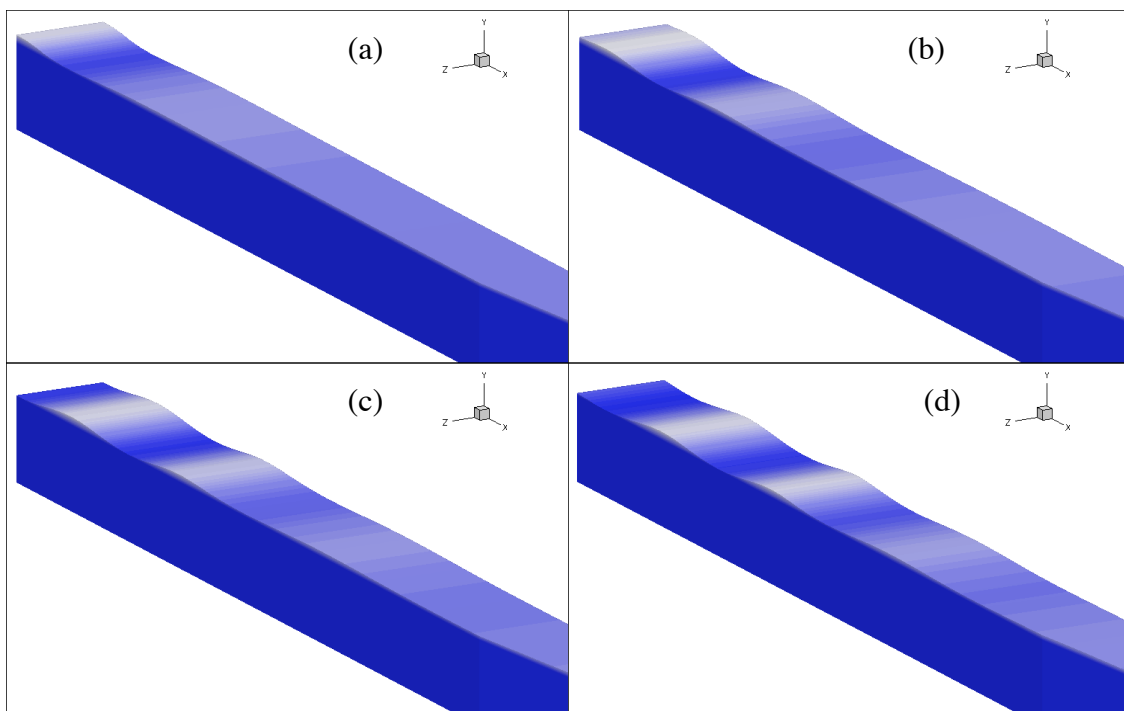


Figure 6.3: 3D free-surface elevation at (a) $t / \sqrt{h_d / g} = 5.0$, (b) $t / \sqrt{h_d / g} = 10.0$, (c) $t / \sqrt{h_d / g} = 15.0$ and (d) $t / \sqrt{h_d / g} = 20.0$.

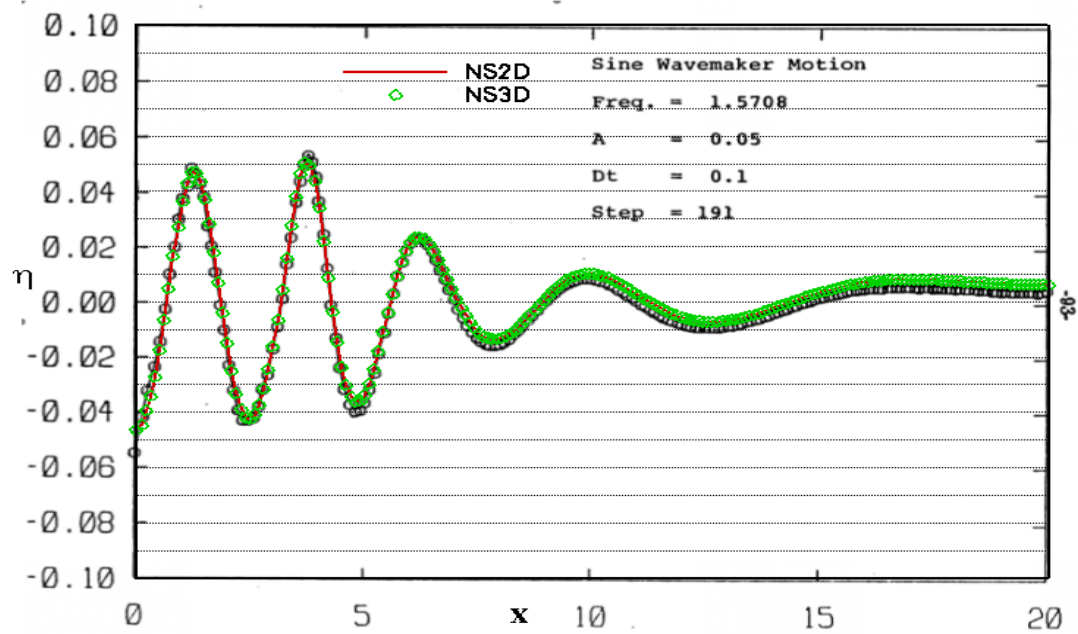


Figure 6.4: Free-surface elevation from NS3D, NS2D and Lin (1984) at

$$t / \sqrt{h_d / g} = 19.1.$$

6.2 PRESCRIBED ROLL OF A SHIP-SHAPED HULL WITH A UNIFORM HULL CROSS-SECTION

In this section, the NS3D solver is applied to a 3D prescribed roll motion problem, which is extended from the 2D case described in section 5.1, and all the variables are also made non-dimensional with exactly the same parameters as used in the 2D case. As shown in Fig. 6.5, the numerical simulation is performed in a uniform channel with a domain size of $40B$ ($20B$ on each side of the hull) long, $3B$ wide and $6.67B$ deep, and the ship-shaped hull also has a uniform cross-section, which is identical to the round bilge hull geometry as used in the 2D case. The 3D mesh is shown in Fig. 6.6. It contains six strips of hexahedral cells and a total number of 34,224 cells for the entire 3D computational domain.

The ship-shaped hull is forced to roll at a fixed Froude number, $Fn=0.8$, and the roll amplitude is equal to 5.75 degrees. The vorticity contour and the vorticity iso-surface at $t/T=6.00$ are presented in Fig. 6.7. Three slices of pressure contours for x - y plane at $t/T=6.00$ are shown in Fig. 6.8. The results clearly show two-dimensionality in the longitudinal direction of the hull (z -direction). Moreover, the pressure distribution along the hull predicted by using NS3D is compared to the solution of the 2D case at $t/T=5.75$ and 6.00. As shown in Fig. 6.9, the 3D results are identical to those solved in two dimensions.

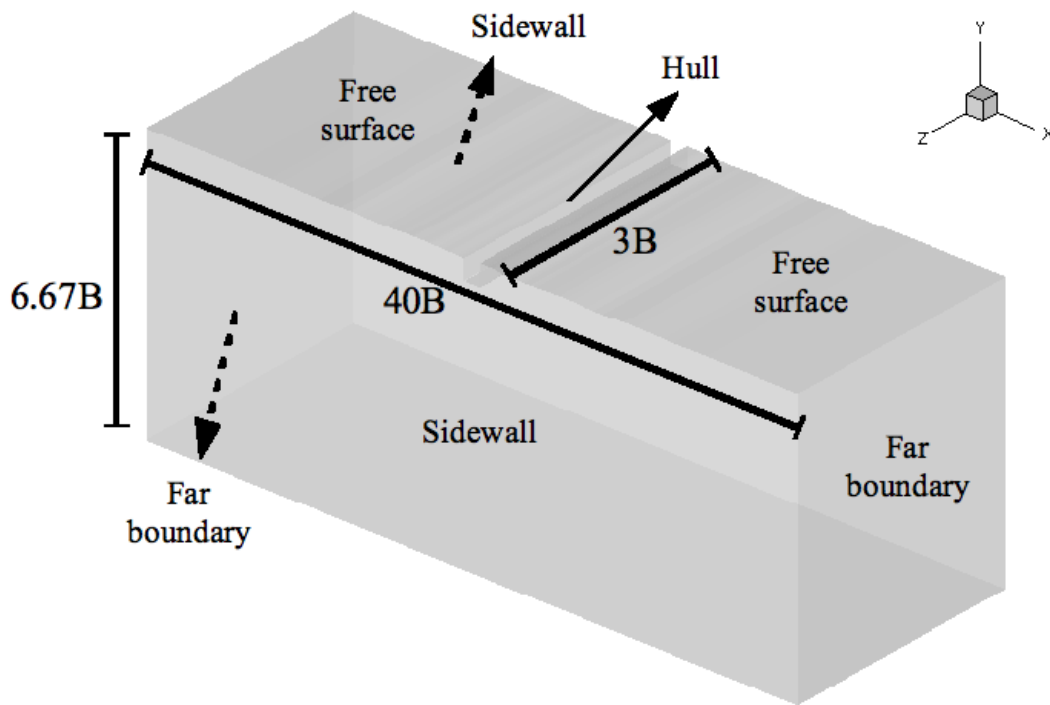


Figure 6.5: Computational domain and corresponding domain boundaries of a 3D prescribed roll motion problem in a uniform channel with a uniform hull cross-section.

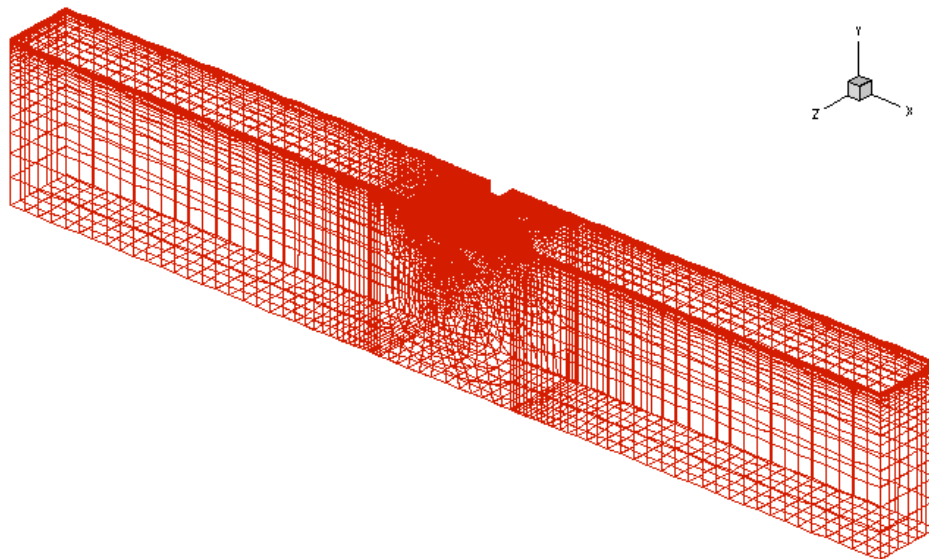


Figure 6.6: Mesh of the 3D prescribed roll motion problem in a uniform channel with a uniform hull cross-section.

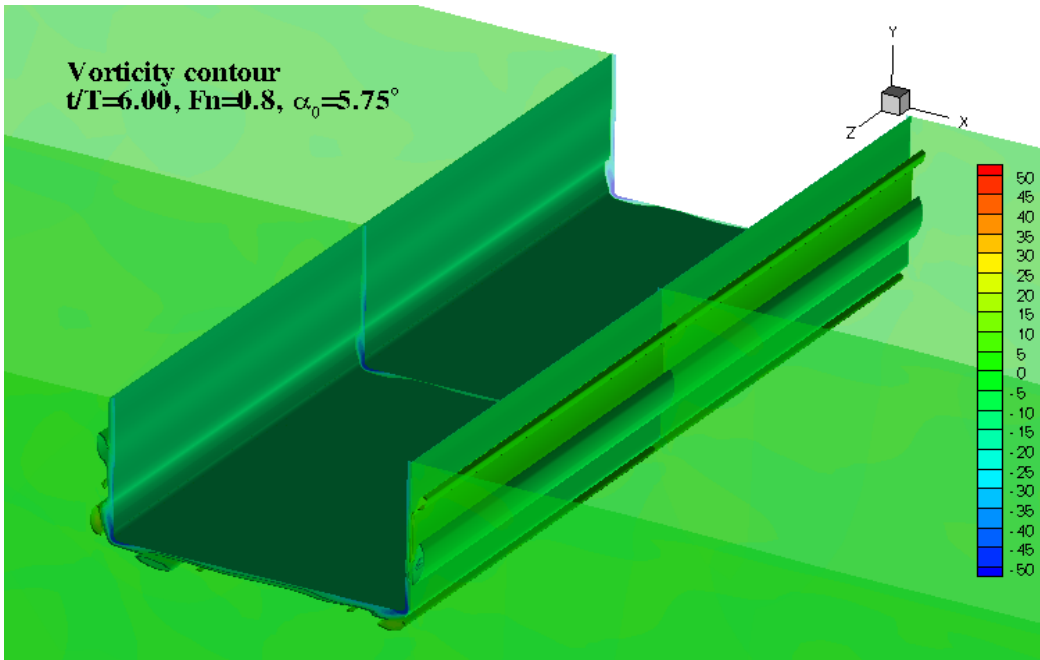


Figure 6.7: The vorticity contour and the vorticity iso-surface of the 3D prescribed roll motion problem in a uniform channel with a uniform hull cross-section.

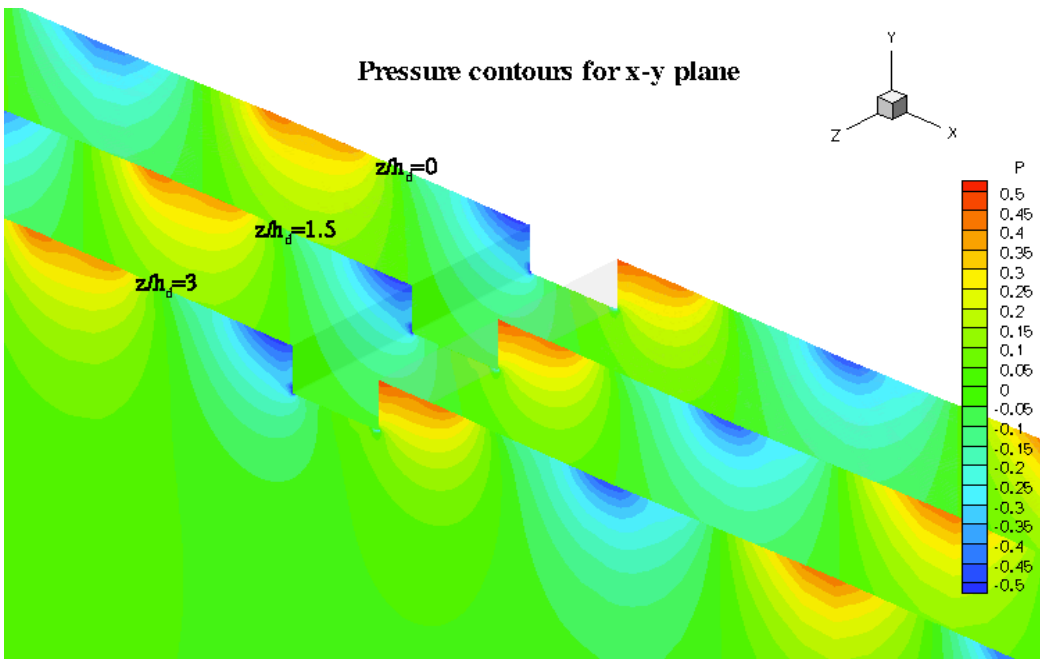


Figure 6.8: Slices of pressure contours for x - y plane in the case of the 3D prescribed roll motion problem in a uniform channel with a uniform hull cross-section.

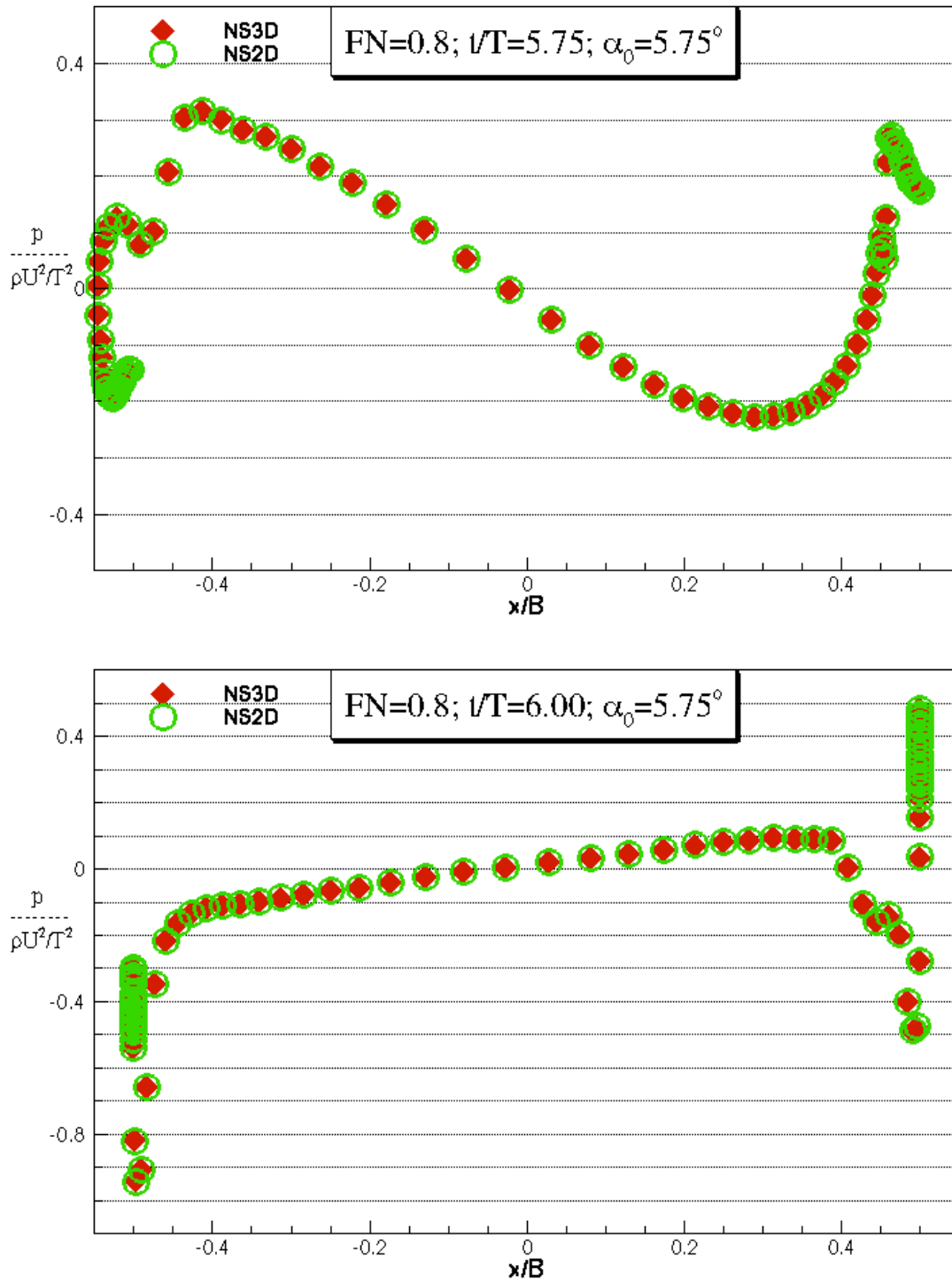


Figure 6.9: Comparison between the pressure distribution from NS2D and NS3D.

6.3 PRESCRIBED ROLL OF A SHIP-SHAPED HULL WITH A NON-UNIFORM HULL CROSS-SECTION

The application of the NS2D solver to the prescribed roll motion of a ship-shaped hull with a non-uniform hull cross-section is conducted in this section. The roll angle amplitude of the prescribed roll motion is equal to 5.75 degrees. As shown in Fig. 6.10, a non-uniform cross-section cylindrical hull is placed in a uniform channel with a domain size of $40B$ ($20B$ on each side of the hull) long, $4B$ wide and $6.67B$ deep. The bottom figure in Fig. 6.10 shows a blowup view of the cylindrical hull, where the symbol B stands for the hull beam at $z=0$, and the beam length at $z=4B$ for the non-uniform hull cross-section is equal to $0.8B$. The hull cross-section is diminishing in the z -direction, but the bilge radius is kept the same, which is equal to $0.02B$. The boundary conditions are the same as those applied in the uniform cross-section cylindrical hull problem, except that the sidewall boundaries are replaced by a symmetry boundary at $z=0$ and a no-slip boundary condition at $z=4B$. The computational domain contains eight strips of hexahedral cells and a total number of 45,632 cells.

As shown in Fig. 6.11, the vorticity contour and the vorticity iso-surface are plotted at $t/T=5.00$, and the figure shows that the size of the vortices is changing in the z -direction due to the non-uniform cross-section cylindrical hull geometry. Three slices of pressure contours for x - y plane located at $z/B=0$, $z/B=2$ and $z/B=4$ are plotted in Fig. 6.12, and the 3D pressure contours for $Fn=0.8$ and $Fn=1.2$ are presented in Fig. 6.13 and Fig. 6.14, respectively. The three-dimensionality can clearly be observed in Fig. 6.11 to Fig. 6.14. Moreover, for two given roll frequencies, $Fn=0.8$ and $Fn=1.2$, the comparisons between the results from the NS3D solver and those from the 2D approach using strip theory are shown in Fig. 6.15 and Fig. 6.16, respectively. In this study, the domain is divided into five strips in the z -direction when implementing strip theory, and each strip

is simulated using the NS2D solver with a different hull cross-section. The corresponding moment from each strip is integrated along the z-direction. The results from NS3D show good agreement with those from the 2D approach using strip theory. Moreover, a slight deviation found near the peak of the roll moment indicates the need of a fully three-dimensional solver to accurately predict the wave-hull interaction. Note that, the study is limited in the grid resolution, particularly in the z-direction due to the limitation of the computational resources. Nevertheless, the results show the capability of the NS3D solver for applying to fully 3D ship motion problems.

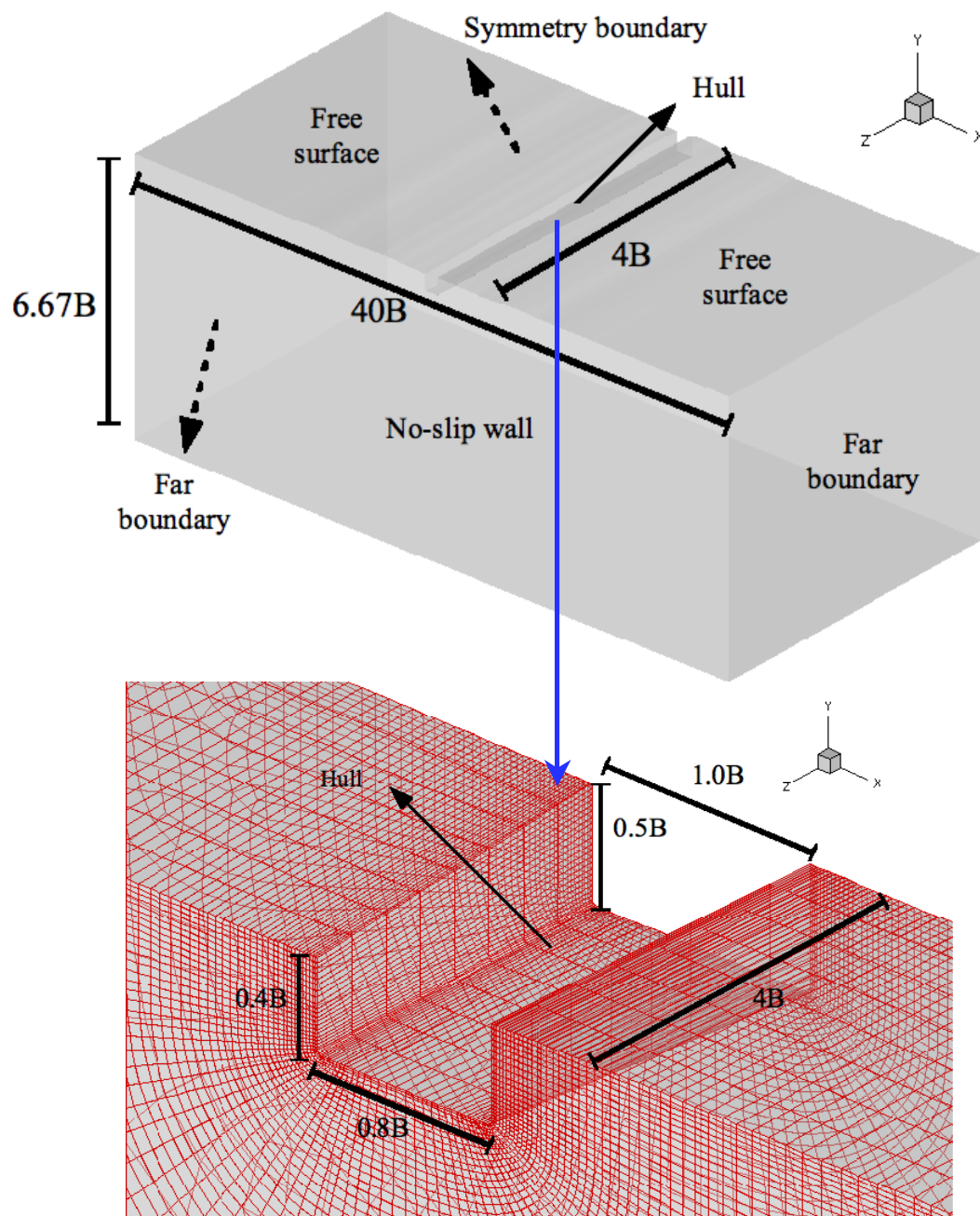


Figure 6.10: Computational domain and corresponding domain boundaries of a 3D prescribed roll motion problem in a uniform channel with a non-uniform hull cross-section, and a blowup view of the hull.

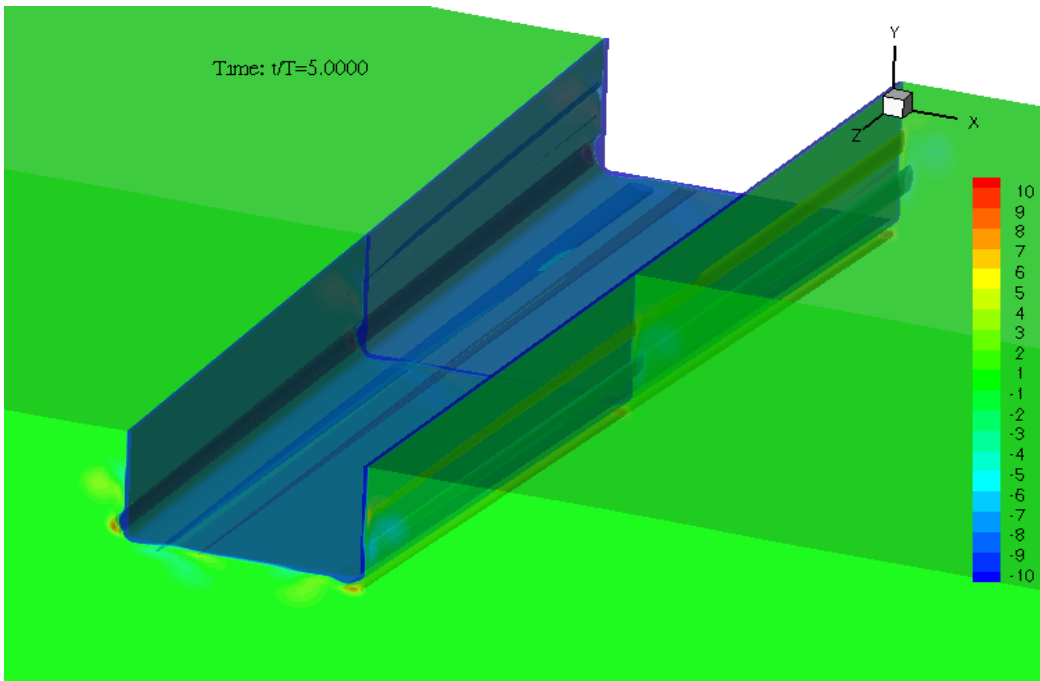


Figure 6.11: The vorticity contour and the vorticity iso-surface of the 3D prescribed roll motion problem in a uniform channel with a non-uniform hull cross-section.

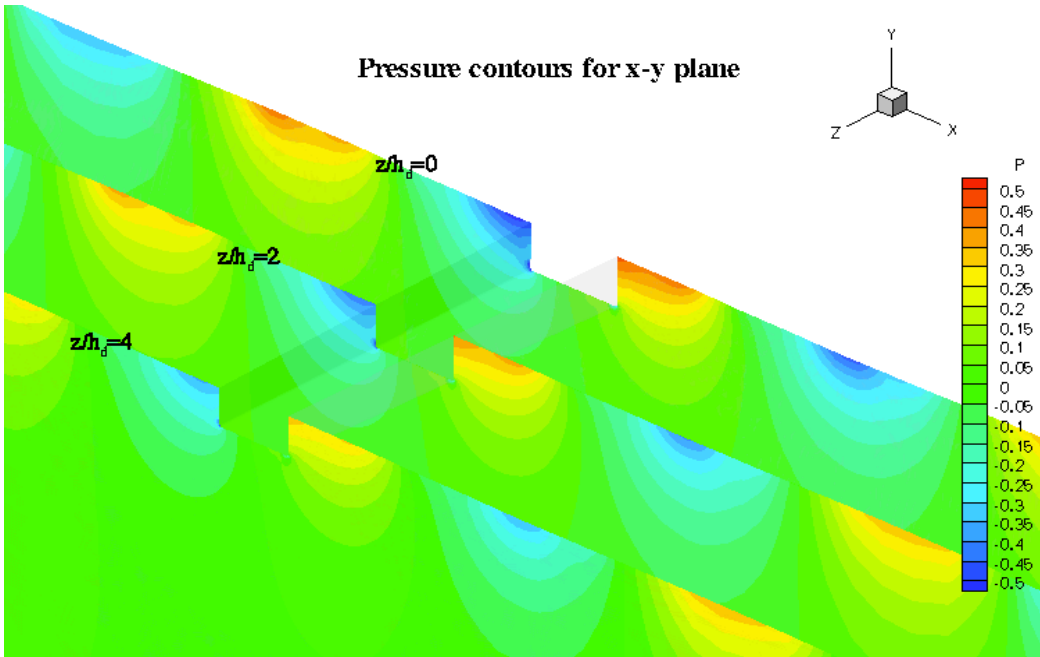


Figure 6.12: Slices of pressure contours for x-y plane in the case of the 3D prescribed roll motion problem in a uniform channel with a non-uniform hull cross-section.

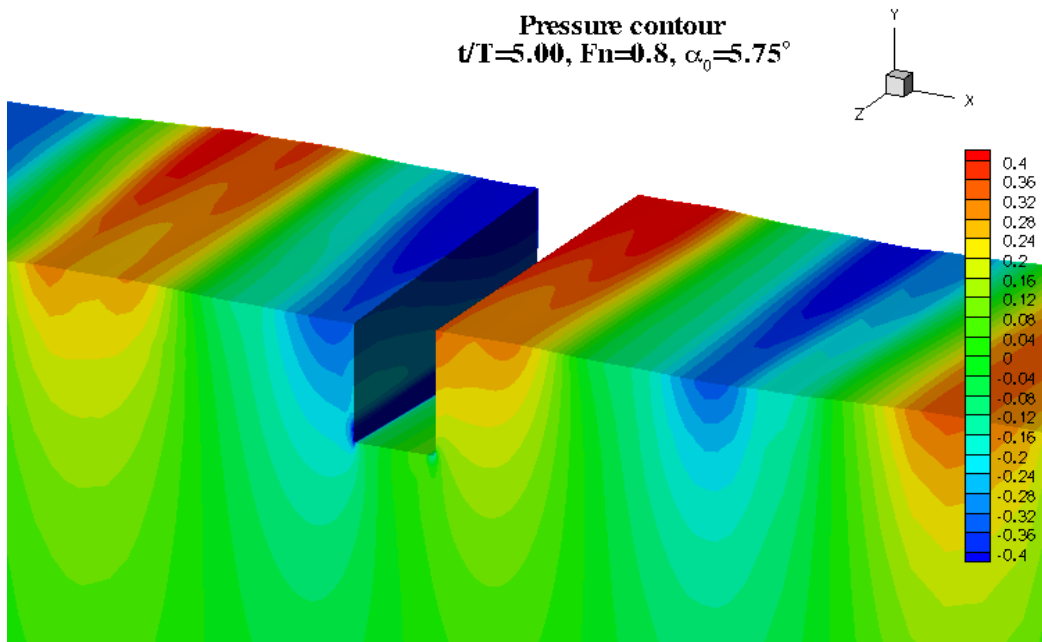


Figure 6.13: Pressure contours for the 3D prescribed roll motion problem in a uniform channel with a non-uniform hull cross-section ($Fn=0.8$).

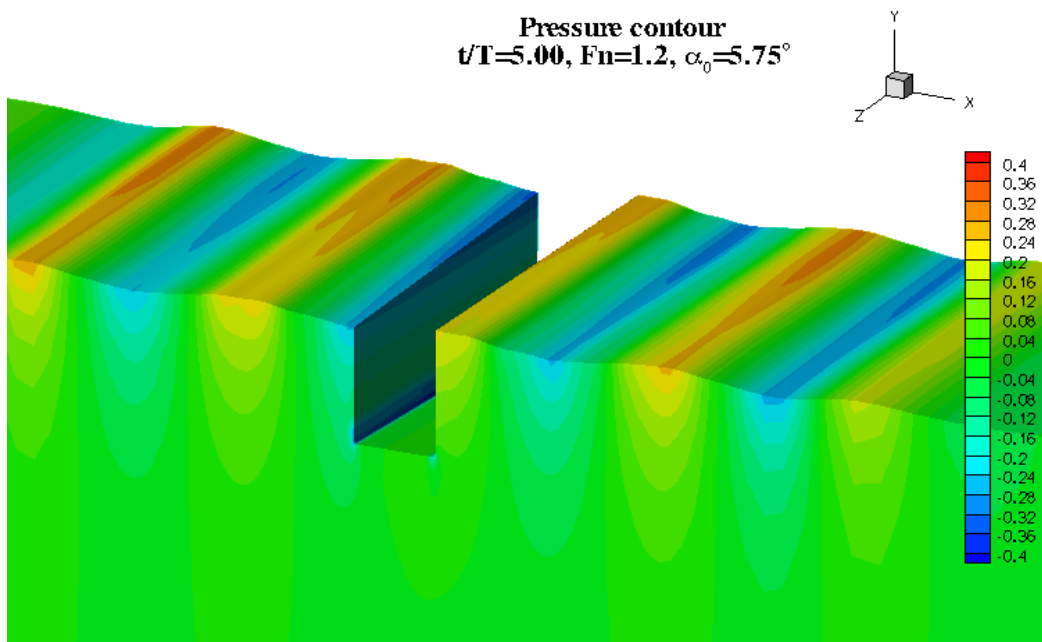


Figure 6.14: Pressure contours for the 3D prescribed roll motion problem in a uniform channel with a non-uniform hull cross-section ($Fn=1.2$).

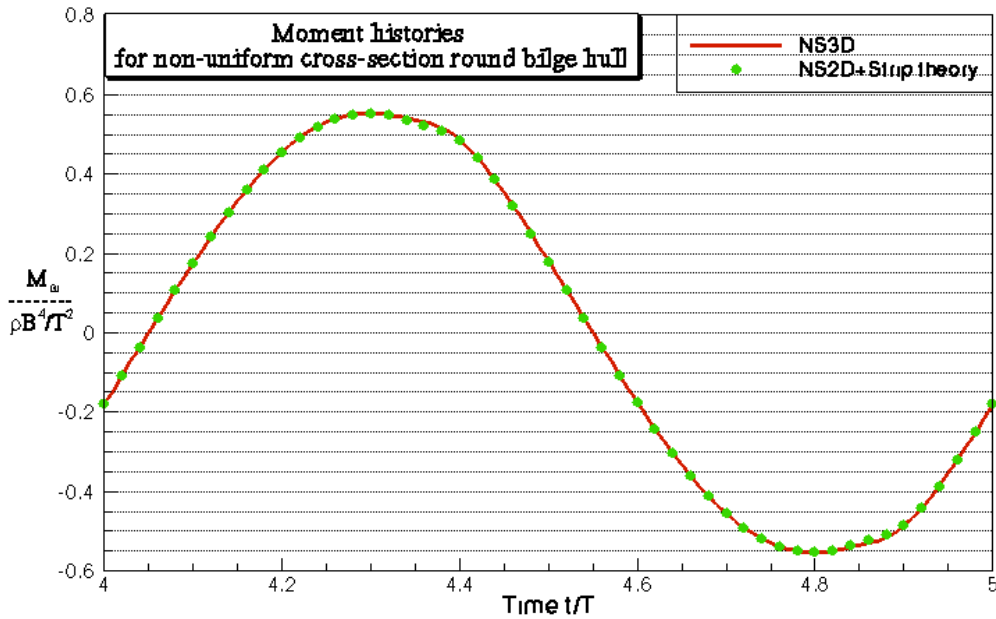


Figure 6.15: Moment histories for non-uniform cross-section cylindrical hull (round bilge model, $F_n=0.8$ and $\alpha_0=5.75^\circ$).

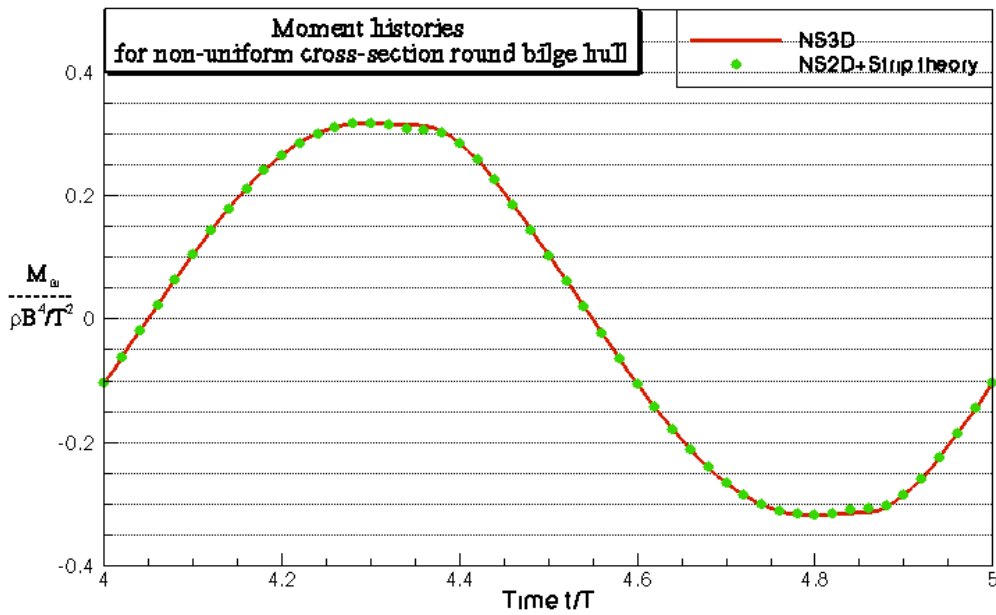


Figure 6.16: Moment histories for non-uniform cross-section cylindrical hull (round bilge model, $F_n=1.2$ and $\alpha_0=5.75^\circ$).

6.4 SUMMARY

The application of the NS3D solver to the wave-maker problem and the prescribed roll motion problems with a uniform or non-uniform cross-section hull are presented in this section. The NS3D results are verified fully with those from NS2D in the wave-maker problem and in the prescribed roll motion problem with a uniform hull cross-section, and with those from the 2D strip-wise approximation in the non-uniform cylindrical hull case. The results have proved that the full-scale application of the NS3D solver for 3D ship motion problems is feasible. However, a further improvement on the solver for parallel computing is needed in order to perform studies on more complex hull geometries.

Chapter 7: Conclusions and Recommendations

7.1 CONCLUSIONS

An unsteady Navier-Stokes solver has been developed, and was applied to predict the flow around ship-shaped hull sections and the corresponding hydrodynamic loads with an emphasis on roll. A step-by-step approach was followed towards this goal by initially performing NS2D simulations for submerged bodies subject to an oscillating inflow (vertical plate and fixed submerged hulls) and for a 2D piston type wave-maker. As an extension of these studies, the NS2D solver was modified and applied to hull motion simulations, where different hull geometries were subject to prescribed roll motions (with or without the presence of the free surface) or in free-decay motions. Based on the 2D algorithm, the solver has also been successfully extended into three dimensions (NS3D) and validated in multiple cases. The main contributions of the research are:

- *Development of an effective method to simulate hull motions and to predict the corresponding hydrodynamic loads:* A two-dimensional FVM based numerical scheme (NS2D) has been developed. The method solves the unsteady laminar Navier-Stokes equations and applies fully non-linear boundary conditions on the free surface. The results compare well with those from the commercial CFD tool FLUENT, a BEM based potential flow solver and other methods.

Potential flow solvers are known as an effective tool for predicting the free-surface elevation, and have the advantage of requiring less computational resources. As shown in Vugts (1968); Roddier (2000) and in the present study, the effect of viscosity is significant in predicting hull roll motions and corresponding

hydrodynamic loads, which makes the application of the viscous solver to ship roll motion problems inevitable.

A one-to-one comparison can be made between the commercial CFD tool FLUENT and NS2D since both are FVM based viscous solvers. FLUENT has the advantage over NS2D in its ability to solve turbulent flow, as well as in laminar, and can be run in parallel. On the other hand, NS2D simulations require less grid resolution near the hull geometry than FLUENT runs to produce results with the same accuracy due to the boundary conditions and numerical settings. In addition, the application of the GMRES algorithm in the NS2D solver gives a better convergence rate in solving the system of algebraic equations. The NS2D solver, therefore, is more efficient for solving hull motion problems in laminar flow by using a single CPU. However, in the case of submerged hulls, the aforementioned advantages are not sufficient to beat the parallel capability of FLUENT at very fine grid resolutions. In spite of FLUENT's capability to handle over-turning and breaking waves by using VOF method, the present research focuses on ship-shaped hull roll motion problems, where the effect of over-turning or breaking waves usually does not play an important role in the prediction of ship motions and the corresponding hydrodynamic loads. Moreover, it is more computationally expensive to use VOF method for capturing the free surface. Therefore, the development of a robust and efficient computational tool for simulating ship motions is in demand, and the NS2D solver has shown the advantage of being applied to ship-shaped hull roll motion problems.

- *Systematic studies on two-dimensional ship-shaped hull motions:* In the case of prescribed roll motions, sensitivity analyses in space and in time were performed, and the effect of turbulence is studied by using FLUENT with the implementation

of the $k-\omega$ model. The effect of turbulence is found to be small in the simulations of ship-shaped hull motions even with the installation of bilge keels. The free surface effects were addressed by comparing the results from ship-shaped hulls to those from submerged hulls, and the results show that the wave propagation on free surface carries energy away from the hull. As a result, a lower roll frequency produces a smaller wave height on the free surface, which leads to higher hydrodynamic loads on the hull. A study on different roll angle amplitudes was performed using the round bilge hull, and the results show that the current model can handle roll angles up to 20 degrees. The effects of hull geometries are investigated, and the study also includes the effects of keel lengths for the bilge keel model. In the case of free-decay motions, the effects of hull geometries and initial roll angles on roll decay motions were also analyzed. Among all the analyzed hull models, the 4% bilge keel model has been demonstrated to be the most effective model in terms of roll decay and has the highest roll decay rate.

In general, the moment histories predicted from NS2D, FLUENT and other methods show a good agreement. Also, the corresponding hydrodynamic coefficients predicted from all these methods agree fairly well. However, some differences were observed in the study, particularly in the case of the 4% bilge keel model. Despite the fact that the roll moment histories from NS2D and FLUENT are very similar, the resulting added-mass coefficients have a significant difference in the case of $F_n=0.6$. In the present study, it has also been found that using a linear combination of added-mass and damping coefficients to represent a periodic force or moment histories can be inadequate, particularly for the hulls subject to roll motions. Therefore, the calculation of the hull response in time domain becomes inevitable.

- *Extension of the present method into three dimensions:* The present numerical scheme has been successfully extended from two into three dimensions. The NS3D solver has been well validated in three test cases. The first two cases are 3D problems with 2D solutions, and the 3D results are compared well to those solved in 2D. The last one is conducted for a hull with non-uniform cross-section subject to prescribed roll motions, and the results are compared to those from the 2D approach using strip theory. The NS3D results show the capability of the present numerical scheme to apply to fully 3D ship motion simulations.

7.2 RECOMMENDATIONS

Over the course of this research, the agreement between the results from NS2D and those from other methods has been satisfactory, giving the confidence in the present numerical scheme. However, the ultimate objective of this research is to model the interaction between incoming waves and an FPSO vessel in roll. To achieve this goal, the following may be included:

- *Parallelization of the numerical solver:* The two-dimensional numerical solver has been successfully extended into three dimensions. However, the application of the present solver to a three-dimensional problem with more complex hull geometries is limited by the high demand of computational resources. A parallel version of the Navier-Stokes solver can resolve this issue by dividing the computational domain into several smaller zones, and then solving the problem in parallel.
- *Handling more complex geometries:* In 2D simulations, the present study has shown that the prediction of shed vortices for hulls with sharp corners, e.g., bilge

keel model, is complicated, and more studies are needed, particularly when the roll frequency is low. For 3D simulations, the gap effect between the hull and the side boundary (in the case of hull sections tested in between the walls of a wave basin) need to be analyzed, and more studies of the ship motions with full-scale FPSO vessel geometries need to be included. In addition, comparisons can be made between the results from the two-dimensional strip-wise approximation and those from a fully three-dimensional simulation. The difference between them should also be addressed in the future.

- *Ship motion in an ambient wave field:* The study of prescribed or free-decay motions of hulls can provide useful information for ship design. However, studies on hulls in waves are still in demand, particularly for FPSO vessels subject to incoming waves with various frequencies and heading angles. The analysis of the hydrodynamic interaction and motion responses of adjacent multiple floating vessels in waves must also be addressed, due to their importance in affecting the FPSO-shuttle offloading operability.
- *Turbulent flow modeling:* As shown in the present study, the effect of turbulence is small when predicting the hydrodynamic loads in ship-shaped hull roll motion problems and also in the case of submerged hulls with round corners (round bilge model). For submerged hulls with sharp corners, according to our numerical experience, the results were found to be very sensitive to grid resolution, and therefore, more studies on these aspects need to be addressed in the future. Moreover, in the present study, the effect of turbulence was performed using FLUENT, and the model coefficients are based on the default settings, which are not defined specifically for modeling ship roll motion problems of hulls with sharp corners. The values of those given model coefficients can be inadequate and

may produce a higher dissipation of the vortices near the hull. A study of the effect of turbulence by using Direct Numerical Simulation (DNS) method in the case of hull sections in roll could be very helpful, and should be addressed in the future.

Appendix A: Approximation of Fluxes and Cell Face Values

This appendix describes the calculations for the cell face value, the normal derivative values and the convective flux.

A.1 CALCULATIONS FOR CELL FACE VALUE

From Eq. (3.11) and Eq. (3.13), the cell face value is obtained using Taylor series expansion:

$$\Phi_f = \Phi_{f'} + \Delta\vec{X}_{f-f'} \cdot \nabla\Phi_{f'} + H \approx \Phi_{f'} + \Delta\vec{X}_{f-f'} \cdot \nabla\Phi_{f'} \quad (3.11)$$

$$\Phi_{f'} \approx (C_P)_f \Phi_P + C_{NB} \Phi_{NB}, \quad (3.13)$$

$$\nabla\Phi_{f'} \approx (C_P)_f \nabla\Phi_P + C_{NB} \nabla\Phi_{NB}.$$

where the corresponding coefficients $(C_P)_f$ and C_{NB} are given as:

$$(C_P)_f = \frac{|\Delta\vec{X}_{NB-f'}|}{|\Delta\vec{X}_{P-f'}| + |\Delta\vec{X}_{NB-f'}|} = \frac{|\Delta\vec{X}_{NB-f}|}{|\Delta\vec{X}_{P-f}| + |\Delta\vec{X}_{NB-f}|}, \quad (A.1)$$

$$C_{NB} = \frac{|\Delta\vec{X}_{P-f'}|}{|\Delta\vec{X}_{P-f'}| + |\Delta\vec{X}_{NB-f'}|} = \frac{|\Delta\vec{X}_{P-f}|}{|\Delta\vec{X}_{P-f}| + |\Delta\vec{X}_{NB-f}|},$$

which lead to:

$$\Phi_f \approx (C_P)_f (\Phi_P + \Delta\vec{X}_{f-f'} \cdot \nabla\Phi_P) + C_{NB} (\Phi_{NB} + \Delta\vec{X}_{f-f'} \cdot \nabla\Phi_{NB}). \quad (A.2)$$

From Eq. (3.14):

$$\nabla\Phi_p \approx \frac{1}{\nabla} \sum_{\partial\forall} \Phi_f \bar{n}A_f. \quad (3.14)$$

It is assumed that Φ_f is known from previous iteration, and Eq. (3.14) and Eq. (A.2) are then solved through iterative procedure. For better convergence rate, Eq. (A.2) can be applied again in Eq. (3.14), which gives:

$$\begin{aligned} \nabla\Phi_p &\approx \frac{1}{\nabla} \sum_{\partial\forall} (\Phi_{f'} + \Delta\bar{X}_{f-f'} \cdot \nabla\Phi_{f'}) \bar{n}A_f \\ &= \frac{1}{\nabla} \sum_{\partial\forall} \left[(C_p)_f (\Phi_p + \Delta\bar{X}_{f-f'} \cdot \nabla\Phi_p) \right. \\ &\quad \left. + C_{NB} (\Phi_{NB} + \Delta\bar{X}_{f-f'} \cdot \nabla\Phi_{NB}) \right] \bar{n}A_f \end{aligned} \quad (A.3)$$

When the above equation is substituted into Eq. (A.2), the cell face value is given as:

$$\Phi_f \approx d_p \Phi_p + \hat{d}_p \nabla\Phi_p + \sum_l d_l \Phi_l + \sum_l \hat{d}_l \nabla\Phi_l, \quad (A.4)$$

$l = \text{surrounding cells.}$

where the subscript "l" represents the surrounding cells, which includes all the *NB* points and the neighboring points around each *NB*; d_p , d_l , \hat{d}_p and \hat{d}_l represent the corresponding coefficients; and " $\hat{}$ " indicates the coefficients that are associated with irregular grids, which become zero when f and f' are collocated on each cell face.

A.2 CALCULATIONS FOR NORMAL DERIVATIVE VALUES

From Eq. (3.15), the derivative of any variable Φ with respect to the normal direction on the cell face is given as:

$$\left(\frac{\partial\Phi}{\partial n}\right)_f \approx \frac{\Phi_{NB'} - \Phi_{P'}}{(\vec{X}_{NB'} - \vec{X}_{P'}) \cdot \vec{n}} \quad (3.15)$$

The values at those two auxiliary points are calculated using Taylor series expansion:

$$\begin{aligned} \Phi_{P'} &\approx \Phi_P + \Delta\vec{X}_{P'-f} \cdot \nabla\Phi_P, \\ \Phi_{NB'} &\approx \Phi_{NB} + \Delta\vec{X}_{NB'-f} \cdot \nabla\Phi_{NB}. \end{aligned} \quad (A.5)$$

With these expressions, Eq. (3.15) becomes:

$$\begin{aligned} \left(\frac{\partial\Phi}{\partial n}\right)_f &\approx \frac{\Phi_{NB} - \Phi_P}{(\vec{X}_{NB'} - \vec{X}_{P'}) \cdot \vec{n}} \\ &+ \frac{\Delta\vec{X}_{NB'-f} \cdot \nabla\Phi_{NB} - \Delta\vec{X}_{P'-f} \cdot \nabla\Phi_P}{(\vec{X}_{NB'} - \vec{X}_{P'}) \cdot \vec{n}}. \end{aligned} \quad (A.6)$$

If Eq. (A.3) is again used in Eq. (A.6), it can lead to an algebraic equation:

$$\left(\frac{\partial\Phi}{\partial n}\right)_f \approx j_P\Phi_P + \hat{j}_P\nabla\Phi_P + \sum_l j_l\Phi_l + \sum_l \hat{j}_l\nabla\Phi_l, \quad (A.7)$$

$l =$ surrounding cells.

where j_P , j_l , \hat{j}_P and \hat{j}_l denote the corresponding coefficients.

A.3 CALCULATIONS FOR CONVECTIVE FLUX

From Eq. (3.17), the cell-face velocity vector for calculating the convective flux in the momentum equation is given as:

$$\begin{aligned}\vec{U}_f &\approx C_{up}(\vec{U}_p + \Delta\vec{X}_{f-p} \cdot \nabla\vec{U}_p) + (1 - C_{up})(\vec{U}_{NB} + \Delta\vec{X}_{f-NB} \cdot \nabla\vec{U}_{NB}), \\ C_{up} &= 0.5(v_n + |v_n|) / v_n,\end{aligned}\tag{3.17}$$

When Eq. (A.3) is substituted into Eq. (3.17), the velocity vector on the cell face is obtained, which is given as:

$$\vec{U}_f \approx k_p \vec{U}_p + \sum_l k_l \vec{U}_l + \hat{k}_p \nabla \vec{U}_p + \sum_l \hat{k}_l \nabla \vec{U}_l.\tag{A.8}$$

It is similar to Eq. (A.4) but has different coefficients k_p , k_l , \hat{k}_p and \hat{k}_l . The substitutions of Eq. (3.6), Eq. (A.7), and Eq. (A.8) in Eq. (3.10) result in a system algebraic equation of the momentum equations:

$$a_p \vec{U}_p + \sum_l a_l \vec{U}_l = -\frac{1}{\rho} \sum_{\partial\forall} p_f \vec{n} A_f + \hat{a}_p \nabla \vec{U}_p + \sum_l \hat{a}_l \nabla \vec{U}_l,\tag{3.18}$$

where a_p , a_l , \hat{a}_p and \hat{a}_l are the corresponding coefficients.

Appendix B: Non-Dimensionalization

In the NS2D solver, all the variables are made non-dimensional. Combinations of the following scales are used to non-dimensionalize all the variables, a characteristic length L_o , which is a representative length in the problem being solved (i.e. hull beam B , water depth h_d or plate height h_0), a characteristic time T_o , and a characteristic velocity U_o , which is equal to L_o/T_o . The non-dimensionalizations are summarized as follows:

$$\begin{aligned}
 \vec{X}^* &= \frac{\vec{X}}{L_o}, \quad \nabla^* = \frac{\nabla}{L_o^3}, \quad A_f^* = \frac{A_f}{L_o^2}, \\
 \vec{U}^* &= \frac{\vec{U}}{U_o} = \frac{\vec{U}}{L_o/T_o}, \\
 t^* &= \frac{t}{T_o}, \\
 p^* &= \frac{p}{\rho U_o^2} = \frac{p}{\rho L_o^2 / T_o^2}, \\
 \vec{F}^* &= \frac{\vec{F}}{U_o^2 L_o} = \frac{\vec{F}}{\rho L_o^3 / T_o^2}, \\
 M_o &= \frac{M_o}{\rho U_o^2 L_o^2} = \frac{M_o}{\rho L_o^4 / T_o^2}, \quad M_\omega = \frac{M_\omega}{\rho U_o^2 L_o^2} = \frac{M_\omega}{\rho L_o^4 / T_o^2}.
 \end{aligned} \tag{B.1}$$

The two parameters are used in the NS2D solver. The first is the Reynolds number Re , which controls the flow viscosity in the momentum equations. The other one is the non-dimensional gravity g^* , which is used for calculating the free surface. The two parameters are defined as:

$$\begin{aligned}
g^* &= \frac{g}{L_o / T_o^2}, \\
\text{Re} &= \frac{U_o L_o}{\nu} = \frac{L_o^2 / T_o}{\nu}.
\end{aligned} \tag{B.2}$$

The discrete non-dimensional continuity and Navier-Stokes equations then can be re-written as:

$$\begin{aligned}
\sum_{\partial\forall} (\vec{U}_f^* \cdot \vec{n}) A_f^* &= 0, \\
\frac{\delta \vec{U}^*}{\delta t^*} \nabla^* + \vec{U}^* \frac{\delta \nabla^*}{\delta t^*} + \sum_{\partial\forall} \left[(v_n^* - v_{gn}^*) \vec{U}_f^* - \frac{1}{\text{Re}} \left(\frac{\partial \vec{U}^*}{\partial n} \right)_f \right] A_f^* &= - \sum_{\partial\forall} p_f^* \vec{n} A_f^*.
\end{aligned} \tag{B.3}$$

Glossary

Latin Symbols

A	periodic motion amplitude of the wave-maker
a_{66}	added-mass coefficients
b_{66}	damping coefficients
$a_p, a_l, \hat{a}_p, \hat{a}_l$	coefficients in the system algebraic equation of the momentum equations
A_f	area of the cell side
B	hul beam
C_d	drag coefficient
C_m	inertia coefficient
$(C_p)_f, C_{NB}$	coefficients for linear interpolation
C_{up}	direction coefficient used in upwind scheme
D	hull draft
d_f	coefficient of the velocity-correction correction term, $d_f = a_p + \sum_l a_l$
\vec{F}_B	body force vector
\vec{F}_o	total force vector on the hull
F_c	force value from a coarser grid
F_e	"exact" force value
F_p	horizontal force on the plate
Fn	Froude number (non-dimensional frequency), $Fn = \omega\sqrt{B/2g}$
g	acceleration of gravity
H	High-order terms

h_0	plate height
h_d	water depth in wave-maker problem
$h_p, h_l, \hat{h}_p, \hat{h}_l$	coefficients in the system algebraic equation of the pressure-correction equation
KC	Keulegan-Carpenter number, $KC=U_{in}T_{in}/h_0$.
L_0, L_1	vertices on the free surface and one level below the free surface
\dot{m}	mass flux of each cell face
\bar{n}	unit normal vector to the cell face
(n_x, n_y, n_z)	Cartesian components of \bar{n}
N_T	number of data points used for calculating the least square error
M_ω	hydrodynamic moment
M_o	total moment
M_c	moment from a coarser grid
M_e	"exact" moment
O	coordinate system origin
p	pressure
p_{ap}	atmosphere pressure
Re	Reynolds number, $Re=U_0L/\nu$.
R_f	ramp function for prescribed roll motion
\bar{s}	unit tangential vector to the cell face
$S_F(t)$	instantaneous position of the free-surface
$S_H(t)$	instantaneous position of the hull surface
t	time
T	period of the sinusoidal function
T_o	a characteristic time

T_{in}	period of the sinusoidal inflow
(u, v, w)	three velocity components in the Cartesian coordinate system
(u_g, v_g, w_g)	three grid velocity components in the Cartesian coordinate system
\vec{U}	velocity vector
U_0	a characteristic velocity
v_{gn}	normal component of the velocity of the control volume boundary
v_n	normal component of the flow velocity on the cell face
v_s	tangential component of the flow velocity on the cell face
(x, y, z)	three directions in Cartesian coordinate system

Greek Symbols

α	angle of roll
$\dot{\alpha}$	angular velocity
$\ddot{\alpha}$	angular acceleration
α_0	roll angle amplitude
β	frequency ratio
δ	boundary-layer cell height
$\Delta\vec{X}$	distant vector between two points
Δt	time step size
$\Delta\Omega_f$	volume swept by the cell boundary between two time steps
ε_F	absolute least square error of the force history
ε_m	absolute least square error of the moment history
Φ	an arbitrary variable
η	wave height

ν	kinematic viscosity
ρ	density
ω	frequency of roll

Other Symbols

\forall	volume of the control volume
$\partial\forall$	boundary of the control volume
\wedge	coefficients that are associated with irregular grids
\sim	provisional value in the SIMPLE algorithm
overbar	interpolated value at the cell face

Subscripts

DB	point index at the domain-boundary cell face
FS	point index at the free-surface-boundary cell face
f	point index at the center of the cell face
f	point on the line between P and NB
i	data index at each time step
l	point index at the center point of the surrounding cell (NB cells and the neighboring cells around each NB cell)
NB	point index at neighboring point (on either side of the cell face)
P	point index at the center of the cell
tn	node point indices at the domain-boundary cell face

Superscripts

$m+1$	time index at current time step
$m-1, m$	time indices at previous time steps
'	correction term
*	non-dimensional term

Acronyms

BEM	Boundary Element Method
CDS	Central Differencing Scheme
CFD	Computational Fluid Dynamics
CPU	Central Processing Unit
CV	Control Volume
DFSBC	Dynamic Free Surface Boundary Condition
FPSO	Floating, Production, Storage and Offloading (vessels)
FVM	Finite Volume Method
KFSBC	Kinematic Free Surface Boundary Condition
RANS	Reynolds Averaged Navier-Stokes (equations)
SIMPLE	Semi-Implicit Method for Pressure-Linked Equations
VOF	Volume Of Fluid

Computer Programs

BFFDM	Boundary-Fitted Finite-Difference Method based numerical solver (Alessandrini and Delhommeau 1994)
FLUENT	commercial CFD software

FSRVM	Free-Surface Random Vortex Method based numerical solver (Yeung et al. 1993)
GAMBIT	grid generator provided by FLUENT Company
MBLF	BEM based potential flow solver (Moving Body Linear Free- surface)
NL-BEM	BEM based potential flow solver (fully non-linear free surface)
NS2D/NS3D	two-dimensional/three-dimensional Navier-Stokes solver

References

- Alessandrini, B., and Delhommeau, G. (1994). "Simulation of 3-Dimensional Unsteady Viscous Free-Surface Flow around a Ship Model." *Int. J. Numer. Methods Fluids*, 19(4), 321-342.
- Alessandrini, B., and Delhommeau, G. (1998). "Viscous free surface flow past a ship in drift and in rotating motion." *Proceedings of the 22nd ONR Symposium on Naval Hydrodynamics*, Washington, DC.
- Choi, D. Y., and Wu, C. H. (2006). "A new efficient 3D non-hydrostatic free-surface flow model for simulating water wave motions." *Ocean Engineering*, 33(5-6), 587-609.
- Choi, J. K. (2000). "Vortical inflow - propeller interaction using an unsteady three-dimensional Euler solver." *PhD Dissertation*, University of Texas at Austin.
- Choi, J. K., and Kinnas, S. A. (2001). "Prediction of non-axisymmetric effective wake by a three-dimensional Euler solver." *J. Ship Res.*, 45(1), 13-33.
- Choi, J. K., and Kinnas, S. A. (2003). "Prediction of unsteady effective wake by a Euler solver/vortex-lattice coupled method." *J. Ship Res.*, 47(2), 131-144.
- Clement, A. (1996). "Coupling of Two Absorbing Boundary Conditions for 2D Time-Domain Simulations of Free Surface Gravity Waves." *Journal of Computational Physics*, 126(1), 139-151.
- Demirdzic, I., and Peric, M. (1988). "Space conservation law in finite volume calculations of fluid flow." *Int. J. Numer. Methods Fluids*, 8(1037-1050), 97.
- Di Mascio, A., and Campana, E. (1999). "The numerical simulation of the yaw flow of a free surface ship." *Proceedings of the 7th International Conference on Numerical Ship Hydrodynamics*, Nantes, France.
- Farhat, C., Geuzaine, P., and Grandmont, C. (2001). "The discrete geometric conservation law and the nonlinear stability of ALE schemes for the solution of flow problems on moving grids." *Journal of Computational Physics*, 174(2), 669-694.
- Ferziger, J. H., and Peric, M. (2002). "Computational methods for fluid dynamics." Springer, New York.
- Gentaz, L., Maury, C., Alessandrini, B., and Delhommeau, G. (2000). "Numerical simulations of a two-dimensional wave tank in viscous fluid." *International Journal of Offshore and Polar Engineering*, 10(1), 1-9.
- Hendrickson, K. L. (2005). "Navier-Stokes simulations of steep breaking water waves with a coupled air-water interface." MIT.

- Himeno, Y. (1981). "Prediction of Ship Roll Damping. A State of the Art." Rept. No. 239 University of Michigan at Ann Arbor, Department of Naval Architecture.
- Hochbaum, A., and Vogt, M. (2002). "Towards the simulation of seakeeping and maneuvering based computation of the free surface viscous ship flow." *Proceedings of the 24th ONR Symposium on Naval Hydrodynamics*, Fukuoka, Japan.
- Irvine, M., Atsavapranee, P., Carneal, J., Engle, A., Pervoal, S., Bishop, R., Grant, D., Lugni, C., Di Felice, F., Longo, J., and Stern, F. (2006). "Comparison of Free Roll Decay Tests for Model DTMB 5415/2340/5512, and Investigation of Lateral Hydrodynamic Loads on Bilge keels." *Proceedings of the 26th ONR Symposium on Naval Hydrodynamics*, Rome, Italy.
- Irvine, M., Longo, J., and Stern, F. (2008). "Pitch and heave tests and uncertainty assessment for a surface combatant in regular head waves." *J. Ship Res.*, 52(2), 146-163.
- Issa, R. I. (1986). "Solution of the implicitly discretised fluid flow equations by operator-splitting." *Journal of Computational Physics*, 62(1), 40-65.
- Kacham, B. (2004). "Inviscid and Viscous 2D Unsteady Flow Solvers Applied to FPSO Hull Roll Motions." *MS. Thesis*, University of Texas at Austin.
- Kakar, K. (2002). "Computational Modeling of FPSO Hull Roll Motions and Two-component Marine Propulsion Systems." *MS. Thesis*, University of Texas at Austin.
- Kasten, M. (2002). "An overview of a few common roll attenuation strategies for motor yachts and motor sailors." <<http://www.kastenmarine.com/>> (7/25, 2008).
- Kinnas, S. A., Yu, Y.-H., Lee, H., and Kakar, K. (2003). "Modeling of Oscillating Flow Past a Vertical Plate." *International Offshore and Polar Engineering Conference*, ISOPE, Honolulu, HI, United States, 218-226.
- Kinnas, S. A., Yu, Y.-H., and Vinayan, V. (2006). "Prediction of flows around FPSO hull sections in roll using an unsteady Navier-Stokes solver." *International Offshore and Polar Engineering Conference*, ISOPE, San Francisco, CA, United States, 384-393.
- Kinnas, S. A., Yu, Y.-H., and Vinayan, V. (2007). "Numerical methods for the prediction of the bilge keel effects on the response of ship-shaped hulls." *International Conference on Offshore Mechanics and Arctic Engineering*, OMAE, San Diego, CA, United States, 1023-1030.
- Korpus, R. A., and Falzarano, J. M. (1997). "Prediction of viscous ship roll damping by unsteady Navier-Stokes techniques." *Journal of Offshore Mechanics and Arctic Engineering-Transactions of the Asme*, 119(2), 108-113.

- Korvin-Kroukovsky, B. V. (1955). "Investigation of ship motions in regular waves." *Trans. SNAME*, 63, 386-435.
- Lehnhauser, T., and Schafer, M. (2002). "Improved linear interpolation practice for finite-volume schemes on complex grids." *Int. J. Numer. Methods Fluids*, 38(7), 625-645.
- Lehnhauser, T., and Schafer, M. (2003). "Efficient discretization of pressure-correction equations on non-orthogonal grids." *Int. J. Numer. Methods Fluids*, 42(2), 211-231.
- Lesoinne, M., and Farhat, C. (1996). "Geometric conservation laws for flow problems with moving boundaries and deformable meshes, and their impact on aeroelastic computations." *Computer Methods in Applied Mechanics and Engineering*, 134(1-2), 71-90.
- Li, B., and Fleming, C. A. (2001). "Three-Dimensional Model of Navier-Stokes Equations for Water Waves." *Journal of Waterway, Port, Coastal and Ocean Engineering*, 127(1), 16-25.
- Lin, P., and Li, C. W. (2002). "A sigma-coordinate three-dimensional numerical model for surface wave propagation." *Int. J. Numer. Methods Fluids*, 38(11), 1045-1068.
- Lin, W. M. (1984). "Nonlinear motion of the free surface near a moving body." M. I. T., Dept. of Ocean Engineering.
- Longuet-Higgins, M. S., and Cokelet, E. D. (1976). "The deformation of steep surface waves on water." *Proc. R. Soc. Lond. A*, 350, 1-26.
- Miller, R., Gorski, J., and Fry, D. (2002). "Viscous roll predictions of a circular cylinder with bilge keels." *Proceedings of the 24th ONR Symposium on Naval Hydrodynamics*, Fukuoka, Japan.
- Na, J. H., Lee, W. C., Shin, H. S., and Park, I. K. (2002). "A Design of Bilge Keels for Harsh Environment FPSOs." *International Offshore and Polar Engineering Conference*, ISOPE, Kitakyushu, Japan, 114-117.
- Patankar, S. V. (1980). "Numerical heat transfer and fluid flow." *Washington, DC, Hemisphere Publishing Corp., 1980. 210 p.*
- Patankar, S. V., and Spalding, D. B. (1972). "A calculation procedure for heat, mass, and momentum transfer in three-dimensional flows." *Int. J. Heat Mass Transfer*, 15, 1787.
- Peric, M. (1985). "A Finite Volume Method for the Prediction of Three-Dimensional Fluid Flow in Complex Ducts." *University of London, PhD thesis.*
- Peric, M. (1990). "Analysis of Pressure-Velocity Coupling on Nonorthogonal Grids." *Numerical Heat Transfer Part B-Fundamentals*, 17(1), 63-82.

- Roddier, D. (2000). "Hydrodynamics of Rolling Cylinders With and Without Bilge Keels." *PhD Dissertation*, University of California at Berkeley.
- Sarkar, T., and Vassalos, D. (2001). "A RANS-based technique for simulation of the flow near a rolling cylinder at the free surface." *Journal of Marine Science and Technology*, 5(2), 66-77.
- Sarpkaya, T., and Okeefe, J. L. (1996). "Oscillating flow about two and three-dimensional bilge keels." *Journal of Offshore Mechanics and Arctic Engineering-Transactions of the Asme*, 118(1), 1-6.
- Sato, Y., Miyata, H., and Sato, T. (2000). "CFD simulation of 3-dimensional motion of a ship in waves: application to an advancing ship in regular heading waves." *Journal of Marine Science and Technology*, 4(3), 108-116.
- Seah, R. K. M., and Yeung, R. W. (2003). "Sway and Roll Hydrodynamics of Cylindrical Sections." *International Offshore and Polar Engineering Conference*, ISOPE, Honolulu, HI, United States, 1861-1868.
- Sen, D. (2002). "Time-domain computation of large amplitude 3D ship motions with forward speed." *Ocean Engineering*, 29(8), 973-1002.
- Simonsen, C. D., and Stern, F. (2003). "Verification and validation of RANS maneuvering simulation of Esso Osaka: effects of drift and rudder angle on forces and moments." *Computers and Fluids*, 32(10), 1325-1356.
- Simonsen, C. D., and Stern, F. (2005). "RANS maneuvering simulation of Esso Osaka with rudder and a body-force propeller." *J. Ship Res.*, 49(2), 98-120.
- Tahara, Y., Longo, J., Stern, F., and Himeno, Y. (1998). "Comparison of CFD and EFD for the Series 60 CB = 0.6 in steady yaw motion." *Proceedings of the 22nd ONR Symposium on Naval Hydrodynamics*, Washington, DC.
- Tahara, Y., and Stern, F. (1996). "A large-domain approach for calculating ship boundary layers and wakes and wave fields for nonzero Froude number." *Journal of Computational Physics*, 127(2), 398-411.
- Tahara, Y., Stern, F., and Rosen, B. (1992). "An interactive approach for calculating ship boundary layers and wakes for nonzero Froude number." *Journal of Computational Physics*, 98(1), 33-53.
- Taz Ul Mulk, M., and Falzarano, J. (1994). "Complete Six-Degrees-of-Freedom Nonlinear Ship Rolling Motion." *TRANSACTIONS-AMERICAN SOCIETY OF MECHANICAL ENGINEERS JOURNAL OF OFFSHORE MECHANICS AND ARCTIC ENGINEERING*, 116, 191-191.
- Thomas, P. D., and Lombard, C. K. (1979). "Geometric conservation law and its application to flow computations on moving grids." *AIAA Journal*, 17(10), 1030-1037.

- Van Doormaal, J. P., and Raithby, G. D. (1984). "Enhancements of the SIMPLE method for predicting incompressible fluid flows." *Numerical Heat Transfer*, 7(2), 147-163.
- Vinayan, V., Kinnas, S. A., and Yu, Y.-H. (2005). "Modeling of flow around FPSO hull sections subject to roll motions: Effects of nonlinear boundary conditions." *International Conference on Offshore Mechanics and Arctic Engineering - OMAE*, American Society of Mechanical Engineers, New York, NY 10016-5990, United States, Halkidiki, Greece, 805-816.
- Vugts. (1968). "The Hydrodynamic Coefficients for Swaying, Heaving and Rolling Cylinders in a Free Surface." Rept. No. 194, Laboratorium voor Scheepsboukunde, Technische Hogeschool Delft, The Netherlands.
- Weymouth, G. D., Wilson, R. V., and Stern, F. (2005). "RANS Computational Fluid Dynamics Predictions of Pitch and Heave Ship Motions in Head Seas." *J. Ship Res.*, 49(2), 80-97.
- Wilson, R., Paterson, E., and Stern, F. (1998). "Unsteady RANS CFD method for naval combatant in waves." *Proceedings of the 22nd ONR Symposium on Naval Hydrodynamics*, Washington, DC, 183-197.
- Wilson, R. V., Carrica, P. M., and Stern, F. (2006). "Unsteady RANS method for ship motions with application to roll for a surface combatant." *Computers and Fluids*, 35(5), 501-524.
- Yeung, R. W., Liao, S. W., and Roddier, D. (1998). "On roll hydrodynamics of rectangular cylinders." *International Offshore and Polar Engineering Conference*, ISOPE, Montreal, Can, 445-453.
- Yeung, R. W., Roddier, D. R., Alessandrini, L., Gentaz, L., and Liao, S. W. (2000). "On Roll Hydrodynamics of Cylinders Fitted with Bilge Keels." *Proceedings of the 23rd ONR Symposium on Naval Hydrodynamics*, Val de Reuil, France.
- Yeung, R. W., Sphaier, S. H., and Vaidhyanathan, M. (1993). "Unsteady flow about bluff cylinders." *International Journal of Offshore and Polar Engineering*, 3(2), 81-92.
- Yu, Y.-H., and Kinnas, S. A. (2008). "Prediction of Hydrodynamic Performance for Various Ship-Shaped Hulls under Excessive Roll Motions Using an Unsteady Navier-Stokes Solver." *International Offshore and Polar Engineering Conference*, ISOPE, Vancouver, BC, Canada, 386-394.
- Yu, Y.-H., Kinnas, S. A., Vinayan, V., and Kacham, B. K. (2005). "Modeling of flow around FPSO hull sections subject to roll motions: Effect of the separated flow around bilge keels." *International Offshore and Polar Engineering Conference*, ISOPE, Seoul, South Korea, 163-170.

Yuck, R. H., Lee, D. H., Choi, H. S., Jin, Y. M., and Bang, C. S. (2003). "A study on roll damping of 2-D cylinders." *International Journal of Offshore and Polar Engineering*, 13(3), 205-208.

Vita

Yi-Hsiang Yu was born to Jing Yu and Jya-Yi Wu on August 21st, 1976 in Taipei, Taiwan. He graduated from Chung-Cheng high School in 1994. He attended the National Sun Yat-Sen University from 1994-1998 and received a B.S. in Marine Environment and Engineering. He completed the Masters degree at the same university in 2000. He started his doctoral study at Civil, Architectural, and Environmental Engineering in the University of Texas at Austin in 2002.

Permanent address: 4600 Seton Center Parkway Apt. 702, Austin, TX, 78759

This dissertation was typed with MS Word by the author.